Fakultät für Physik und Astronomie
Ruprecht-Karls-Universität Heidelberg

Masterarbeit
im Studiengang Physik
vorgelegt von

Marcel Kern

aus Frankenthal (Pfalz)

2024

Verbesserte lokale Kontrolle von zweidimensionalen ultrakalten Atomwolken

Die Masterarbeit wurde von Marcel Kern
ausgeführt am
Kirchhoff-Institut für Physik in Heidelberg
unter der Betreuung von
Prof. Markus K. Oberthaler

Department of Physics and Astronomy
University of Heidelberg

Master Thesis
in Physics
submitted by

Marcel Kern

born in Frankenthal (Pfalz)

2024

Enhanced Local Control of Two-Dimensional Ultracold Atomic Clouds

This Master Thesis has been carried out by Marcel Kern
at the
Kirchhoff Institute for Physics in Heidelberg
under the supervision of
Prof. Markus K. Oberthaler

Verbesserte lokale Kontrolle von zweidimensionalen ultrakalten Atomwolken

In dieser Arbeit wird ein Aufbau mit einem Digital Micromirror Device (DMD) für verbesserte Kontrolle eines zweidimensionalen Bose-Einstein Kondensat Experiments geplant und ein entsprechender Testaufbau gebaut und charakterisiert. Der Aufbau ermöglicht nah-resonante, blau- oder rotverstimmte Potenziale auf die Atomebene zu projizieren und stellt damit weitere experimentelle Freiheitsgrade bereit. Ein lichtbasierter Feedback Algorithmus für den Testaufbau und ein dichtebasierter Algorithmus für das Hauptexperiment werden entwickelt und für verschiedenste Anwendungsfälle getestet, die auf verschiedenen Längenskalen anspruchsvoll sind. Auf Abruf, deterministische Vortexproduktion wird als neues, vielversprechendes Werkzeug für zukünftige Projekte erprobt. Erste experimentelle Ergebnisse von zwei unterschiedlichen Techniken werden für den aktuellen Aufbau mit nur einem DMD präsentiert.

Enhanced Local Control of Two-Dimensional Ultracold Atomic Clouds

In this thesis, a Digital Micromirror Device (DMD) setup for enhanced control of a two-dimensional Bose-Einstein condensate experiment is planned, and a corresponding test setup is built and characterized. The setup enables the projection of near-resonant, blue-, as well as red-detuned potentials onto the atomic cloud, providing more experimental degrees of freedom. A light-based feedback algorithm for the test setup, as well as a density-based algorithm for the main experiment, are developed and successfully tested for various patterns, which are all challenging on different length scales. On-demand, deterministic vortex production is explored as a new promising toolbox for upcoming projects. First experimental results based on two different techniques are presented using the current, single-DMD setup.

Contents

List of Figures

1 Introduction

In 1982, Feynman proposed analog quantum simulators (AQS) to efficiently simulate large quantum systems [21], which pose many important questions in modern physics. In AQS, the Hamiltonian of the simulated system is mapped onto the Hamiltonian of the simulator, which can be controlled to some extent. Thus, the simulator has to be tailored to a specific problem, such that the parameters of interest can be tuned. The simulator acts as a controllable "toy model" of the simulated system. An AQS can be noisy up to a certain threshold, while still allowing to study the property of interest and therefore, is already feasible today. A common platform for AQSs are ultracold atom experiments [3]. Here, a widely used type of simulator consists of ultracold atoms in optical lattices allowing the implementation of the Hubbard or transverse-field Ising Hamiltonian [4]. The atoms are trapped in the potential extremes and hence, form a discrete system. In contrast, a bulk atomic cloud can be used to simulate continuous quantum fields [54].

In continuous systems, the atomic density distribution and the interaction between particles are two key tuning knobs. One experimentally interesting bosonic species is ^{39}K because its two-particle interactions can be finely tuned using broad magnetic Feshbach resonances. Local density manipulations are achieved using a Digital micromirror device (DMD). By flipping individual mirrors in a micromirror array, arbitrary light potentials can be projected onto the atom cloud. Initially, spatial light modulators were used to create simple potentials like a box [23], while nowadays DMDs facilitate much more involved potentials [28]. Both finely tuned groundstates (for implementing effectively curved spacetime [54]) and far-from-equilibrium structured states (Vortex production [33] and supersolids [36]) can be prepared. However, the light potential shaped by a DMD is susceptible to various sources of noise, like interference effects, imperfections in the illumination and output optics, and finite resolution. All these issues affect the projected light field and limit the control provided by the DMD. The increasing complexity of the studied problems requires advances in the control of the atomic cloud and initial states.

One way to overcome these difficulties is a second DMD allowing for a more versatile optical power control spatially, as well as temporally. Spatially, an additional DMD can be used to decouple static and dynamical features e.g., by displaying a strong trapping potential on one and a sequence of precisely tuned, local manipulations on the other device. Additionally, the two light sources are not coherent with each other, which prevents interference effects between the two potentials and their wavelengths can be chosen freely. For example, a repulsive trapping potential and an attractive local manipulations can be applied, or two laser frequencies on the second DMD can drive two-photon Raman transitions. Temporally, the pulse time of a single-DMD setup is limited by the mirror refresh rate. By adding a second DMD, its laser light can be pulsed on and off, which can be done much faster.

Another way to improve the control of the light field in a single-DMD setup is the active correction of the light potentials. This active correction consists of a feedback algorithm that optimizes the DMD pattern based on the measured light signal or density distribution. With the algorithm, static imperfections from the illumination and output optics, as well as from the initial mirror configuration, and the Gaussian shape of the illumination beam are corrected. In this way, the full potential of the DMD is exploited.

This thesis aims to enhance the control of the condensate in the BECK experiment, a two-dimensional Bose-Einstein condensate of ^{39}K, by implementing both approaches. First, the theoretical and experimental background is introduced in sec. 2. In sec. 3, a test setup for a second DMD is presented and the implementation into the main experiment is explained. Next, a light- and a density-based feedback algorithm are introduced in sec. 4. Both algorithms have been extensively tested and the results are discussed. With this enhanced control, a new toolbox namely on-demand, deterministic vortex creation is explored. In sec. 5, two different approaches are tested with the single-DMD setup. Here, the first experimental results are presented and limitations are discussed.

2 Theoretical and Experimental Background

In this section, the theoretical principles on which the content of this thesis is based are introduced. First, the basic properties of the atomic species are discussed that were used for the experiments in this work. The experiments are performed with a two-dimensional Bose-Einstein condensate. Characteristic variables for this state of matter are derived in the second part. In the next section, the interactions between the atoms in the condensate and light are discussed including several techniques to manipulate ultracold atomic clouds. Finally, the specific experimental setup is described in more detail.

2.1 Properties of Potassium

For the experiments, the alkali-metal potassium with the chemical symbol "K" and atomic number $Z = 19$ is used. It has three isotopes: The unstable, fermionic ^{40}K, as well as the stable, bosonic ^{39}K and ^{41}K [49]. For the creation of a Bose-Einstein condensate, the most abundant bosonic isotope ^{39}K was chosen. Its ground state configuration is $^2\mathrm{S}_{1/2}$, while the first excited state is divided into the $^2\mathrm{P}_{1/2}$ and $^2\mathrm{P}_{3/2}$ state due to the electron spin-orbit coupling. The level structure of ^{39}K, including the hyperfine splitting, is shown in fig. 2.1. Typical for alkali metals are the two, strong spectral lines called the D-line doublet, which are the transitions from the ground state into the first exited states. The $^2\mathrm{S}_{1/2} \rightarrow {}^2\mathrm{P}_{1/2}$ transition corresponds to the D1 line and the $^2\mathrm{S}_{1/2} \rightarrow {}^2\mathrm{P}_{3/2}$ to the D2 line. The most relevant properties of the D-line doublet are presented in tab. 2.1.

Another important property of potassium is its Feshbach resonances [20, 9]. In a general scattering event as depicted in fig. 2.2a, two neutral particles enter the scattering state described by the interatomic potential via the energetically open reaction channel. The potential consists of the attractive Van-der-Waals, as well as the repulsive inter-nuclear interactions. On the other hand, a molecular bound state is forbidden by momentum conservation and, accordingly, the reaction channel is closed. However, when the bound state is energetically close to the scattering state, the particles can temporarily form a molecule. This phenomenon is called a Feshbach resonance. In the ultracold limit, s-wave scattering is dominant, which is described by a single parameter a_s. Accordingly, the so-called scattering length a_s changes depending on the mixing strength of the two reaction channels. Since the magnetic moments of the two channels differ, the energy difference between the two states can be controlled by an external magnetic field. According to [40],

λ_{D_2,D_1} (nm)	$\Delta'_{FS}/2\pi$ (GHz)	$\Delta'_{HFS}/2\pi$ (MHz)	$\Gamma/2\pi$ (MHz)
766.7, 769.9	1500	34	6.2

Table 2.1: Properties of the D-line doublet of ^{39}K with transition wavelength λ_{D1} and λ_{D2}, excited-state fine structure splitting Δ'_{FS}, excited-state hyperfine splitting Δ'_{HFS}, and natural linewidth Γ. Values taken from [25].

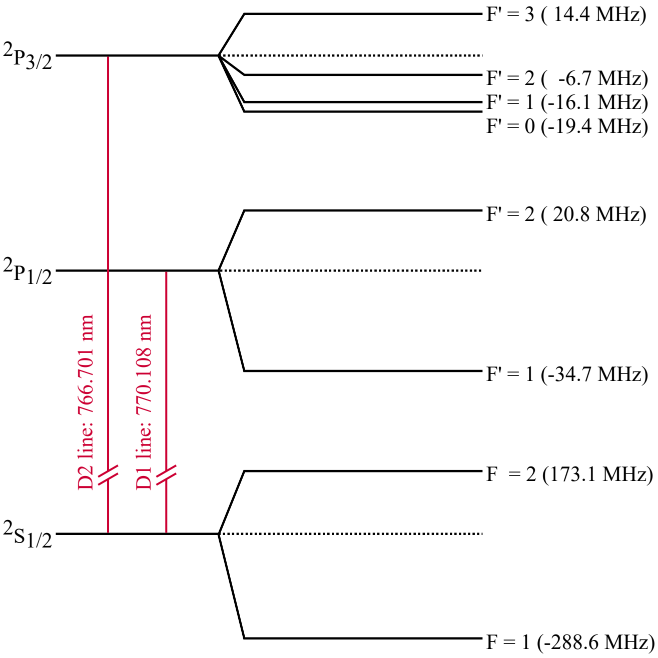

Figure 2.1: Level scheme of ^{39}K. The transitions from the ground state ^{2}S$_{1/2}$ to the excited states ^{2}P$_{1/2}$ and ^{2}P$_{3/2}$ are called the D line doublet. Image adapted from [53].

this changes the scattering length according to

$$a_s = a_{bg}\left(1 - \frac{\Delta}{B - B_0}\right). \tag{2.1}$$

Here, a_{bg} is the background scattering length, B_0 is the magnetic field strength of a resonance and Δ is the width of the corresponding resonance. The Feshbach resonances of ^{39}K in the $|F, m_f\rangle = |1, -1\rangle$ state at low magnetic field are illustrated in fig. 2.2b. While the particles repel each other at $a_s > 0$, they are attracted to each other for $a_s < 0$. At $a_s = 0$, the particles do not interact with each other. At zero magnetic field, the scattering length is $a_{bg} = -29.3(30)\,a_0$ [19]. However, only positive scattering length allow condensation. Therefore, the Feshbach resonance at $B_0 = 561.14(200)$ G [19] is used in the following to realize a Bose-Einstein condensate.

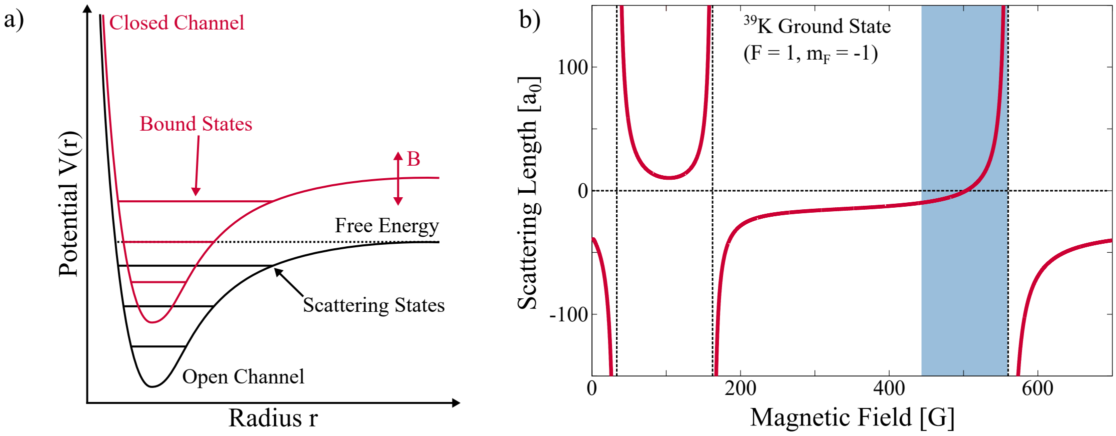

Figure 2.2: (a) Two-channel model for a Feshbach resonance. Two neutral particles that enter the energetically allowed open channel (black) form an unbound state. The entrance channel also couples to a molecular-bound state by the energetically forbidden closed channel (red). The coupling strength is controlled by an external magnetic field B. By temporarily forming a bound state, the prolonged interaction changes the s-wave scattering length a_s. (b) The Feshbach resonances of ^{39}K in the $|F, m_f\rangle = |1, -1\rangle$ state at low magnetic field. The resonance marked in blue is used in the experiment. Image adapted from [53].

2.2 Bose-Einstein Condensates

A Bose-Einstein condensate (BEC) is an ensemble of N bosons, which predominantly occupy the macroscopic ground state of the system. The condensate wave function can be described as a product of the N identical single-particle ground-state wave functions. This state was theoretically predicted by Albert Einstein in 1925 [17] by extending Satyendra Bose's work on quantum statistics [7]. The first atomic BECs were created in 1995 by Eric Cornell and Carl Wieman using ^{87}Rb [1], as well as Wolfgang Ketterle using ^{23}Na [12]. This section is based on a lecture by Georgy Shlyapnikov held in 2021 at the University of Amsterdam. The condensate forms a macroscopic quantum object, which is coherent and possesses superfluid properties. Its wave function can be decomposed into a condensate part $\Psi_0(\vec{r}, t)$ and a non-condensed part $\Psi'(\vec{r}, t)$. Thus, it can be represented as the sum of both parts:

$$\Psi(\vec{r}, t) = \Psi_0(\vec{r}, t) + \Psi'(\vec{r}, t) \tag{2.2}$$

2.2.1 Gross-Pitaevskii Equation

For a BEC in the weakly interacting regime satisfying $n|a_s|^3 \ll 1$ with condensate density n, the non-condensed part $\Psi'(\vec{r}, t)$ can be omitted. Then, the time-dependent Gross-Pitaevskii equation (GPE) governs the temporal evolution of the condensate. It was obtained by Eugen Gross [26] and Lev Pitaevskii [42] in 1961 and has the following form:

$$i\hbar\frac{\partial\Psi_0(\vec{r},t)}{\partial t} = \left[-\frac{\hbar}{2m}\nabla^2 + V(\vec{r},t) + gn\right]\Psi_0(\vec{r},t). \tag{2.3}$$

Here, $\hbar$ denotes the reduced Planck's constant, m is the particle mass, $V(\vec{r},t)$ is the external potential, $g = \frac{4\pi\hbar^2}{m}a_s$ is the interaction strength parameter of the system, and $n = |\Psi_0(\vec{r},t)|^2$ is the condensate density. It has the form of the Schrödinger equation with an additional, non-linear interaction term. The stationary solution of eq. 2.3 has the form:

$$\Psi_0(\vec{r},t) = \psi_0(\vec{r})\exp\left(-\frac{i\mu t}{\hbar}\right) \tag{2.4}$$

with chemical potential μ. Substituting the wave function 2.4 into eq. 2.3 results in the time-independent GPE:

$$\mu\,\psi_0(\vec{r}) = \left[-\frac{\hbar}{2m}\nabla^2 + V(\vec{r}) + gn\right]\psi_0(\vec{r}). \tag{2.5}$$

For a uniform condensate ($V(\vec{r}) = 0$), the ground state solution is

$$\psi_0(r) = \sqrt{n} \tag{2.6}$$

and the chemical potential is given by

$$\mu = ng. \tag{2.7}$$

To introduce the characteristic length scale of a BEC, a potential $V(x)$ is considered that is infinite at $x \leq 0$. It represents an infinite wall at $x = 0$ such that the condensate exists only at $x > 0$. This is equivalent to the boundary conditions $\psi_0(0) = 0$ and $\psi(\infty) = \psi_0$, which results in the ground state solution

$$\psi_0(x) = \pm\sqrt{n}\,\tanh\left(\frac{x}{\xi}\right) \tag{2.8}$$

with the healing length

$$\xi = \frac{\hbar}{\sqrt{mng}}. \tag{2.9}$$

This characteristic length scale for a weakly interacting BEC describes the minimum distance from a local perturbation to acquire the asymptotic value ψ_0.

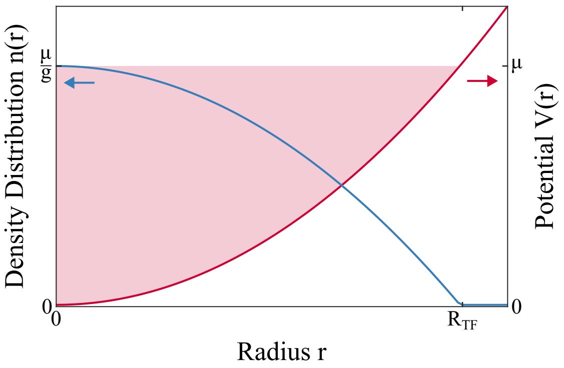

Figure 2.3: Thomas-Fermi profile (blue) in the corresponding harmonic trapping potential (red). The BEC (light red) fills up the potential according to its chemical potential μ. The size of the condensate is given by the Thomas-Fermi radius R_{TF}.

For a spherical harmonic potential

$$V(r) = \frac{m\omega^2 r^2}{2} \tag{2.10}$$

with particle mass m and angular frequency ω in a non-interacting BEC ($g = 0$), the ground state solution is the ground state wave function of a harmonic oscillator:

$$\psi_0(r) = \frac{\sqrt{n}}{\pi^{\frac{1}{4}} l_z^{\frac{1}{2}}} \exp\left(-\frac{r^2}{2l_z^2}\right) \tag{2.11}$$

with harmonic oscillator length

$$l_z = \sqrt{\frac{h}{m\omega_z}}. \tag{2.12}$$

2.2.2 Thomas-Fermi Approximation

In the Thomas-Fermi approximation, the condensate density and external potential are much larger than the kinetic energy and thus, it can be neglected in eq. 2.5. Now, the previously discussed harmonic potential in eq. 2.10 can be solved for $g > 0$. In this case, the condensate density is defined as

$$n = \frac{\mu - V(\vec{r}, t)}{g} \tag{2.13}$$

and the condensate wave function has the form

$$\psi_0(r) = \sqrt{\frac{\mu}{g}\left(1 - \frac{r^2}{R_{TF}^2}\right)}\, \theta(R_{TF} - r) \tag{2.14}$$

with the Thomas-Fermi radius

$$R_{TF} = \sqrt{\frac{2\mu}{m\omega_z^2}} \tag{2.15}$$

and the theta function $\theta(x)$, which is unity for positive arguments and zero otherwise. The Thomas-Fermi profile is illustrated in fig. 2.3. Accordingly, $\psi_0(r)$ is zero for any distance r from the origin larger than R_{TF}. In this approximation, the Thomas-Fermi radius corresponds to the radius of the BEC.

2.2.3 Two-Dimensional Bose-Einstein Condensate

By tightly confining the condensate in one direction, excitations are suppressed in this direction. Accordingly, the BEC behaves two-dimensionally since the dynamics are restricted to the remaining two dimensions. Analogous to [27], the wave function can be described by a product of a time-dependent 2D density profile $\Phi_0(x, y, t)$ and a time-independent 3D profile $\phi_0(x, y, z)$. The total wave function is given by $\Psi_0(\vec{r}, t) = \Phi_0(x, y, t)\phi_0(x, y, z)$ with $\int \mathrm{d}x\,\mathrm{d}y\,\mathrm{d}z|\phi_0(x, y, z)|^2 = 1$ and $\int \mathrm{d}x\,\mathrm{d}y|\Phi_0(x, y, t)|^2 = N$. Subsequently, the external potential is described by $V(\vec{r}, t) = V(x, y, t) + V_z(x, y, z)$. Inserting these expressions in eq. 2.3 results in

$$i\hbar\frac{\partial\Phi_0(x, y, t)}{\partial t} = \left[-\frac{\hbar}{2m}\nabla^2 + V_{2D}(x, y, t) + g_{2D}n_{2D}\right]\Phi_0(x, y, t), \tag{2.16}$$

where

$$V_{2D}(x, y, t) = V(x, y, t) + \int \mathrm{d}zV_z(x, y, z)|\phi_0(x, y, z)|^2, \tag{2.17}$$

$$g_{2D} = g\int \mathrm{d}z|\phi_0(x, y, z)|^4, \tag{2.18}$$

and $n_{2D} = |\Phi_0(x, y, t)|^2$. Furthermore, the chemical potential is replaced by

$$\mu_{2D} = \mu - \frac{\hbar}{2m}\int \mathrm{d}z\phi_0^*(x, y, z)\nabla^2\phi_0(x, y, z). \tag{2.19}$$

For the case of no external potential ($V(x, y, t) = 0$), the chemical potential is given by $\mu_{2D} = n_{2D}g_{2D}$.

The previously discussed harmonic potential (Eq. 2.10) as the time-independent, confining potential leads to the ground state wave function $\phi_0(z)$ described in

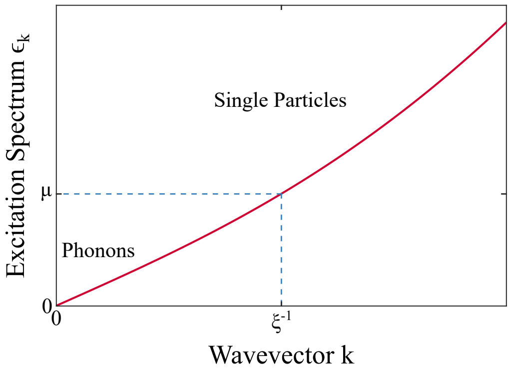

Figure 2.4: Bogoliubov dispersion relation of a uniform condensate. The blue lines mark the transition from a linear to a quadratic relation. At low energies, the excitations behave phonon-like, while they are particle-like for higher energies.

eq. 2.11. Inserting $\phi_0(z)$ in eq. 2.18 yields an interaction strength parameter of

$$g_{2D} = g\,\frac{1}{\pi l_z^2}\int \mathrm{d}z \exp\left(-\frac{2z^2}{l_z^2}\right) = \frac{1}{\sqrt{2\pi} l_z}\,g = \frac{\sqrt{8\pi}\hbar^2}{m}\frac{a_s}{l_z}, \tag{2.20}$$

which will be used throughout the thesis.

2.2.4 Bogoliubov Approximation

In the previous discussion, the non-condensed part $\Psi'(\vec{r},t)$ was omitted. In general, a fraction of particles is not in the groundstate wave function, leading to excitations like random fluctuations, sound, or topological defects like vortices and solitons. Therefore, $\Psi'(\vec{r},t)$ is now considered to first order. Inserting the full expression (Eq. 2.2) in eq. 2.3 yields

$$i\hbar\frac{\partial\Psi'(\vec{r},t)}{\partial t} = \left[-\frac{\hbar}{2m}\nabla^2 + V(\vec{r},t) + 2g\psi_0^2 - \mu\right]\Psi'(\vec{r},t) + g\psi_0^2\Psi'(\vec{r},t)^\dagger. \tag{2.21}$$

Applying Bogoliubov's approach [6] to $\Psi'(\vec{r},t)$ gives it the form

$$\Psi'(\vec{r},t) = \sum_\nu u_\nu(\vec{r})\exp\left(-i\epsilon_\nu t/\hbar\right) - v_\nu^*(\vec{r})\exp\left(i\epsilon_\nu t/\hbar\right), \tag{2.22}$$

where the excited quantum states are labeled by the index ν with eigenenergies $\pm\epsilon_\nu$ and eigenfunctions $u_\nu(\vec{r})$, as well as $v_\nu(\vec{r})$. Here, $u_\nu(\vec{r})$ corresponds to quasiparticles with energy ϵ_ν, while $v_\nu(\vec{r})$ represents anti-quasiparticles with energy $-\epsilon_\nu$. The eigenfunctions are normalized by $\int\left(u_\nu u_{\nu'}^* - v_\nu v_{\nu'}^*\right) = \delta_{\nu\nu'}$. Inserting the ansatz in eq. 2.21 results in the two Bogoliubov-de Gennes equations

$$\left[-\frac{\hbar^2}{2m}\nabla^2 + V(\vec{r},t) + 2g\psi_0^2 - \mu\right] u_\nu(\vec{r}) - g\psi_0^2 v_\nu(\vec{r}) = \epsilon_\nu u_\nu(\vec{r}) \tag{2.23}$$

$$\left[-\frac{\hbar^2}{2m}\nabla^2 + V(\vec{r},t) + 2g\psi_0^2 - \mu\right] v_\nu(\vec{r}) - g\psi_0^2 u_\nu(\vec{r}) = \epsilon_\nu v_\nu(\vec{r}) \tag{2.24}$$

for quasiparticles and anti-quasiparticles. For a uniform condensate ($V(\vec{r}) = 0$), the ground state solution and chemical potential are described by eq. 2.6 and 2.7, respectively. This simplifies eq. 2.23 and 2.24 to

$$\left[-\frac{\hbar^2}{2m}\nabla^2 + gn\right] u_\nu(\vec{r}) - gnv_\nu(\vec{r}) = \epsilon_\nu u_\nu(\vec{r}) \tag{2.25}$$

$$\left[-\frac{\hbar^2}{2m}\nabla^2 + gn\right] v_\nu(\vec{r}) - gnu_\nu(\vec{r}) = \epsilon_\nu v_\nu(\vec{r}). \tag{2.26}$$

With the ansatz $u_\nu(\vec{r}) = u_k \exp\left(i\vec{k}\vec{r}\right)$ and $v_\nu(\vec{r}) = v_k \exp\left(i\vec{k}\vec{r}\right)$, where $\vec{k}$ is the excitation wavevector, the Bogoliubov dispersion relation

$$\epsilon_k = \sqrt{\frac{\hbar^2|\vec{k}|^2}{2m}\left(\frac{\hbar^2|\vec{k}|^2}{2m} + 2ng\right)} \tag{2.27}$$

is obtained. The ansatz also yields negative energies $-\epsilon_k$. However, they should be omitted due to the resulting negative norm $(u_\nu u_{\nu'}^* - v_\nu v_{\nu'}^*)$. For $k \ll \xi^{-1}$ equal to $\epsilon_k \ll \mu$, the excitations are phonons or sound waves, and the dispersion relation with a linear dispersion relation

$$\epsilon_k = \hbar c_s k \tag{2.28}$$

with the speed of sound

$$c_s = \sqrt{\frac{ng}{m}}. \tag{2.29}$$

For $k \gg \xi^{-1}$ analogue to $\epsilon_k \gg \mu$, the excitations behave like particles with a quadratic dispersion relation

$$\epsilon_k = \frac{\hbar^2|\vec{k}|^2}{2m} + ng. \tag{2.30}$$

2.2.5 Quantized Vortices

A vortex is a macroscopically excited state in a BEC with a non-zero orbital angular momentum. As a topological feature of a superfluid, it is an important indicator of the dynamics of quantum fluids. Vortices have been first experimentally created and observed by Eric Cornell and Carl Wieman [39], Jean Dalibard [37], and Wolfgang Ketterle [41]. There are several techniques to create vortices in a condensate, from which two are later discussed in more detail.

Since a condensate with vortices represents a hydrodynamic-like system, the Mandelung equations [38] are used to describe the system. This formulation expresses the Schrödinger equation in terms of hydrodynamical variables. Analogue to [27], the wave function is used in the polar form

$$\Psi(\vec{r},t) = \sqrt{n(\vec{r},t)}\exp\left(i\theta(\vec{r},t)\right) \tag{2.31}$$

with condensate density $n(\vec{r},t)$ and phase $\theta(\vec{r},t) = \arg\Psi(\vec{r},t)$. To describe the probability flux in the system, eq. 2.31 is inserted into the definition of the probability current

$$\begin{aligned}\vec{j}(\vec{r},t) &= \frac{\hbar}{2mi}\left[\Psi^*(\vec{r},t)\nabla\Psi(\vec{r},t) - \Psi(\vec{r},t)\nabla\Psi^*(\vec{r},t)\right] && (2.32)\\ &= \frac{\hbar}{m}n(\vec{r},t)\nabla\theta(\vec{r},t). && (2.33)\end{aligned}$$

The form of the probability current is equal to that of hydrodynamics and electromagnetism and consists of a product of density and velocity. Consequently, the velocity is given by

$$\vec{v}(\vec{r},t) = \frac{\vec{j}(\vec{r},t)}{n(\vec{r},t)} = \frac{\hbar}{m}\nabla\theta(\vec{r},t). \tag{2.34}$$

Subsequently, the superfluid flows along the gradient of the phase. Moreover, the vorticity $\omega \equiv \nabla \times \vec{v}(\vec{r},t)$ is zero, such that the flow of a superfluid is irrotational. This implies that a pole, called a vortex core, is needed to allow circulation. Additionally, the velocity is inversely proportional to the distance to the pole. The circulation around any closed line that does not enclose the vortex core is zero. On the other hand, the calculation of the circulation around any closed line containing the vortex core yields

$$\oint v_s\,\mathrm{d}l = \oint \frac{\hbar}{m}\nabla\theta(\vec{r},t)\,\mathrm{d}l = \frac{2\pi\hbar}{m}s. \tag{2.35}$$

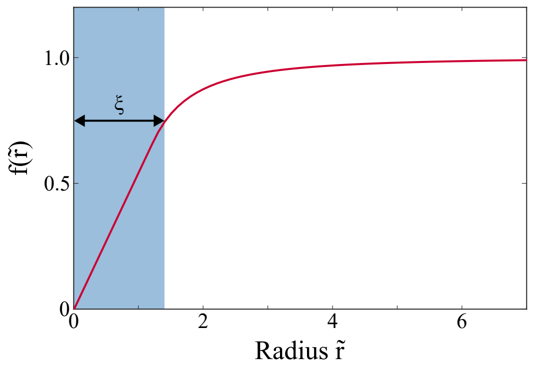

Figure 2.5: Numerical calculation of the radial wave function $f(\tilde{r})$ based on the stationary GPE for a vortex state with $|s| = 1$ (Eq. 2.38). The healing length ξ is marked in blue.

To have a single-valued wave function $\Psi(\vec{r}, t)$, s has to be an integer. Thus, the circulation of a superfluid is quantized in units of $\hbar/m$. Furthermore, the phase of the condensate has to change by multiples of 2π, when following the path of circulation. The so-called charge s of a vortex describes the number of 2π windings of the phase. It can be negative or positive, which corresponds to a clockwise or counter-clockwise circulation and refers to an antivortex or vortex, respectively. Vortices with opposite charges can combine, which annihilates the flow. As a vortex creates a pole in the wave function, the total charge number S of a condensate is a topological property and thus is conserved. Consequently, the vortex can only decay at the border of the condensate. The energy associated with a vortex is dominated by the kinetic energy $E_v \propto v_s^2 \propto s^2$. Thus, it is energetically favorable to have many singly-charged vortices instead of a single, higher-charged vortex, which accordingly decays into many singly-charged vortices.

In [42], the vortex state is described based on the GPE. By considering a single vortex with $|s| = 1$ in free space, the condensate wave function has the form

$$\psi(r) = \sqrt{n} f(r) \exp(i\theta) \,, \tag{2.36}$$

where $f(r)$ is a function that only depends on the distance $|r|$. Inserting eq. 2.36 into the stationary GPE (Eq. 2.5) yields

$$-\frac{\hbar^2}{2m}\left(\frac{\mathrm{d}^2}{\mathrm{d}r^2} + \frac{1}{r}\frac{\mathrm{d}}{\mathrm{d}r} - \frac{1}{r^2}\right) f + ng|f|^2 f - \mu f = 0. \tag{2.37}$$

Here, the Laplacian is used in polar coordinates. Inserting eq. 2.7 and introducing

$\tilde{r} = \frac{\sqrt{2}r}{\xi}$ with healing length ξ (Eq. 2.9), the expression simplifies to

$$\frac{\mathrm{d}^2 f}{\mathrm{d}\tilde{r}^2} + \frac{1}{\tilde{r}}\frac{\mathrm{d}f}{\mathrm{d}\tilde{r}} - \frac{f}{\tilde{r}^2} - f^3 + f = 0. \tag{2.38}$$

With this expression, $f(\tilde{r})$ can be calculated numerically and is illustrated in fig. 2.5. In the limits $\tilde{r} \to 0$ and $\tilde{r} \to \infty$, the function behaves according to

$$f(\tilde{r}) \propto \tilde{r}, \qquad \tilde{r} \to 0 \tag{2.39}$$

$$f(\tilde{r}) \propto \left(1 - \frac{1}{2\tilde{r}^2}\right), \qquad \tilde{r} \to \infty. \tag{2.40}$$

The vortex core radius is $r_c \sim \xi \sim \frac{1}{\sqrt{n a_s}}$ and recalling the condition for the weakly interacting regime $n|a_s|^3 \ll 1$, results in $r_c \ll n^{-1/3}$. So, the vortex state is a macroscopically excited BEC state with a core size in the order of the healing length.

2.3 Atom-Light Interactions

To trap neutral atoms and create a Bose-Einstein condensate, three different types of traps are frequently used: Radiation-pressure traps, magnetic traps, and optical dipole traps. Normally, a sequence of the different traps is utilized in experiments to cool down the atoms. While the optical dipole trap achieves the lowest trap depth of those three techniques, it keeps the optical excitation extremely low. This enables experiments in the order of many seconds. Therefore, the final trap geometry is usually realized by using the optical dipole force. It is not only used for cooling and trapping but also to manipulate the trapped atom cloud. Due to this versatility, the effect of optical dipole traps on atoms is discussed in more detail, followed by two techniques to manipulate the atomic cloud.

2.3.1 Conservative Optical Dipole Potentials

The following introduction to atom trapping in optical dipole potentials is based on [25]. All considerations are made under the assumption of far-detuned light to avoid Rayleigh scattering processes as it simplifies the calculations. In the presence of an external electric field, the energy levels of an atom or molecule split and shift. The so-called Stark effect is the electric field analog of the Zeeman effect caused by magnetic fields. More precisely, the Alternating Current (AC) Stark effect applies to optical dipole traps, since the electric fields of lasers vary in time. Atoms and molecules can be described as an ensemble of point charges and thus, are approximated as a dipole.

In a two-level atom, the interaction Hamiltonian is given by

$$\hat{H}^{(1)} = -\hat{\mu}\vec{E} \tag{2.41}$$

with the electric dipole operator $\hat{\mu} = -e\vec{r}$ and the electric field $\vec{E}$. For detunings Δ much larger than the Rabi frequency Ω, the radiative coupling is introduced to the Hamiltonian as a small perturbation

$$\hat{H} = \hat{H}^{(0)} + \hat{H}^{(1)}. \tag{2.42}$$

Here, $\hat{H}^{(0)}$ is the Hamiltonian of the unperturbed system with the eigenstates $|\psi_j\rangle$ and the known energy levels $E_j^{(0)} = \langle\psi_j|\,\hat{H}^{(0)}\,|\psi_j\rangle$. When considering the perturbation up to the second order, the energy levels are given by

$$E_j = E_j^{(0)} + \langle\psi_j|\,\hat{H}^{(1)}\,|\psi_j\rangle + \sum_{k\neq j} \frac{\langle\psi_k|\,\hat{H}^{(1)}\,|\psi_j\rangle\,\langle\psi_j|\,\hat{H}^{(1)}\,|\psi_k\rangle}{E_j^{(0)} - E_k^{(0)}}. \tag{2.43}$$

Due to the properties of the dipole operator $\hat{\mu}$, the first-order term is zero. Accordingly, the energy shift of the j-th state is

$$\Delta E_j = \sum_{k\neq j} \frac{|\langle\psi_k|\,\hat{H}^{(1)}\,|\psi_j\rangle|^2}{E_j^{(0)} - E_k^{(0)}} = \sum_{k\neq j} \frac{|\langle\psi_k|\,\hat{\mu}\,|\psi_j\rangle|^2}{E_j^{(0)} - E_k^{(0)}}|\vec{E}|^2. \tag{2.44}$$

The atom has zero internal energy in the ground state, while the field energy is $n\hbar\omega$ depending on the number of photons n. In total, this state has an energy of $E_j^{(0)} = n\hbar\omega$. In the excited state, the atom has an energy of $\hbar\omega_0$, while the field energy is reduced to $(n-1)\hbar\omega$. This amounts to a total energy of $E_k^{(0)} = \hbar\omega_0 + (n-1)\hbar\omega = -\hbar\Delta + n\hbar\omega$. Consequently, $E_j^{(0)} - E_k^{(0)} = \hbar\Delta$ in eq. 2.44. Furthermore, the electric field can be described by the intensity using the relation

$$I = 2\epsilon_0 c_0 |\vec{E}|^2 \tag{2.45}$$

with the vacuum permittivity ϵ_0 and the speed of light c_0. Fermi's golden rule for the energy level transition between two discrete states yields

$$\Gamma_{j\to k} = \frac{\omega_0^3}{3\pi\epsilon_0\hbar c_0^3}|\langle\psi_k|\,\hat{\mu}\,|\psi_j\rangle|^2. \tag{2.46}$$

This spontaneous decay rate of the excited state is analogous to the natural linewidth of the transition. Inserting eq. 2.45 and 2.46 into eq. 2.44 results in

$$\Delta E_j = \frac{3\pi c_0^2}{2\omega_0^3}\frac{\Gamma}{\Delta} I. \tag{2.47}$$

For red-detuned light ($\Delta < 0$), the ground state energy E_j is shifted down by ΔE_j, while the excited state E_k is shifted up by $\Delta E_k = -\Delta E_j$[1]. In contrast, blue-detuned light ($\Delta > 0$) shifts the ground state energy up by ΔE_j and the excited state down by $\Delta E_k = -\Delta E_j$. For dipole trapping usually low saturation is used, which implies that the atoms reside most of the time in the ground state. Consequently, red-detuned light attracts the atoms, while blue-detuned light repels them.

In a multi-level atom, the dipole matrix elements depend on the specific transition. According to the Wigner-Eckart theorem [16, 55], the dipole operator elements μ_{jk} can be expressed as the product of a reduced matrix element $\|\mu\|$ that is independent of the quantum numbers and a Clebsch-Gordan coefficient c_{jk}. In this way, the energy shift of a ground state $|\psi_j\rangle$ with several excited states $|\psi_k\rangle$ is described by

$$\Delta E_j = V_{dip} = \frac{3\pi c_0^2}{2\omega_0^3}\frac{\Gamma}{\Delta} I \cdot \sum_k \frac{c_{jk}^2}{\Delta_{jk}}. \tag{2.48}$$

Here, the detunings Δ_{jk} and the line strengths c_{jk} of all coupled excited states are considered. The energy shift ΔE_j can be interpreted as a ground-state dipole potential V_{dip}.

For alkali atoms and $\Delta \gg \Delta'_{HFS}$, eq. 2.48 yields

$$V_{dip,F}(\vec{r}) = \frac{\pi c^2 \Gamma}{2\omega_0^3} \left(\frac{2 + \mathcal{P}\cdot g_F \cdot m_F}{\Delta_{2,F}} + \frac{1 - \mathcal{P}\cdot g_F \cdot m_F}{\Delta_{1,F}}\right) I(\vec{r}) \tag{2.49}$$

with polarization $\mathcal{P}$, Landé factor g_F and magnetic quantum number m_F. Circular polarized $\sigma^{\pm}$ light imply $\mathcal{P} = \pm 1$, while linear polarization give $\mathcal{P} = 0$. In the latter case, the expression simplifies further to

$$V_{dip,F}(\vec{r}) = \frac{\pi c^2 \Gamma}{2\omega_0^3} \left(\frac{2}{\Delta_{2,F}} + \frac{1}{\Delta_{1,F}}\right) I(\vec{r}). \tag{2.50}$$

The dipole potential $V_{dip,F}$ is connected to the scattering rate Γ_{sc} by

$$\hbar\Gamma_{sc} = \frac{\Gamma}{\Delta} V_{dip} \tag{2.51}$$

---

[1] Here, $E_k^{(0)} - E_j^{(0)} = -\hbar\Delta$.

Figure 2.6: Azimuthally varying phase pattern to imprint a vortex with integer angular momentum s. The angular momentum s depends on the discontinuity equals $2\pi s$. The color map represents the phase gradient.

and directly provides an expression for the scattering rate based on eq. 2.50:

$$\Gamma_{sc,F}(\vec{r}) = \frac{\pi c^2 \Gamma^2}{2\hbar\omega_0^3} \left(\frac{2}{\Delta_{2,F}^2} + \frac{1}{\Delta_{1,F}^2}\right) I(\vec{r}) \tag{2.52}$$

Equations 2.50 and 2.52 can be used to estimate the trap depth and optical excitation for an atomic cloud consisting of alkali atoms.

2.3.2 Phase Imprinting

The phase imprinting method was introduced first in a numerical study by Wolfgang Ertmer [15] in 1999 and was then experimentally demonstrated by William Phillips [14]. The method modifies the phase distribution of a BEC by exposing it to a far-off-resonant laser pulse with intensity $I(x,y)$. Thereby, the atoms experience a conservative Stark-shift potential $V_{dip}(x,y)$ that was introduced in the previous section. Consequently, they acquire a phase of

$$\phi(x,y) = \frac{V_{dip}(x,y)t_L}{\hbar}, \tag{2.53}$$

where t_L is the laser pulse duration. For short laser pulse durations t_L in the order of microseconds (Raman-Nath regime [11]) and $V_{dip}(x,y)$ much larger than the other energy scales, all other terms in eq. 2.5 can be neglected. Then, the dynamical effect of $V_{dip}(x,y)$ corresponds to a phase imprint, which modifies the initial wave function according to

$$\psi \rightarrow \psi \exp[-i\phi(x,y)]. \tag{2.54}$$

If the potential $V_{dip}(x,y)$ consists of an azimuthally varying phase pattern as de-

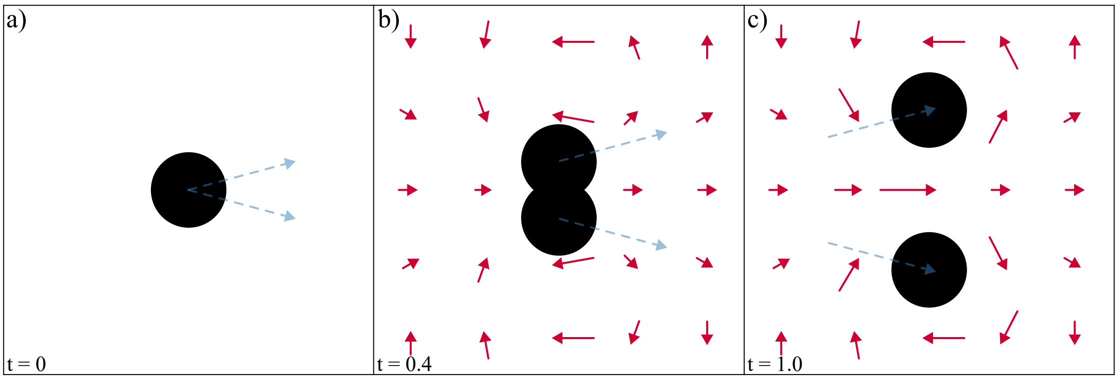

Figure 2.7: Chopsticks sequence at different times t/t_s with the total sweep time t_s. (a) Initial position (x_i, y_i) of the collocated chopstick beams. The local fluid flows (red arrows) are negligible. From this position, the chopsticks start to move apart (blue arrows) with sweep velocity (v_x, v_y). (b) Position of the chopsticks at $t = 0.4$. The beams act as obstacles that push atoms out of their way. These atoms flow around the beams and fill the vacant space behind them. (c) Final positions of the chopsticks. The flow velocity around the beams corresponds to a phase winding of 2π, which forms two, counter-rotating vortices pinned to the laser beams. Based on numerical simulations from [45].

picted in fig. 2.6, a vortex with integer angular momentum s can be generated. The phase difference at the discontinuity has to be equal to $2\pi s$. This produces one vortex in the middle of the condensate and changes the condensate's total angular momentum by s.

2.3.3 Chopsticks Method

The chopstick method was experimentally demonstrated by Brian Anderson [45] in 2016 with a numeric companion paper [24]. The sequence, depicted in fig. 2.7, starts with two collocated, blue-detuned laser beams, the so-called chopsticks, that pierce the BEC. The beams are moved together in one direction, while also moving apart. When the distance between the beams is in the same order as their diameter, the beams come to a rest and fade out. However, the distance and angle between the beams are not critical parameters. The beams act as obstacles that push atoms out of their way as they move through the condensate. These atoms then flow around the beams and fill the vacant space behind them. The flow velocity around the beams has to be high enough to correspond to a phase winding of 2π. Then, two, counter-rotating vortices form, whereby their vortex cores are pinned to the laser beams. By ramping the chopstick's intensity down, the vortices are released. The total angular momentum of the condensate is conserved as the charges have opposite signs. By driving one of the chopsticks out of the condensate, non-neutral charge configurations can be generated. Furthermore, multiple vortices can be deposited on a single chopstick by overlapping it with another chopstick that is then ramped down. The charge of the vortices stored on the so-called repository beam adds up. Note that only a certain number of vortices can be stored on such a beam before they start to leak out, which depends on the beam size. Here, the beam width should be larger than the number of vortices times the healing length.

The potential of the chopsticks is described by

$$V_{dip}(x,y,t) = V_0 \sum_{j=1}^{2} \exp(-\frac{2}{\sigma_c^2}[(x,y)-(x_i,y_i)_j-(v_x,v_y)_j t]^2) \tag{2.55}$$

with the maximum repulsive potential energy of each beam $V_0 = 0.8\mu_{2D}$, the $1/e^2$ radius of the chopsticks σ_c, the initial position (x_i, y_i) and sweep velocity (v_x, v_y) of beam j. For a successful vortex generation, the beam radius σ_c and the sweep velocity $|\vec{v}_s|$ have to be matched in accordance to fig. 1 in [24]. For too-small velocities, no vortices are created, while for too-high velocities, the vortices are lost from their beams and remain behind. For condensates in a harmonic trap, chopsticks with $\sigma_c < 3.4\,\mu\text{m}$ [2] do not support trapping due to vortex precession induced by the trap geometry [13].

2.4 BECK Experiment

The following work has been conducted at the Bose-Einstein Condensate ^{39}K (BECK) experiment. In this section, the experimental setup is described. A more detailed description of the whole setup, as well as the condensate preparation sequence, can be found in [30, 53].

Figure 2.8 illustrates the vacuum system of the experiment illustrating the path of the atoms. To prepare the condensate, an oven provides thermal potassium atoms that are trapped and pre-cooled in a two-dimensional magneto-optical trap (MOT). Here, the atoms are only confined in two dimensions, forming a cigar-like shape. A push beam transfers the atom cloud through a differential pumping stage into the science chamber loading a three-dimensional MOT. The science chamber is a glass cell providing high optical access and allows a proximate placement of magnetic coils. Next, the gray molasses cooling scheme is applied to reach sub-Doppler temperatures. To obtain only atoms in the low-field seeking $|F, m_f\rangle = |1, -1\rangle$ state, the atoms are transferred into a magnetic trap. ^{39}K has a negative background

---

[2] Corresponding to $b_w = \sqrt{2\ln(2)} \cdot \sigma_c < 4\,\mu\text{m}$

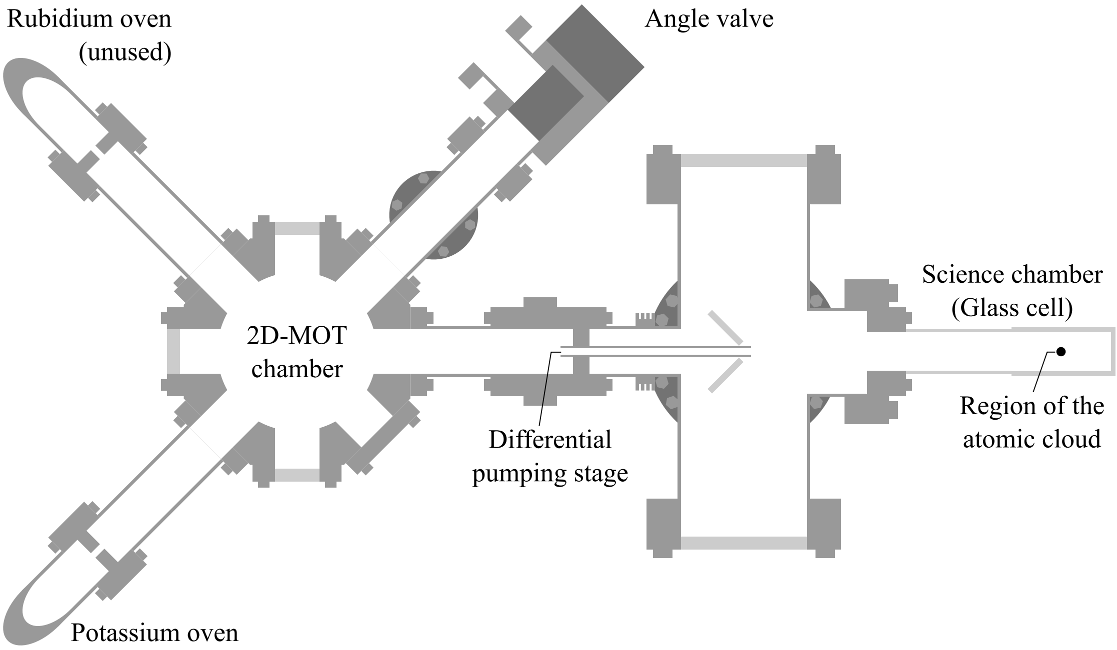

Figure 2.8: Top view of the vacuum system. The potassium oven provides a thin background gas in the 2D-MOT chamber with a pressure of 10^{-7} mbar. The atoms are transferred through a differential pumping stage into the science chamber with an ultra-high vacuum below 10^{-11} mbar. Here, the experiments are performed. Image adapted from [30].

scattering length of $a_{bg} = -29.3(3)\,a_0$ [19] at zero magnetic field, making condensation impossible. However, the $|F, m_f\rangle = |1, -1\rangle$ state has a Feshbach resonamce at 561.14(2) G [19], which allows to set a positive scattering length. The atoms are loaded into an attractive optical dipole trap. By evaporative cooling, the atoms condense and are then transferred into the final trap geometry. For the vertical confinement, a pancake trap with a trapping frequency of $\omega_z = 1.5\,\text{kHz}$ provides a time-independent, spherical harmonic potential. Accordingly, the condensate sits between two repulsive sheets of light that are separated by 5 µm. The horizontal confinement is configurable due to a DMD. This device modulates a laser beam and can create any desired dipole potential. In the following, the DMD is explained in more detail as the emphasis of this work is to enhance the control of the horizontal confining potential. Due to the highly anisotropic trapping geometry, most excitations occur in the horizontal direction, which limits the dynamics in the condensate to two dimensions.

The experiment prepares a two-dimensional potassium condensate that can be manipulated by an arbitrarily shaped optical dipole potential, as well as an external magnetic field. Following eq. 2.3, the arbitrary dipole potential allows to control $V(x, y, t)$ and subsequently, the condensate density n_{2D}. By using the broad Feshbach resonance of ^{39}K at 561.14(2) G [19], the interaction strength parameter g can be tuned via the magnetic field. For $g < 0$ the system is attractive, while it is repulsive for $g > 0$. An ideal, non-interacting system can be achieved at $g = 0$.

3 Digital Micromirror Device Setup

This section describes the second DMD setup in more detail. Since the components are very similar to the existing setup, which is described in [47], this section focuses on the differences, as well as the added complexity of simultaneously employing two DMD setups in the experiment. First, the laser and illumination setup are described. Next, the DMD itself is discussed in more detail. Special emphasis is laid on the new controller board mount that also acts as a passive heat sink. Then, the output optics are described, followed by the analysis of interference effects observed during testing. Finally, the planned implementation in the main experiment is presented. All optical components used in the DMD setup are listed in appendix A.

3.1 Laser Setup

The second DMD is planned to operate with near-resonant light close to the D2-line of $\lambda = 767\,\mathrm{nm}$. Due to its large tuning range from 700 nm to 1030 nm, a *Coherent MBR-110* Ti:Sapphire (Ti:Sa) laser will be used. For a first test setup that operates independently from the main experiment, a blue-detuned wavelength of 760 nm is used. The cavity mirrors that are currently employed are suitable for wavelengths between 750 nm to 870 nm [10], which means the setup can be switched to red-detuned operation, without any modifications. To pump the Ti:Sa laser, the *Coherent Verdi V-10* laser operates at 27 A, which corresponds to approx. 7 W. Consequently, the power of the Ti:Sa laser amounts to 500 mW. Figure 3.1a shows that the laser has to operate for at least three hours to maintain a stable, linear polarization.

In fig. 3.2a, the beam path from the Ti:Sa laser into the fiber is illustrated. First, the laser beam passes through a half-wave plate and a polarizing beamsplitter (PBS) allowing for power control. To avoid clipping in the acousto-optic modulator (AOM), a Galilean telescope reduces the beam diameter by a factor of 1.5. Although the *Crystal Technology AOMO 3110-120* AOM is only rated for wavelength from 442 nm to 633 nm, up to 60 % of the light is diffracted into the first order. In fig. 3.1c, the diffracted power depending on the voltage-controlled oscillator (VCO) level is displayed. The voltage range between 400 mV to 700 mV is used for active power stabilization. The light is then coupled into a polarization-maintaining, single-mode fiber with a coupling efficiency of 50 %.

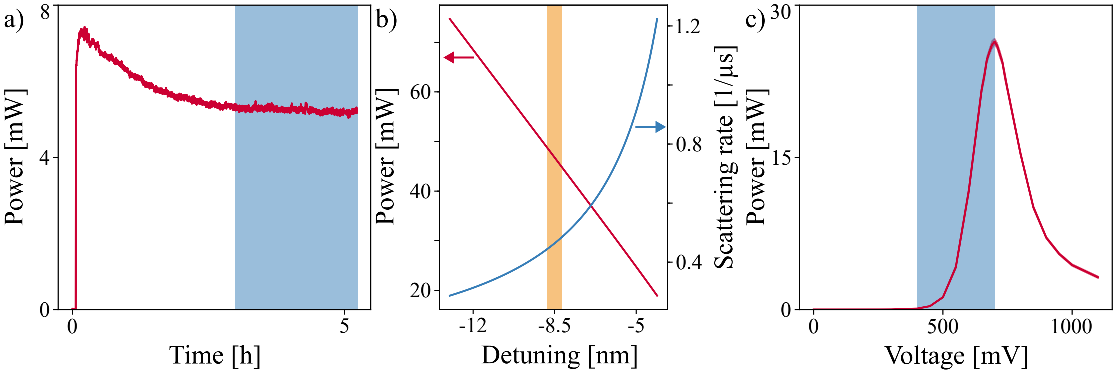

Figure 3.1: (a) Power fluctuations caused by polarization fluctuations after powering on the Ti:Sa laser. The laser operates stable after 3 h (blue). (b) The required power and corresponding scattering rate for different detunings to project a potential of 100 kHz onto the atom cloud. The orange marked detuning corresponds to the used wavelength of 760 nm. (c) Laser power depending on the VCO level of the AOM driver. The blue-marked voltage range is used for power stabilization. The laser power in (a) and (c) is measured after the fiber in fig. 3.2b.

The most intensity-demanding application to manipulate the condensate is a phase imprint (Sec. 2.3.2). To acquire a phase of 2π with a pulse duration of $t_L = 1\,\mu\mathrm{s}$, potentials up to 100 kHz have to be reached according to eq. 2.53. Since linear polarized light with $\Delta \gg \Delta'_{HFS} = 2\pi\cdot\ 34\,\mathrm{MHz}$ (Tab. 2.1) is used, all assumptions made in eq. 2.50 are met. Inserting a wavelength of $\lambda = 760\,\mathrm{nm}$, a center wavelength of the hyperfine split of $\omega_0 = 768.5\,\mathrm{nm}$ and a natural linewidth of $\Gamma = 2\pi\cdot\ 6\,\mathrm{MHz}$ (Tab. 2.1) yields a required intensity of $I(r) = 0.0015\,\mathrm{mW}\,\mu\mathrm{m}^{-2}$. To estimate the laser power, a Gaussian intensity distribution with $\frac{1}{e^2}$ beam radius of 70 µm at the atomic plane is assumed in accordance with [47]. For a typical condensate radius of 35 µm in the BECK experiment, a power of 50 mW is required to achieve the desired potential throughout the entire atomic cloud. For this intensity, eq. 2.52 yields an average scattering rate of $\Gamma_{sc,F} = 0.05\,\mu\mathrm{s}^{-1}$ for a condensate of 40 000 atoms and reaches a maximum of $0.14\,\mu\mathrm{s}^{-1}$. Consequently, scattering is unlikely for millisecond-long manipulations of the condensate. The required laser power and corresponding scattering rate for different detunings are depicted in fig. 3.1b.

The used Ti:Sa laser is sufficient to illuminate the DMD chip with the calculated optical power. For the test setup, the light is projected onto a camera, which only needs several microwatts of power. Thus, 400 mW of the power has to be transmitted through the PBS onto a beam dump, and only 100 mW are reflected to reach the fiber. Note that the polarization noise behaves anti-proportional to the reflected power. Observations show that this noise can be neglected if not

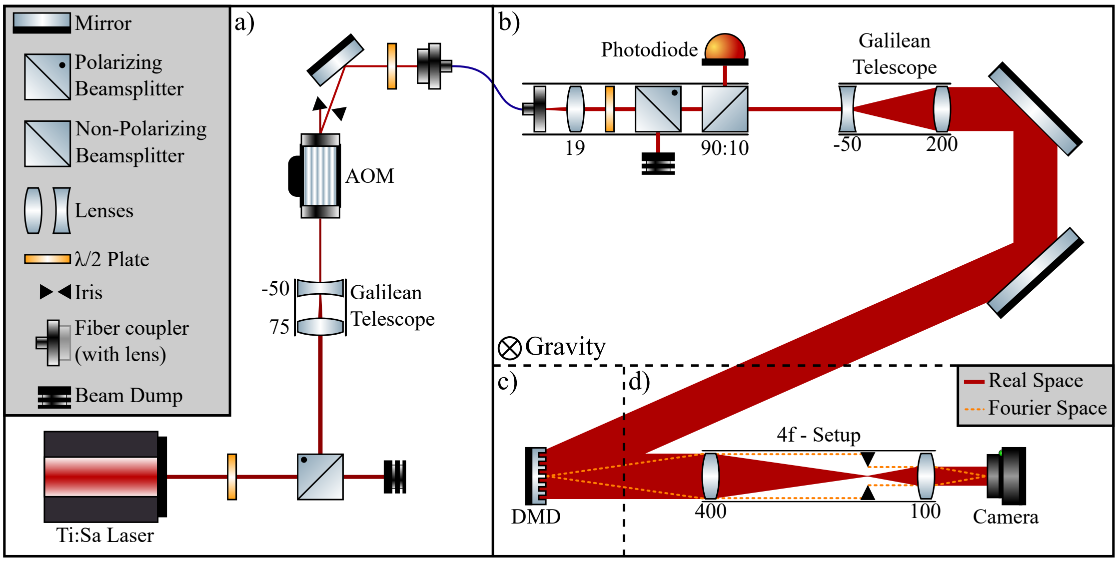

Figure 3.2: (a) Schematic of the laser setup and (b,c,d) test setup. The two setups are constructed on different optical tables and are connected via an optical fiber. The test setup is divided into (b) illumination optics, (c) DMD chip, and (d) output optics. Focal length of the lenses in millimeters.

more than 80 % of the power is transmitted to the beam dump. With the VCO level, the power can be further reduced before it is coupled into the fiber.

3.2 Illumination Optics

Now, the optical fiber with the laser light can be routed towards the DMD chip. In fig. 3.2b, the optical path is depicted. The beam has to be widened such that it illuminates the whole chip, which has a size of 19.4 mm × 12.1 mm. First, the beam is collimated with a lens to a diameter of approx. $d = 5\,\mathrm{mm}$. The focal length of the lens is determined by

$$f = \frac{d}{2 \cdot \mathrm{NA}}, \tag{3.1}$$

where the NA describes the numerical aperture of the fiber. With an NA of 0.12, the focal length of the lens amounts to approx. $f = 20.8\,\mathrm{mm}$. The ray model that uses the NA overestimates the beam size and accordingly, a slightly larger focal length is suggested by [48]. Then, a Galilean telescope with a magnification of 4 is used to widen the beam to a diameter of 20 mm. As the telescope is built with 1 inch optics, a collimator lens with a focal length of $f = 19\,\mathrm{mm}$ was used to avoid clipping. Before entering the telescope, the laser beam passes once more through a half-wave plate followed by a PBS to clean the polarization and

DLP9000X properties	
DMD array size	2560 px × 1600 px
Micromirror size	7.6 µm × 7.6 µm
Active region size	19.4 mm × 12.1 mm
Micromirror tilt angle	±12°
AR coating	400 nm to 700 nm
Micromirror reflectivity	88 %
Array diffraction efficiency	86 %
Array fill factor	92 %
Window transmission	95 %
DLP V4390 properties	
Onboard memory	16 GB (min. 50 000 1-bit frames)
Min. Dark Phase	90 µs (Standard) 77 µs (High Speed)
Max. temperature	80 °C

Table 3.1: Specifications of the *DLP9000X* chip and the *DLP V4390* controller board. Data taken from [31] and [52].

control the power. Afterward, a part of the signal is reflected onto a photodiode. For the main experiment, a beam sampler with a reflectance of 1 % is used and the photodiode is operated in the photoconductive mode to reduce the response time (Appendix C.1a). Due to the lower beam power in the test setup, a 90:10 beamsplitter reflects the majority of light onto the photodiode that is attached to a slower transimpedance amplifier (Appendix C.1b). In both cases, the output voltage is connected to a proportional–integral (PI) controller that stabilizes the power by modifying the VCO level of the AOM in the laser setup. Two 2 inch mirrors are used to guide the beam onto the DMD chip.

3.3 Digital Micromirror Device

A DMD is a spatial light modulator that modulates the amplitude and direction of incoming light. Depending on the application, the device can be either placed in the image or Fourier plane. In this setup, the DMD is used to manipulate the image plane (Fig. 3.2c). Analogous to [47], a *DLP9000X* chip with *ViALUX DLP V4390* controller board was chosen. The specifications are listed in tab. 3.1. Although the used wavelength is not within the AR coating specification, the device can be used up to a wavelength of $\lambda = 2500\,\mathrm{nm}$ with reduced efficiency [52].

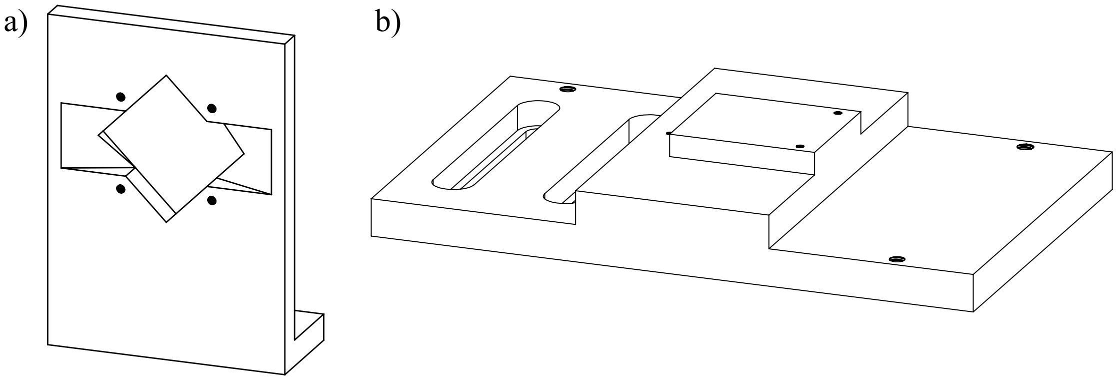

Figure 3.3: (a) Self-designed Mounting hardware for the DMD chip and (b) the controller board. Both are made from aluminum. Technical drawings with dimensions can be found in appendix B.4 and B.2.

3.3.1 DMD Chip and Controller Board Mount

The DMD chip has to be mounted with an angle of 45°, such that the reflected beams run parallel to the table surface regardless of the mirror state. The DMD mount design from [47] was adapted to a beam height of 12.5 cm. Figure 3.3a shows a sketch of the new DMD chip mount. In the new version, the material thickness was decreased and slopes on both sides of the chip were added. These slopes allow for steeper angles for the in- and outgoing light, which simplifies the alignment. The mount was made from aluminum and contains screw threads such that it can be mounted onto the *Newport 9081-M* 5-axis translation stage.

The *ViALUX DLP V4390* controller board houses two field-programmable gate arrays (FPGA). The applications (APPS) FPGA allows the user to communicate with the DMD chip via an application programming interface (API). It processes the image data that it receives over a USB interface and sends it to the digital down-converter (DDC) FPGA. The DDC-FPGA provides a high-speed data and control interface for the DMD chip and is also responsible for the mirror clocking pulses and timing information. The DDC-FPGA is cooled passively, while the APPS-FPGA comes with active cooling. Due to spatial constraints, the cooling fan of the stock design has a size of 20 mm × 20 mm and thus, has to run at 13 000 RPM to provide the required thermal resistance of $\mathrm{R}_{TH} = 3.07\,\mathrm{K\,W^{-1}}$ [18]. As a consequence, the fan introduces vibrations on the DMD chip, which can heat the atoms in the trapping potential projected by the DMD. To avoid the vibrations, a new controller board mount that acts as a passive heat sink was designed to replace the active cooling solution.

To ensure that the APPS-FPGA operates within its temperature limit, the needed power dissipation performance of the heat sink is calculated. The following calculations are adopted from [46]. Starting with the thermal resistance given by

$$R_{TH} = \frac{T_{MAX} - T_A}{TDP} \tag{3.2}$$

$$= \frac{R_\lambda}{d}, \tag{3.3}$$

where T_{MAX} is the maximum operating temperature of the given device, T_A is the ambient temperature and TDP is the thermal design power of the device. R_λ is the specific thermal resistance and d is the material thickness. Typically, the ambient temperature ranges from 35 °C to 45 °C with external airflow and from 50 °C to 60 °C, if the component is enclosed. The TDP of the APPS-FPGA is not known, but with $T_{MAX} = 80\,°\mathrm{C}$, $T_A = 35\,°\mathrm{C}$ and $R_{TH} = 3.07\,\mathrm{K\,W^{-1}}$, it is approx. 15 W according to eq. 3.2. With this TDP and $T_A = 60\,°\mathrm{C}$, the new heat sink needs a thermal resistance of $R_{TH} = 1.3\,\mathrm{K\,W^{-1}}$. For aluminium, the specific thermal resistance is $R_\lambda = 4.25 \times 10^{-3}\,\mathrm{W\,m^{-1}\,K^{-1}}$ [43]. Following eq. 3.3, the material thickness has to be larger than $d = 4\,\mathrm{mm}$. The designed heat sink has a thickness of $d = 25\,\mathrm{mm}$, such that the thermal resistance is $R_{TH} = 0.17\,\mathrm{K\,W^{-1}}$.

Next, the thermal budget is estimated by

$$V_{HS} = \frac{R_{VOL}}{R_{TH}}. \tag{3.4}$$

Here, V_{HS} describes the volume of the heat sink and R_{VOL} is the volumetric resistance. The new heat sink operates without a fan, such that heat is dissipated only via natural convection. Typically, the volumetric resistance with only natural convection lies between $500\,\mathrm{cm^3\,K\,W^{-1}}$ to $800\,\mathrm{cm^3\,K\,W^{-1}}$ [46]. In the worst case of $R_{VOL} = 800\,\mathrm{cm^3\,K\,W^{-1}}$, the required volume accounts to $V_{HS} = 270\,\mathrm{cm^3}$. The designed heat sink has a volume of $V_{HS} = 200\,\mathrm{cm^3}$ and is thermally coupled to its holding device.

The new controller board mount is sketched in fig. 3.3b and has direct contact with the APPS-FPGA. Since the original heat sink is glued to the FPGA, it has to be removed carefully using a razor blade. The remaining glue has to be removed by using isopropyl alcohol. Then, thermal paste is applied to the chip, and with three M2 screws, the mount is fixated on the chip. The screws are fastened evenly and such that the PCB does not bend. In the remaining M4 threads, a spacer with M2.5 threads can be screwed to securely attach the controller board. Note that for all screw connections isolating washers are recommended (Appendix B.1).

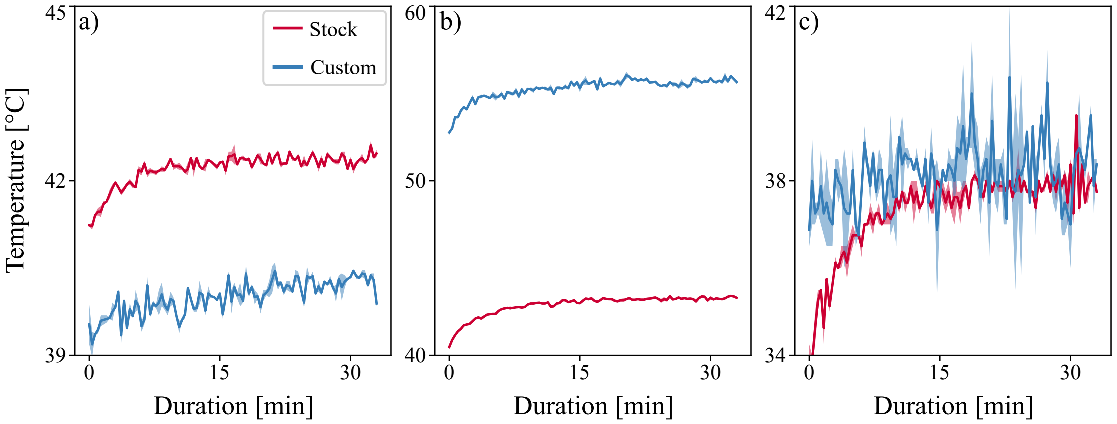

Figure 3.4: Temperature comparison of the stock cooler with the custom-designed, passive cooler (Fig. 3.3b). As a benchmark, a sequence of 380 images is loaded and then displayed for a total of 20 s on the DMD chip. This procedure is repeated 100 times, which takes 35 min. The controller board's temperature readout for the (a) APPS-FPGA, (b) DDC-FPGA, and (c) circuit board are compared.

The new mount was benchmarked by loading 380 images onto the DMD that were then displayed for a total of 20 s. This procedure was repeated 100 times and after each iteration, the temperature of the FPGAs was logged. In total, the benchmark takes approx. 35 min. The results are displayed in fig. 3.4 and were compared to the stock cooler. The APPS-FPGA that has direct contact with the board mount is approx. 2 °C cooler than with the stock design. However, due to the missing airflow, the DDC-FPGA is more than 10 °C warmer, when using the passive heat sink. The temperature on the circuit board is nearly identical. Since the FPGAs can operate up to a temperature of $T_{MAX} = 80\,°\mathrm{C}$, both heat sink designs provide sufficient cooling.

3.3.2 DMD Chip

The *DLP9000X* chip contains over 4 million micromirrors that can be individually addressed. They are arranged in an array of 2560×1600 micromirrors, illustrated in fig. 3.5a. By flipping the mirrors around the 45° tilted hinge axis, the state of the mirror can be changed. The illumination light is either projected into the output optics ("On-State") or beam dump ("Off-State") as sketched in fig. 3.5b. By setting a frame rate, the loaded DMD patterns are displayed for equal intervals in a loop. Alternatively, each pattern is displayed until an external trigger input is detected and the next image is loaded. A trigger event can be realized by a transistor-transistor logic (TTL) pulse (Appendix C.2).

The mirrors on the DMD chip form a blazed grating, which has maximum grating

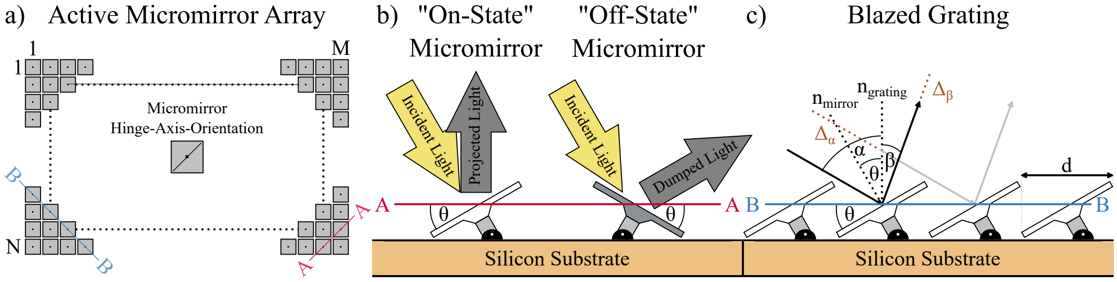

Figure 3.5: (a) Schematic of the active micromirror array with the hinge-axis orientation, (b) the micromirror states, and (c) the blazed grating. The normal vector of the mirror $\mathbf{n}_{mirror}$ differs by the tilt angle θ from the normal vector of the grating $\mathbf{n}_{grating}$. Adopted from [31].

efficiency for a given wavelength and diffraction order. At the same time, the power in the other orders is minimized. The grating equation reads

$$m\lambda = d(\sin\alpha + \sin\beta) \tag{3.5}$$

with diffraction order $m \in \mathbb{Z}$, wavelength λ, line spacing d, incident angle α and diffraction angle β. The maximum intensity for angle β is reached when the path difference $\Delta = \Delta_\alpha + \Delta_\beta$ is a multiple of the wavelength. The incident angle α and the diffraction angle β are connected via the mirror tilt θ of the chip by

$$\beta = -\alpha + 2\theta. \tag{3.6}$$

This is the only configuration where all phase differences of parallel rays nullify in infinity. The variables are all depicted in fig. 3.5c. If both, eq. 3.5 and eq. 3.6, are meet the maximum diffraction efficiency can be reached. For a planned diffraction angle of $\beta = 0°$ and the given mirror tilt of $\theta = 12°$, the illumination angle is defined as $\alpha = 24°$ according to eq. 3.6. With these angles, $d = \sqrt{2}{\times}7.6\,\mu\text{m}$, and wavelength $\lambda = 760\,\text{nm}$, diffraction order $m = 5.8$ contains the maximum. This does not satisfy eq. 3.5, which is more important than eq. 3.6, as the chip is much larger than a single mirror. Accordingly, a diffraction order of $m = 6$ and an incident angle of $\alpha = 25.1°$ provides the best fit and was used for the alignment.

3.4 Output Optics

The output optics have to demagnify the reflected beam to the size of the condensate. In the BECK experiment, the camera captures an area of approx. 470 µm × 470 µm, while the condensate has a diameter of approx. 60 µm. Thus, the demagnification has to be between 40 and 300, as it results in a beam size between those two measures. Due to the limited spatial resolution of the objective, the demagnification factor will set the number of grayscales, which defines how fine the local brightness on the DMD can be adjusted. Intuitively, the lower the resolution or the higher the demagnification, the more micromirrors cannot be resolved. The unresolved mirrors form a larger "superpixel", where each sub-mirror contributes to its overall brightness. Hence, the more mirrors are unresolved, the larger a "superpixel", which provides more grayscales.

The diffraction limit is given by

$$d = \frac{\lambda}{2 \cdot \mathrm{NA}} \tag{3.7}$$

with the wavelength λ and the NA of the optical path. In this setup, the objective with NA $= 0.5$ is the resolution limiting component. In the already implemented DMD setup, the output optics demagnifies the beam by a factor of 86.7, since it has to confine the atomic cloud laterally [47]. Two magnification stages are used to obtain a good beam quality. By magnifying in multiple steps, more conservative focal lengths can be chosen, which minimizes aberrations. First, a 4f-setup demagnifies by a factor of 4, then another 4f-setup including the high-resolution objective by a factor of approx. 21. This setup uses light with a wavelength of $\lambda = 532\,\mathrm{nm}$ and hence $d = 0.5\,\mu\mathrm{m}$. Accordingly, 6×6 mirrors are unresolved, allowing for 36 grayscales.

The second DMD will be used for local manipulations and optimizations of the trapping potential. A larger demagnification would allow for finer control by providing a larger number of grayscales. For the test setup, only the first 4f-setup with a demagnification factor of 4 was used, as no test objectives comparable to the high NA objective in the main experiment, were available. This is depicted in fig. 3.2d. After the telescope, a *Mako G-223 NIR* camera is placed to capture the modified beam. An iris in the 4f-setup allows us to simulate different NAs. Note that both, the camera and DMD chip, have to be placed in the focus of their respective lens. Without the objective, the resolution is limited by the camera sensor. In this configuration, a camera pixel images three DMD pixels. Consequently, 3×3 mirrors are unresolved, allowing for 9 grayscales. Depending on the use case in the main experiment, the second $f = 100\,\mathrm{mm}$ lens in the first 4f-setup can be swapped with a $f = 50\,\mathrm{mm}$ lens such that the demagnification factor doubles to 8. The second 4f-setup is identical to the first DMD setup with a demagnification of 21. In the experiment the resolution limit is $d = 0.76\,\mu\mathrm{m}$ at a wavelength of $\lambda = 760\,\mathrm{nm}$. With a total demagnification of 84, a block of approx. 9×9 mirrors

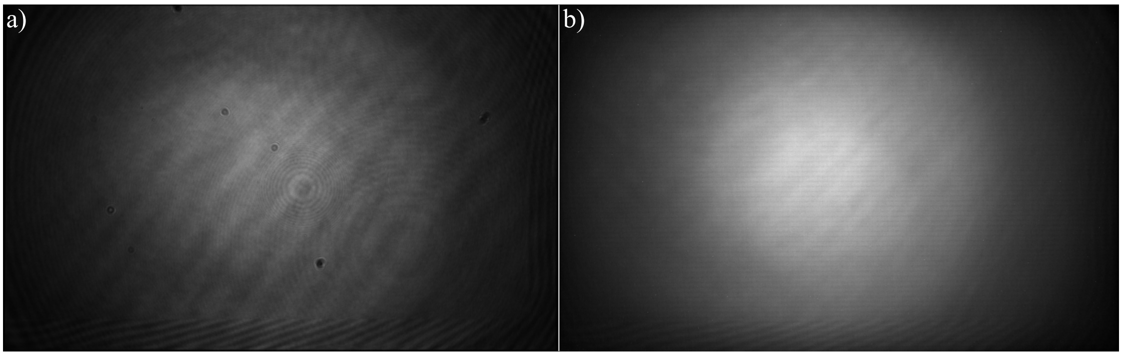

Figure 3.6: (a) Camera image of an all-white DMD pattern corresponding to all micromirrors in the on-state. (b) To avoid interference effects based on neighboring mirrors, the exposure time of the camera was increased from 1000 µs to 500 000 µs. Simultaneously, the display time of the DMD was set to 90 µs such that approx. 5500 DMD patterns per camera image are displayed. By displaying a sequence of 1000 patterns, where each pattern contains 5000 different mirrors in the on-state, effectively an all-white DMD pattern is created.

cannot be resolved, allowing for 81 grayscales. For a demagnification of 168, a block of approx. 17×17 mirrors cannot be resolved, allowing for 289 grayscales.

3.5 Results and Observations

The test setup was built without the second 4f-setup, as no high NA test objectives were available. Hence, the final demagnification and resolution could not be determined. However, a detailed characterization of a similar setup can be found in [47].

Interference patterns When all DMD mirrors are turned on as shown in fig. 3.6a, four different features are visible that disturb the image: First, the Gaussian shape of the incident light does not illuminate the DMD chip homogeneously. Second, diagonal interference stripes cover the whole chip area. Third, in the bottom and right part of the chip, an additional interference pattern is visible. Finally, dust particles sitting on the optics are distributed all over the micromirror array.

It is interesting to know, where and why these interference effects emerge and if they can be suppressed. By increasing the exposure time of the camera and turning all micromirrors on, one by one, interference effects of neighboring mirrors can be avoided. This is shown in fig. 3.6b, where the diagonal interference stripes as well as dust particles disappear. However, the stripes do not appear when illuminating only parts of the micromirror array, which is the most probable use case. The interference effects along the bottom and right side of the chip remain and are most likely caused by reflections on the frame of the DMD chip. This type of interference can also be observed in [27]. Nevertheless, the edges of the chip are non-critical areas regarding the typical application scenarios.

In conclusion, the Gaussian shape of the beam as well as the interference effects near the bottom and right edge are inevitable, while the dust particles can be removed and the interference stripes only appear when large areas of the chip are turned on at the same time. These effects are a good benchmark for the light-based feedback algorithm in sec. 4.1 as it has to cope with these imperfections.

3.6 Integration into the Main Experiment

To integrate the second DMD setup into the experiment, the test setup has to be moved onto the breadboard above the glass cell next to the first DMD setup, which was characterized in [47]. Figure 3.7a sketches the arrangement, where the components up to the first 4f-setup are used in the test setup (Fig. 3.2b-d) and were already discussed. Only the 90:10 beamcube has to be replaced by a beam sampler as discussed in sec. 3.2. The camera used in the test setup is replaced by a second 4f-setup consisting of a $f = 750\,\mathrm{mm}$ lens and the $f = 35\,\mathrm{mm}$ backfocus of the objective. The Fourier image must pass collimated and with maximal size through the objective, while the real space image has to be collimated at the atomic plane. Accordingly, the distances between the components are chosen, such that these three constraints are fulfilled. In this way, the cut-off frequency is maximized and the image on the atomic plane has the best resolution.

The beam radius in real and Fourier space throughout the full beam path is plotted in fig. 3.8a. To block all light in the Fourier plane that will not fit through the objective, the iris placed in the first 4f-setup has to be open by at least $2.3\,\mathrm{mm}$ in radius. All sketches are for a final demagnification of 84 as it requires the longest total beam path. However, the option to demagnify by a factor of 168 is still attainable by swapping the second $f = 100\,\mathrm{mm}$ lens in the first 4f-setup with a $f = 50\,\mathrm{mm}$ lens as discussed in sec. 3.4. In this case, the overall beam path is reduced by $100\,\mathrm{mm}$, which requires only small adjustments in the sketched arrangement (Fig. 3.7a). After the $f = 750\,\mathrm{mm}$ lens, the beam passes through a hole in the breadboard to reach the objective. The vertically mounted optics to overlap both DMD beams as well as the imaging and MOT beams are depicted in fig. 3.10 showing several modifications compared to the previous setup in fig. 3.9.

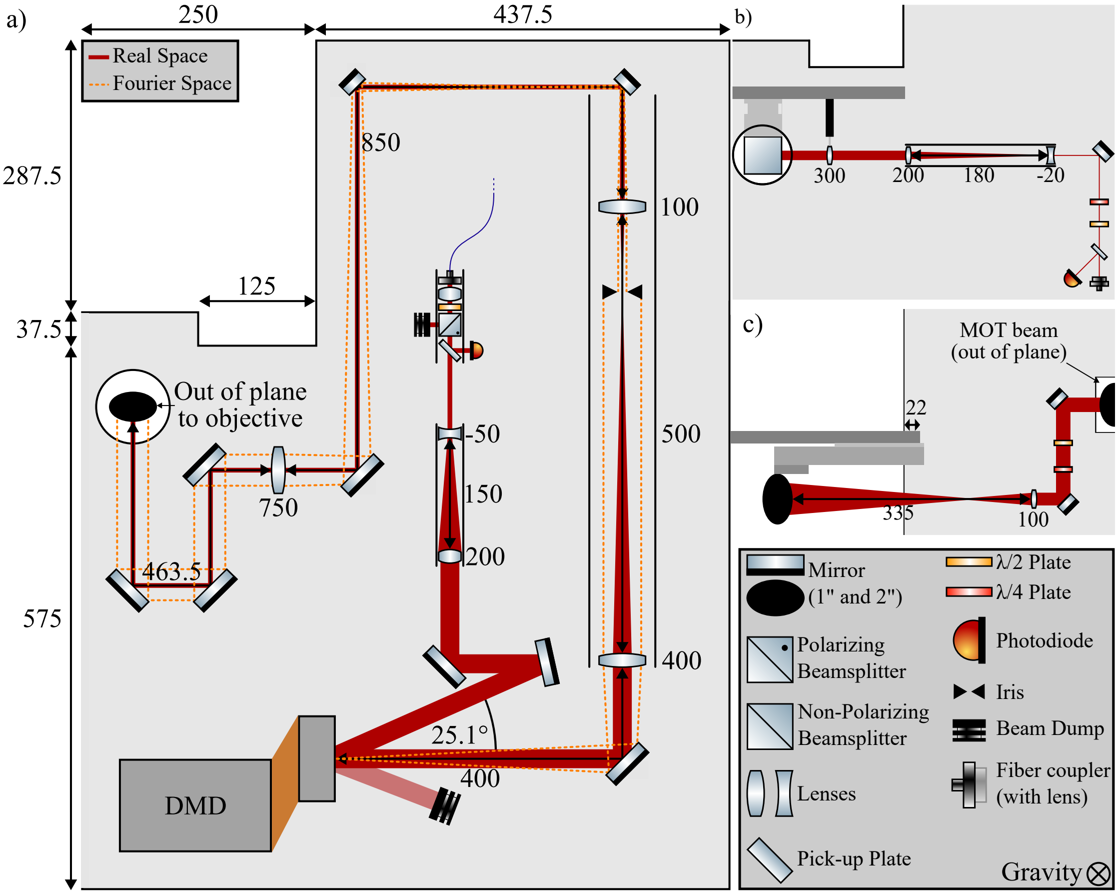

Figure 3.7: (a) DMD setup on the breadboard above the glass cell. The breadboard extends further to the left, where the first DMD setup is located. To fit the additional DMD beam into the objective, (b) the imaging and (c) the MOT beam path have to be modified. The imaging optics remain mounted directly below the DMD breadboard, while the MOT optics are moved to a lower breadboard. The distances and focal lengths are given in millimeters and are drawn to scale. If not specified, the exact position of the components is not critical.

The beam path of the first DMD setup indicated in green remains unchanged. The second DMD beam has to be overlapped with the already overlapped imaging and MOT beam by using a 50:50 beamcube. Due to the large Fourier image of the DMD beam, a 2 inch beam cube is required that is glued to a pedestal mounting cube (Appendix B.5). However, two problems arise: First, the MOT and imaging beam power have to be doubled since the beamcube reflects only 50 % of the light into the objective. While this is feasible for the imaging beam, the MOT beam power cannot be doubled. Second, the $f = 75\,\mathrm{mm}$ MOT lens would affect the DMD beam shape. The lens cannot be easily compensated due to the three constraints of the DMD beam at the back focus of the objective. Therefore, the imaging and MOT beam paths have to be separated. As sketched in fig. 3.7c, the MOT optics have to be mounted to the lower breadboard with a

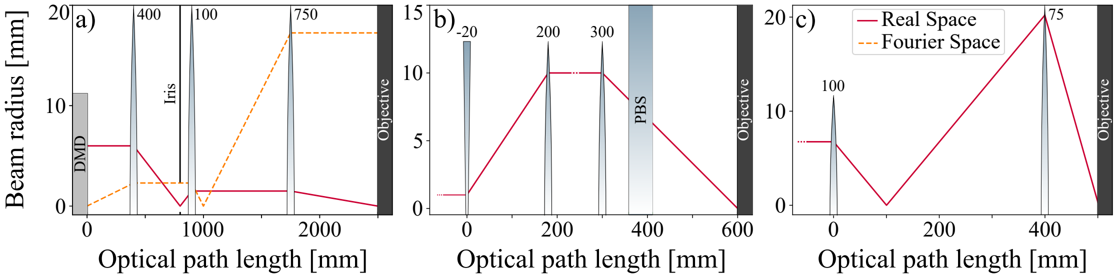

Figure 3.8: The beam path of (a) the second DMD setup, (b) the modified imaging setup, and (c) the moved MOT setup. The beam starts collimated from the left, directly after the DMD chip/fiber coupler. For simplicity, only relevant optical components are included to estimate the beam diameter in real and Fourier space before entering the objective. All beams are collimated after the objective and are magnified by a factor of (a) $\frac{1}{84}$, (b) 1.17, and (c) 1.16.

new beam height of 14 cm. Since the MOT beam is only needed at the beginning of an experimental sequence, before the DMD and imaging light, part of the MOT optics are placed on a translation stage, such that it can be moved in and out of the main beam path. The MOT lens and a mirror are mounted onto an adapter plate (Appendix B.7) and the translation stage can be extended and contracted by applying a TTL pulse (Appendix C.3). The position of the translation stage is depicted in fig. 3.10. In this way, the optical path of the MOT beam displayed in fig. 3.8c, remains unchanged.

In the previous setup depicted in fig. 3.9, the imaging beam path also used the MOT lens, as it had the same lens configuration as the MOT setup. Now that the MOT lens will be retracted from the main beam path during the imaging, the imaging setup has to be adapted. The new optical beam path is illustrated in fig. 3.8b. The previous lens configuration comes close to a 1:1 telescope, which is maintained in the new setup. Additionally, the first optical component has to be placed after the 50:50 beamcube in fig. 3.10. Hence, a $f = 300\,\text{mm}$ lens forms a 4f-setup with the $f = 35\,\text{mm}$ backfocus of the objective demagnifying the imaging beam by a factor of 8.6. Accordingly, a Galilean telescope with a magnification of 10 is placed before the 4f-setup to achieve a magnification of 1.17 after the objective. Except for the Galilean telescope, the optical components and their beam height of 8 cm remain the same, which is shown in fig. 3.7b. The imaging setup is still mounted underneath the DMD breadboard but it has to be rearranged to fit the telescope.

To implement the upgrade minimally invasive, the order of the modifications is important. First, the DMD setup can be assembled on the breadboard above

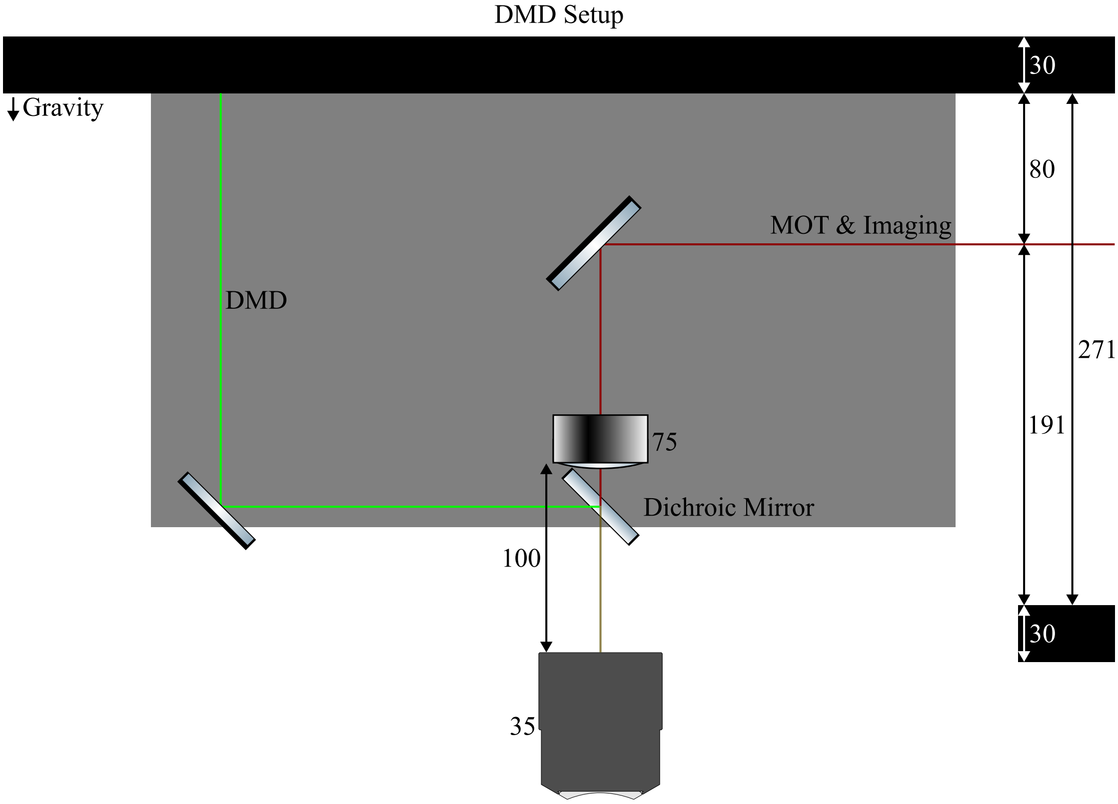

Figure 3.9: Vertical beam path above the glass cell for the single-DMD setup. The sketch contains the last section of the MOT and imaging beam path (red), as well as the DMD path (green) before entering the objective. While the 532 nm light is reflected, all other beams are transmitted by the dichroic mirror. The distances and focal lengths are given in millimeters and are drawn to scale.

the glass cell without affecting the working setup. Then, the MOT lens on the vertical breadboard and an empty mirror mount can be placed onto the translation stage. Here, the imaging and MOT beam can be used to align the extended translation stage. If properly aligned, the experiment will be still functional. Next, the mirror that guides the imaging and MOT beam toward the objective can be replaced by the beamcube. Again, the imaging and MOT beam can be used for the alignment, since their beam position after the beamcube should be maintained. Additionally, the DMD beam coming from the top has to pass straight through the cube. After the reduced power in the MOT beam is compensated by rebalancing the top and bottom beams, the experiment should again be functional. This step can be skipped because the imaging and MOT setup have to be separated and rebuilt. The measurements in fig. 3.10 are provided with millimeter precision. However, due to the limited accessibility of the breadboard, the measured MOT lens position might deviate by several millimeters, which affects the MOT beam height, as well as the position of the imaging and DMD output optic lenses. This

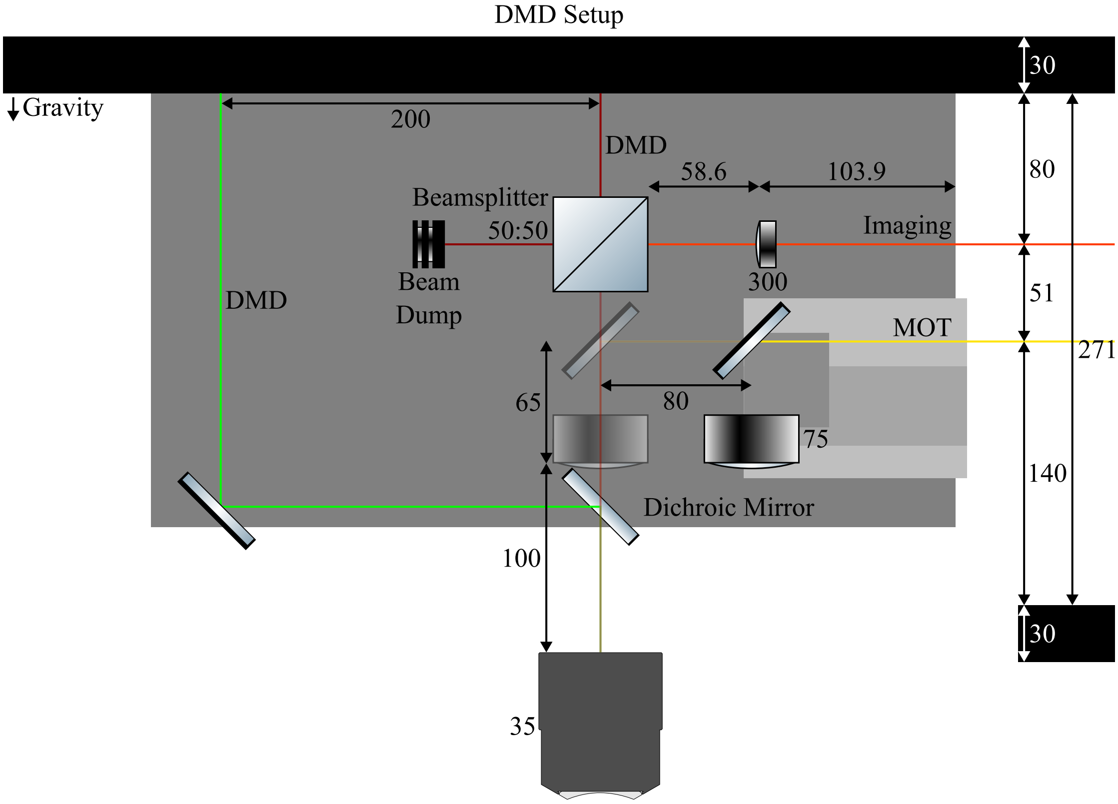

Figure 3.10: Vertical beam path above the glass cell for the dual-DMD setup. The sketch contains the last section of the imaging (orange) and MOT (yellow) beam path, as well as both DMD (green, red) paths before entering the objective. The green DMD path remains unchanged. While the 532 nm light is reflected, all other beams are transmitted by the dichroic mirror. The MOT lens and a mirror are mounted onto a translation stage, indicated in light gray that can be moved in and out of the main beam path. The second DMD beam is overlapped with the imaging beam by using a 50:50 beamcube. The distances and focal lengths are given in millimeters and are drawn to scale.

was considered throughout the planning process such that all mounting hardware comes with adequate margins.

4 Optimization Algorithm

As discussed in the previous section, the optical system of the DMD setup was planned carefully. However, imperfections in the illumination beam and optical system like aberrations or dust cannot be avoided completely and modify the expected potential. In the particular case of the BECK experiment, the glass surface of the science chamber is not coated with an anti-reflective coating, resulting in interference effects on the atomic plane. These imperfections can be corrected by a feedback algorithm that is either based on the light or the atomic signal. The light-based feedback algorithm corrects the projected light beam before entering the science chamber. It is comparatively quick as it is only limited by the time of taking and transferring the image to the computer. However, the additional imaging system might add imperfections that are not seen by the atoms. For the atom-based feedback algorithm, the reaction of the atoms to the potential is measured, so the projected light beam is corrected indirectly. Here, a BEC has to be produced, prepared in the given potential, and imaged. This process takes significantly longer, though, the effect on the condensate is corrected, which is the measured quantity. Figure 4.1 illustrates the overall structure of the two algorithms. The structure and some parts of the algorithm were inspired by [27].

First, the algorithm has to be initialized by either calibrating the mapping between the camera and reference image or by loading the parameters from a file. Then, the target image has to be selected and the corresponding initial DMD sequence is prepared. Next, the algorithm enters the optimization routine that starts by loading the latest DMD sequence to perform the experiment. For the light-based approach, the experiment consists of light propagating to the camera, while a BEC experiment has to be conducted for the density-based approach. After the camera image has been mapped and normalized to the reference image, the optimization begins. Based on an error map, a corresponding mirror flip map is calculated and used to prepare a new DMD sequence. With each iteration, the camera image converges to the reference image until the error in the error map is minimized.

For a consistent notation, an image is defined as $p(x, y)$ with size $M \times N$. The x-direction describes the width of the image with a total of M pixels, while the y-direction defines the height of the image containing N pixels (Fig. 3.5a).

In this section, both feedback algorithms are introduced. The light-based feedback algorithm serves as a proof of concept and was designed for the test setup, while the density-based feedback algorithm is intended for the main experiment.

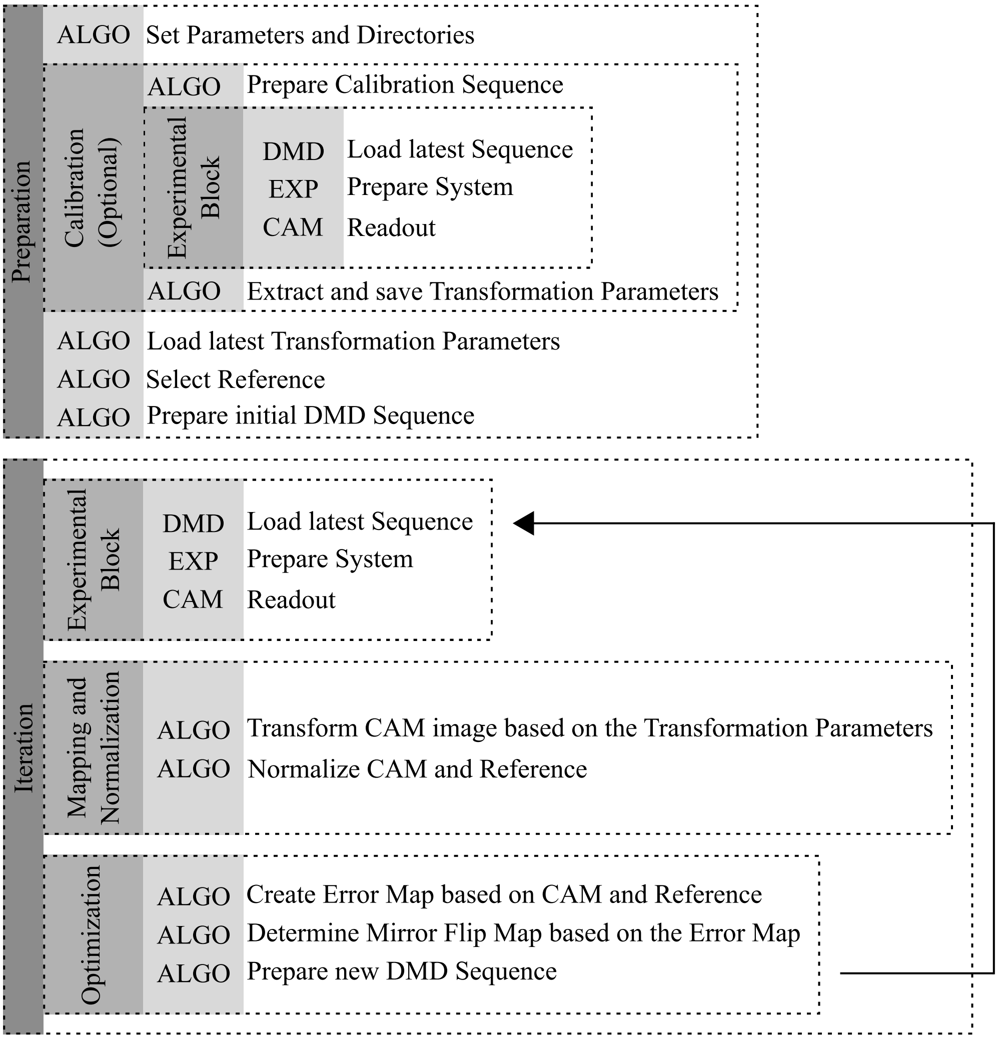

Figure 4.1: Schematic of the optimization algorithm. Both algorithms follow this framework. It can be divided into two parts: The initialization of the algorithm including the calibration of the mapping, and the iteration steps of the optimization routine. The component that executes the step is marked in light gray. They are labeled as DMD control (DMD), camera control (CAM), experimental sequence control (EXP), and optimization algorithm (ALGO).

4.1 Light-Based Feedback Algorithm

As a first proof of principle, a light-based feedback algorithm for the test setup, illustrated in fig. 3.2, is realized. Here, a single DMD image based on an 8-bit reference image is optimized, by analyzing the intensity distribution of the projected beam. Therefore, the beam is captured by a camera and the resulting image is compared to the reference image. This section describes the realization of each step in fig. 4.1 for this particular use case. First, the initialization of the algorithm is explained, followed by the optimization routine. Next, results and observations are discussed and lastly, the methods are described.

4.1.1 Initialization

As indicated in fig. 4.1, the algorithm starts with the calibration, if no suitable set of transformation parameters exists. These parameters determine the mapping between the camera and the reference image. The calibration has to be done once during the preparation of the algorithm. Alternatively, the transformation parameters are loaded from a file.

Calibration The mapping consists of a similarity transformation allowing for translation, rotation, and scaling. By using homogeneous coordinates, so representing the vector (x, y) as $(x, y, 1)$, the transformation can be described by the matrix

$$\mathbf{A} = \begin{bmatrix} s_x & 0 & 0 \\ 0 & s_y & 0 \\ 0 & 0 & 1 \end{bmatrix} \begin{bmatrix} \cos\theta & -\sin\theta & 0 \\ \sin\theta & \cos\theta & 0 \\ 0 & 0 & 1 \end{bmatrix} \begin{bmatrix} 1 & 0 & t_x \\ 0 & 1 & t_y \\ 0 & 0 & 1 \end{bmatrix} . \tag{4.1}$$

Here, s_x and s_y are the scaling factors in x- and y-direction, respectively, and in our case $s_x = s_y = s$. The angle of rotation is denoted as θ, while t_x and t_y describe the translation in x- and y-direction, respectively. First, a unique calibration pattern has to be created. Three dots that form a scalene triangle, as shown in fig. 4.2a, allow us to perform an explicit similarity transform. These are the minimal number of points needed for a unique transformation. However, any other number of points that form a convex hull with no rotational symmetry will work, as it connects the edges in a distinct order. Then, the corresponding DMD pattern has to be loaded onto the device and a camera image is taken. This procedure belongs to the experimental block and will be explained in the next section. To find the exact transformation parameters, a fast Fourier transform (FFT) based image registration algorithm[3] was used. To work reliably, the calibration pattern is transformed to match the camera image, based on an initial guess. First, the scaling parameter can be estimated by

$$s = \frac{P_{DMD}}{P_{cam} \cdot M_{DMD} \cdot M_{cam}}, \tag{4.2}$$

where P_{DMD} and P_{cam} describe the pixel size, while M_{DMD} and M_{cam} are the magnification of the DMD and camera sensor, respectively. Here, $P_{DMD} = 7.6\,\mu\text{m}$, $P_{cam} = 5.5\,\mu\text{m}$, $M_{DMD} = 0.25$ and $M_{cam} = 1$, yielding $s = 5.5$. The angle of rotation can be estimated by a visual judgment of a test image. Finally, the image is padded

---

[3] github.com/matejak/imreg_dft

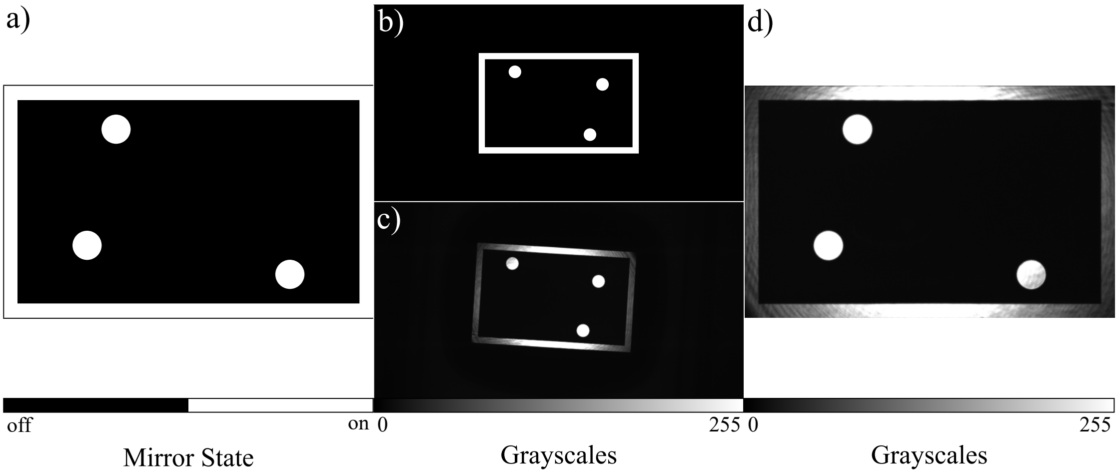

Figure 4.2: (a) The 1-bit DMD calibration image, (b) the initial guess, (c) the corresponding camera image, and (d) the transformed camera image. The camera image (2048 px × 1088 px) is mapped onto the DMD pattern (2560 px × 1600 px).

to match the size of the camera image. Note that the center of the calibration image has to be maintained during the padding. The initial guess in fig. 4.2b and the camera image in fig. 4.2c are already close to each other, simplifying the registration process. However, the transformation using only three dots did not work reliably. Therefore, a box around the DMD chip was added. Furthermore, the exposure time of the camera was increased to provide a higher contrast of the pattern. This improved the reliability, yet, the module still randomly failed to find the correct transformation. Due to the limited amount of tuning parameters, the function could not be tweaked to prevent this behavior. Another constraint was the duration of approx. 18 s for the calibration with the main contribution stemming from the registration algorithm. As a consequence, the calibration scheme was changed in the density-based feedback algorithm. With the transformation parameters used in the initial guess, as well as the corrections found by the registration algorithm, the mapping can be determined. The transformed camera image is displayed in fig. 4.2d. After the mapping, the camera image has the same size as the DMD image. Since the test setup is fairly stable, the transformation parameters are saved and can be used until the setup is modified.

Next, an 8-bit reference image has to be selected that represents the targeted intensity distribution of the projected beam. On the reference image, the Floyd-Steinberg dithering [22] is applied to produce an initial 1-bit DMD pattern. The reference image will not be modified during the optimization process, while the 1-bit DMD pattern is modified in every iteration. Optionally, a mask can be selected to exclude areas from the optimization process. It is a logical array with the same

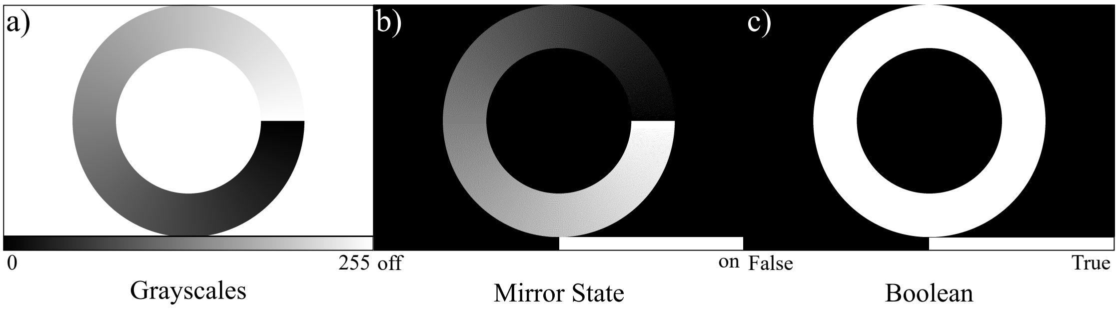

Figure 4.3: A set of (a) 8-bit reference image, (b) 1-bit DMD pattern, and (c) mask (optional) to initialize the optimization process with a size of 2560 px × 1600 px. By applying the Floyd-Steinberg dithering to the reference image, the 1-bit pattern (b) is created. In the digital version, the dither can be observed by zooming in.

size as the DMD pattern and only pixels with a logical one will be considered during the optimization. To evaluate the feedback algorithm, an angular intensity gradient going from 0 % to 100 % with finite width is used. This pattern is displayed in fig. 4.3a with its corresponding 1-bit pattern in fig. 4.3b. The mask shown in fig. 4.3c only serves as an example and was not used during the optimization. The described gradient is a challenging pattern for the DMD as the beam intensity has to increase linearly with the angle while staying constant radially. Moreover, there are intensity steps between the start and end point of the gradient, as well as the ring and background. These features are of interest when assessing the performance of the feedback algorithm. Before the first optimization iteration, a dark image is taken, where all DMD pixels are turned off.

4.1.2 Iteration

In this section, an iteration of the optimization routine is discussed. As represented in fig. 4.1, the iteration is divided into three parts:

Experimental Block In the experimental block, the DMD loads the latest sequence. Then, the experiment is conducted to acquire a camera image. For the light-based algorithm, the experiment consists of the propagation of light from the DMD chip to the camera sensor. Since the illumination beam is permanently turned on, the projected beam resulting from the latest DMD pattern can be instantly captured by the camera. Hence, the system is always prepared. All images are taken with the same camera settings. This ensures that the camera images are comparable. As discussed in sec. 3.5, the intensity of the illumination light decreases radially towards the edges of the DMD chip. This limits the dynamic range available to the algorithm, locally. Therefore, the algorithm works best when starting with more intensity than needed, even if the camera image ends up being slightly oversaturated in some areas. All in all, the experimental block takes approx. 2.5 s.

Mapping and image normalization The next step in fig. 4.1 comprises the mapping of the camera to the DMD image and its normalization to the reference image. First, the camera image has to be mirrored. Then, the mapping is applied to the camera image based on the transformation parameters from the calibration. This operation is performed by the registration module. Next, the camera and reference image have to be normalized. This process allows us to compare and analyze images from different sensors or cameras. Furthermore, it creates relative signals, which are not affected by intensity fluctuations. A combination of range normalization and midway equalization is suggested by [27], which did not work well. Instead, only a range normalization is implemented. The range normalization ensures that the minimum and maximum pixel values of the compared images are the same. Since both, the reference and camera image, have the same range of 255 gray values, only the reference image $p_R(x,y)$ is range normalized to a value $I_{max} \leq 255$ according to

$$\hat{p}_R(x,y) = \frac{I_{max}}{max[p_R(x,y)]} p_R(x,y). \tag{4.3}$$

This prevents that the targeted pattern saturates the camera, as the exposure time and gain of the camera are held constant. Finally, the mean of the dark image is subtracted from the camera image. The mapping and normalization process takes approx. 5.6 s, where again the registration module is the main constraint.

Optimization Now, the final step in the iteration process, illustrated in fig. 4.1, is reached. By subtracting the reference image $\hat{p}_R(x,y)$ from the transformed camera image $p_{cam}(x,y)$ and dividing the result by I_{max}, the local error can be calculated conforming to

$$\epsilon(x,y) = \frac{p_{cam}(x,y) - \hat{p}_R(x,y)}{I_{max}}. \tag{4.4}$$

The error map $\epsilon(x,y)$ takes values in the interval $[-1,\ 1]$, where positive values indicate too much light on a camera pixel and negative values the opposite. In fig. 4.4c, the error map of the initial gradient pattern is shown, while fig. 4.4g presents the error map after 10 iterations. In the next section, a detailed discussion of the error map can be found. By multiplying a global factor α to the absolute of

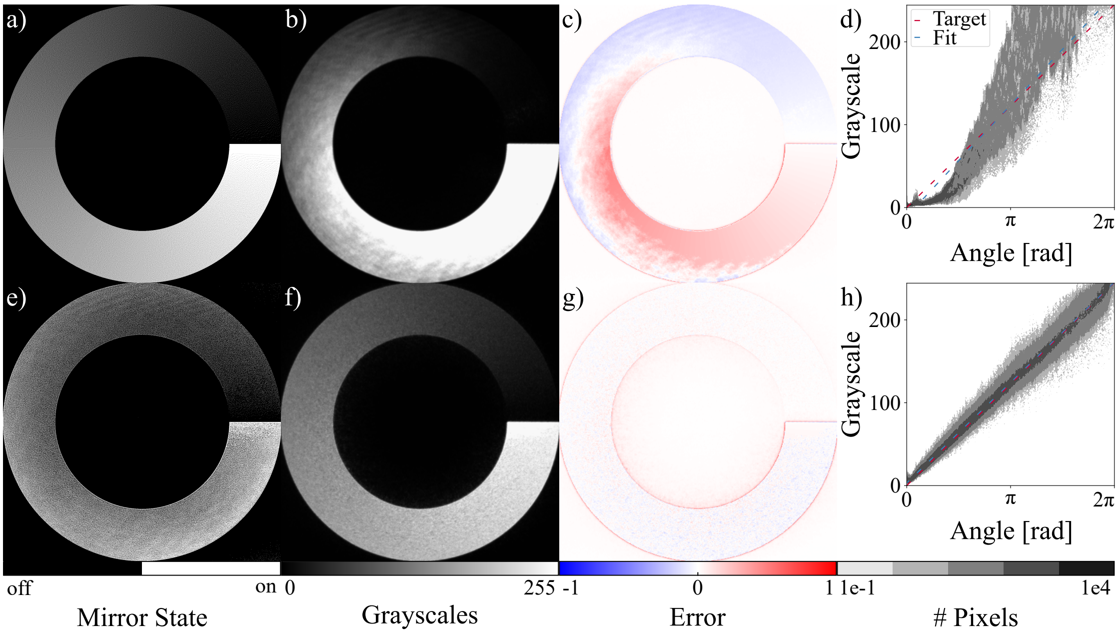

Figure 4.4: Comparison of the (a) initial DMD and (b) camera image with an (e) optimized DMD and (f) camera image after 10 iterations. The 8-bit, target image is shown in fig. 4.3a. Here, the region of interest is reduced to 1600 px × 1600 px. The corresponding error maps of the initial and optimized camera image are presented in (c) and (g), respectively. The angular decompositions of the camera images are displayed in (d) and (h), where only the white area of the mask in fig. 4.3c was evaluated. Note that the color bar is logarithmic. Inspired by [27].

the error map $|\epsilon(x, y)|$, the mirror flip probability is calculated. The parameter α can be adjusted to tune the step size of the optimization procedure by modifying the mirror flip probability. While an $\alpha > 1$ can increase the convergence speed, it can also increase the influence of noise. In contrast, $\alpha < 1$ can decrease the convergence speed but can reduce the influence of noise. For $\alpha > 1$, the mirror flip probability can also reach values larger than one. These values are treated as a one, which means that the mirror will be flipped. At default, α is set to one. To generate a new image, the mirror flip probabilities $\alpha|\epsilon(x, y)|$ are compared to a random number array of the same size and a range of $[0,\ 1]$. If the absolute error is larger than the corresponding random number, the mirror will be flipped, which is denoted in a logical array as depicted in fig. 4.5a. This ensures that, on average, a fraction proportional to the measured error in the corresponding area of mirrors is flipped. At the same time, the randomness of the process should prevent the build-up of structure introduced by the optimization algorithm. As discussed in the next section, this only works if individual mirrors are not resolved. Additionally, it will be checked, whether a mirror flip will reduce the error. The corresponding logical array is displayed in fig. 4.5b. For example, a turned-off mirror in an area that is

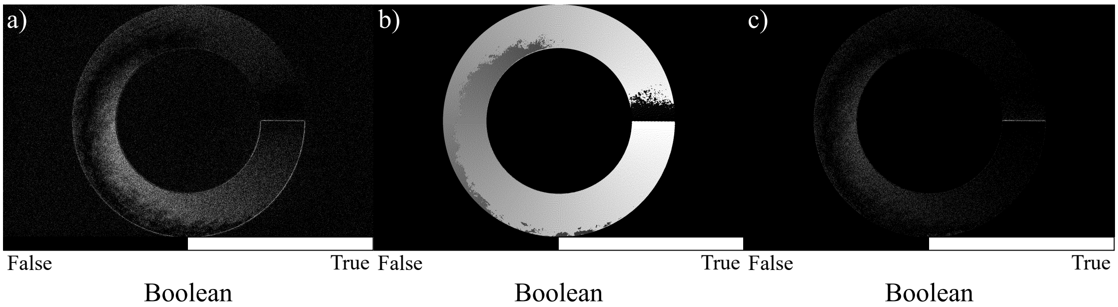

Figure 4.5: Flip maps for the initial DMD pattern (Fig. 4.4a). (a) The mirror flip probability $\alpha|\epsilon(x, y)|$ is compared to a random number array with interval [0, 1]. If $\alpha|\epsilon(x, y)|$ is larger than the random number, the mirror will be flipped. (b) Only mirrors that reduce the error $\epsilon(x, y)$ are considered. (c) Both logical arrays, as well as the optional mask (Fig. 4.3c), are combined with a logical "and". The resulting logical array depicts all mirrors that will be flipped in the first iteration (approx. 50 000). For this pattern, the region of interest can be reduced to 1600 px × 1600 px.

already too bright, will not be flipped. These two logical arrays and the mask will be combined with a logical "and" to give the final flip map. An example of the combined arrays is shown in fig. 4.5c for the initial gradient pattern (Fig. 4.4a-d). The final array, e.g. in fig. 4.5c, and the 1-bit DMD pattern are combined using the XOR operation, which results in an optimized pattern. One optimization iteration takes approx. 1.5 s.

This pattern is then saved and the next iteration starts with the experimental block indicated in fig. 4.1. In total, the calibration takes approx. 18 s and every iteration approx. 9.6 s. However, this algorithm was not optimized for speed. E.g. approx. 5 s per iteration could be saved by replacing the transformation function of the image registration module with a function that applies matrix 4.1 to the camera image.

4.1.3 Results and Observations

Now that the optimization algorithm has been introduced, the performance evaluation of the algorithm for the more general problem of the gradient pattern is put forth. Then, a special application of the algorithm is presented. Finally, a specific artifact, as well as a pattern formation phenomenon that was observed, while using the algorithm, are discussed.

Gradient To evaluate the outcome of the optimization iteration, the number of flipped mirrors, as well as the average error and standard deviation of the error map are logged in each iteration. The error map can be calculated for arbitrary

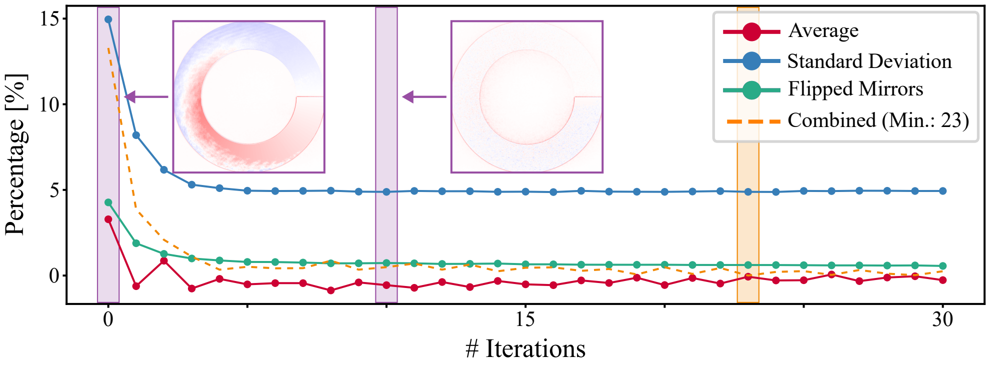

Figure 4.6: Average error and standard deviation of the error map, as well as the fraction of flipped mirrors for the gradient (Fig. 4.3) over 30 iterations. The sum of the average and standard deviation subtracted by their means provides the combined graph. The iteration with the lowest combined value is marked in orange. The insets (violet) display the error map of the marked iteration.

reference patterns and is calculated in each iteration. Therefore, it is an useful tool to evaluate the optimization. Since the error map is normalized to $[-1,\ 1]$, the average and standard deviation can be interpreted as percentual deviations from the target image. Figure 4.6 presents those values for the gradient pattern (Fig. 4.3a) over 30 iterations. After six iterations, the algorithm converges and the logged values remain constant. More precisely, an average of -0.004 and a standard deviation of 0.05 are reached, while the number of flipped mirrors converges to 20 000. This means that on average the camera pixel values do not deviate from the values of the reference, while the individual pixel values deviate by 5 % in the one sigma range. Although, the global minimum is reached as late as after 23 iterations, this value deviates only slightly from the sixth iteration. Beyond the convergence point, the average value of the error map starts to oscillate around zero, which is in accordance with the constant number of mirror flips. As mentioned in sec. 3.4, the DMD can only adjust the intensity in discrete steps, depending on the number of grayscales. Thus, the algorithm might oscillate around the targeted intensity, without being able to reach the exact value. Since the resolution of the test setup is not limited by the objective, approx. nine grayscales can be produced as discussed in sec. 3.4. Figure 4.4 depicts the initial state, as well as the tenth iteration, which will be discussed in more detail. In the first iteration, the error map has an average of 0.03 and a standard deviation of 0.15. Consequently, approx. 110 000 mirrors have to be flipped. After 10 iterations, the average and standard deviation are reduced to -0.006 and 0.05, respectively. Here, around 19 000 mirrors should be flipped. This is an improvement of factor five concerning the average and a factor of three on the standard deviation. The optimized error map does not show any radial dependency and hence, the Gaussian shape of the illumination beam can be compensated without any problems. Furthermore, the interference effects at the bottom of the chip that were described in sec. 3.5 are countervailed by an inverse mirror fraction pattern, visible in the upper part of fig. 4.4e. In contrast, the edges of the pattern are particularly hard to optimize, since the intensity has to change instantaneously. To create sharp edges, high frequencies are needed to allow abrupt intensity changes. Therefore, a high resolution is needed because the optical system characterized by the imaging response function, acts like a low-pass filter. The high resolution contradicts the capability of grayscaling, such that an appropriate balance of both properties has to be found. Normally, the resolution is set by the optical components such that both values are fixed.

Until now, only the error map was considered to evaluate the success of the optimization. However, in the particular case of the gradient pattern, the angular intensity gradient is an important feature. Hence, fig. 4.4d and h depict the angular decomposition of the two camera images. In contrast to the initial pattern, the intensity gradient of the optimized pattern does follow the targeted linear slope. The mean deviation from the ideal curve with its standard deviation yields the same values as the error map. Consequently, the radial decomposition is also a suitable benchmark for optimization success but could only be used in this particular case.

The convergence behavior in fig. 4.6 is also observed for other DMD patterns. Accordingly, around ten iterations are recommended to achieve the best result. The whole process with calibration will then take around 120 s.

Flat-top potential For many optical applications, flat-top laser beams are important and many DMD patterns contain flat-top structures. Yet, the DMD is illuminated by a Gaussian beam leading to an inhomogeneous intensity pattern. The flatness of the wavefront can be quantized by the RMS error given as

$$RMSE = \sqrt{\frac{\sum_{i,j}[\,\hat{p}_R(i,j) - p_{cam}(i,j)]^2}{MN}}. \tag{4.5}$$

The RMS error describes the mean deviation between the camera and reference image in terms of grayscales. By normalizing the RMSE according to

$$NRMSE = \frac{RMSE}{max[p_{cam}(i,j)] - min[p_{cam}(i,j)]}, \tag{4.6}$$

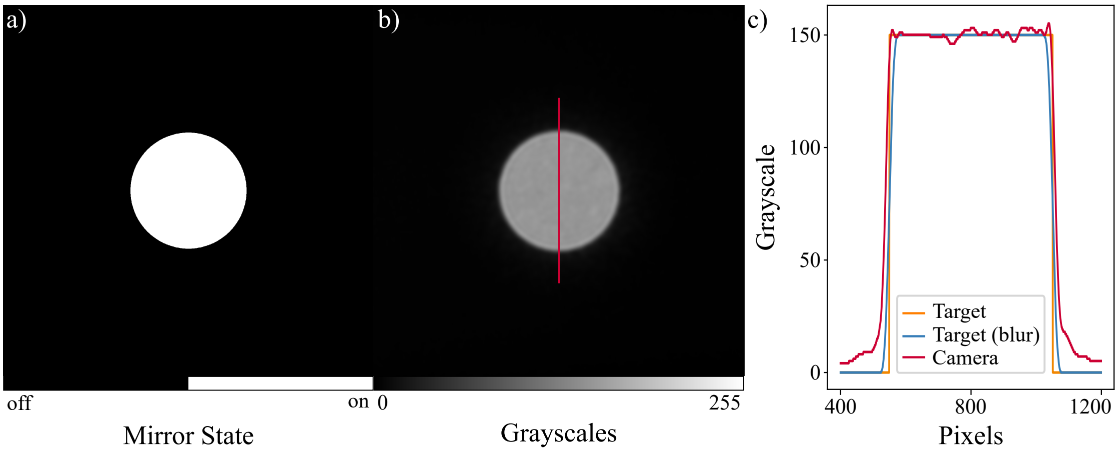

Figure 4.7: (a) A 1-bit DMD image of a dot with a diameter of 500 px and (b) the transformed camera image of the 24th iteration. A Gauss filter ($\sigma = 10$) was applied to the camera image before the optimization and I_{max} was set to 150. The red line in (b) marks a single pixel cut through the middle of the dot. (c) The camera cross section is compared to its targeted shape with and without the Gauss filter.

the deviation can be expressed as a relative number. The NRMSE corresponds to the standard deviation of the error map $\epsilon(x, y)$. For example, an NRMSE of 4.9 % is reached for the gradient pattern after ten iterations as discussed in the previous section. However, this pattern is not the best example of a flat-top potential. Accordingly, a simple point with a diameter of 1 mm at the camera sensor was chosen as depicted in fig. 4.7a. For this pattern, I_{max} was set to 150 to be far from saturation and α to 0.5 to ensure convergence and to reduce noise. With this setup, the optimization algorithm can reach an NRMSE of 7.5 %. As previously discussed, the test setup has a high resolution and consequently, a very limited number of grayscales. To simulate the objective, a Gauss filter with $\sigma = 10$ was applied to the camera image. This increases the number of grayscales from nine to 81 grayscales. This allows us to reach an NRMSE of 1.8 %. The respective camera image and a cross-section of the beam profile are presented in fig. 4.7b and c. There are error-diffusion algorithms for binary-amplitude spatial light modulators that can reach NRMSEs better than 1.5 % [35]. With a very similar DMD setup, an NRMSE of 1.25 % was reached in [8] by adapting the error-diffusion algorithm.

Contrast Some patterns require high contrast. However, the imaging response function of the optical system limits the variation of the intensity. The optical system acts like a low-pass filter and cuts off the high frequencies necessary for an abrupt intensity change. To produce sharp edges with only lower frequencies, an overshoot and undershoot around the jump point arises. This behavior is called the Gibbs phenomenon [5] and is usually undesirable as it can cause clipping

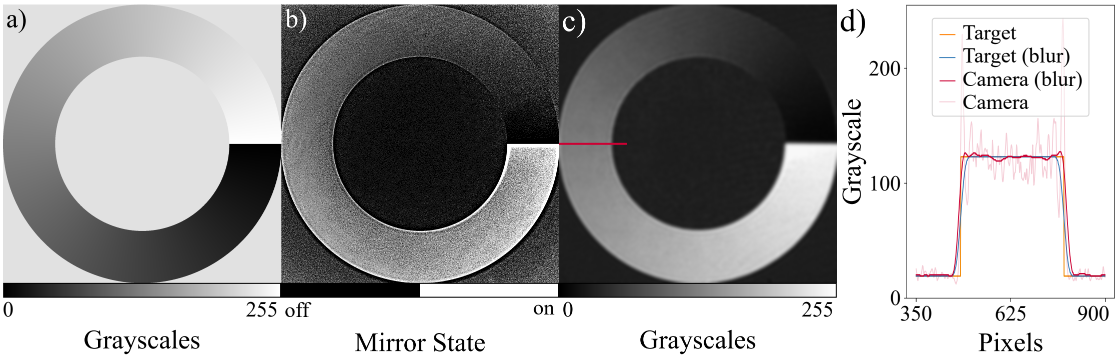

Figure 4.8: (a) The 8-bit reference image of the gradient with a background offset of 20, (b) the corresponding DMD, and (c) camera image after ten iterations. A Gauss filter ($\sigma = 10$) was applied to (c) before the optimization. (b) shows strong ringing artifacts that are not visible in (c) due to the Gauss filter. The red line in (c) marks a single pixel cut through the gradient depicted in (d). In (d), the camera and target cross sections with and without a Gauss filter ($\sigma = 10$) are compared. The overshoots and undershoots produce steeper edges compared to the blurred reference.

and ringing artifacts. Figure 4.8b shows such ringing artifacts on the optimized DMD pattern when a Gauss filter is applied to the camera images. Here, the reference image in fig. 4.8a has a background offset of 20 grayscales to also allow undershoots. The background of the optimized DMD pattern (Fig. 4.8b) nicely shows, how the algorithm compensates the Gaussian shape of the illumination beam. On the Gauss-filtered camera image in fig. 4.8c, the ringing artifacts are not directly visible. However, the cross-section of the blurred camera image in fig. 4.8d reveals slight over- and undershoots near the edge. The over- and undershoots of the original camera image are significant. For most use cases, high contrast is more important than reducing ringing artifacts. Due to these artifacts, the acutance can be even higher than in an ideally blurred image, which can be considered as an enhancement. This effect can be observed in the cross-section plot by comparing the Gauss-filtered target with the blurred camera image. Alternatively, the borders of the reference image can be smoothed such that no oscillations occur, while maintaining the highest contrast possible as presented in [8]. By implementing an edge detection method, this border smoothening could be applied to arbitrary DMD patterns. Yet, the emphasis of this optimization routine was laid on being as unconstrained as possible.

"Dunes" Sometimes, the algorithm creates high-contrast ripples on the optimized DMD images that move and spread over the rest of the pattern with each iteration. Because their shape and movement with every iteration resembles the flow of sand in the wind this feature was named "Dunes". These stem from errors in the calibration of the translation parameter, such that the algorithm corrects the wrong pixels on the DMD. Ergo, the actual error is not fixed, while a new, opposed error arises next to it. This is repeated with each iteration leading to a propagation of the ripples, as well as an increment in the contrast. In fig. 4.9, the dunes are shown for an artificial translation in x and y, respectively. Intuitively, this phenomenon can be understood in terms of the resolution limit in the camera frame d_{cam}. So, how many DMD pixels are mapped to one camera pixel times how many DMD pixels are indistinguishable. We define that two DMD pixels can be distinguished if the convolution of their corresponding delta peaks with the simulated imaging response function shows a minimum in between the two peaks. If the calibration error of the translation parameter is larger than d_{cam}, "Dunes" arise. The sensitivity of the translation alignment can be estimated by

$$\Delta \approx d_{cam} = \frac{P_{cam} \cdot d_{DMD} \cdot s}{P_{DMD}}, \tag{4.7}$$

where Δ is the maximum shift of DMD pixels, before "Dunes" arise, P_{cam} describes the camera pixel size, d_{DMD} is the number of indistinguishable DMD pixels, s is the scaling parameter and P_{DMD} describes the micromirror size. The resulting Δ expresses by how many pixels the camera image can be moved, while still preserving the influence of the proper DMD pixel. For the test setup, the camera pixels have a size of $P_{cam} = 5.5\,\mu\text{m}$, the number of indistinguishable DMD pixels is $d_{DMD} = 1$, the DMD pixels have a size of $P_{DMD} = 7.6\,\mu\text{m}$, and from the calibration file, a scaling factor of $s = 2.9$ can be extracted. This yields a sensitivity of $\Delta = 2.1\,\text{px}$. This criterion is now tested by artificially shifting the camera image by a known number of pixels in the x- and y-direction. With the current calibration, an artificial shift of $\Delta_x = [-1.8,\ 2.2]$ and $\Delta_y = [-0.9,\ 2.9]$ does not produce "Dunes". Those intervals agree well with our estimate, however, it seems that the y-direction is more sensitive to "Dunes" than the x-direction. In the case of perfect calibration, the interval Δ should be symmetric. Hence, the "Dunes" can be used to further optimize the alignment. Here, an offset of $\Delta_x = 0.2\,\text{px}$ and $\Delta_y = 1.9\,\text{px}$ provides a symmetric interval. However, in our system, "Dunes" are the smallest observable features caused by translation misalignment, such that an even better calibration does not provide any visible improvement. So, if no "Dunes" arise during the optimization, the translation alignment is sufficient. By applying a Gauss filter to the camera images, lower resolutions with higher d_{DMD} can be simulated. For a Gauss blur with $\sigma = 5$, $d_{DMD} = 2$, and for $\sigma = 10$, $d_{DMD} = 5$. For those conservative estimates of d_{DMD}, eq. 4.7 holds.

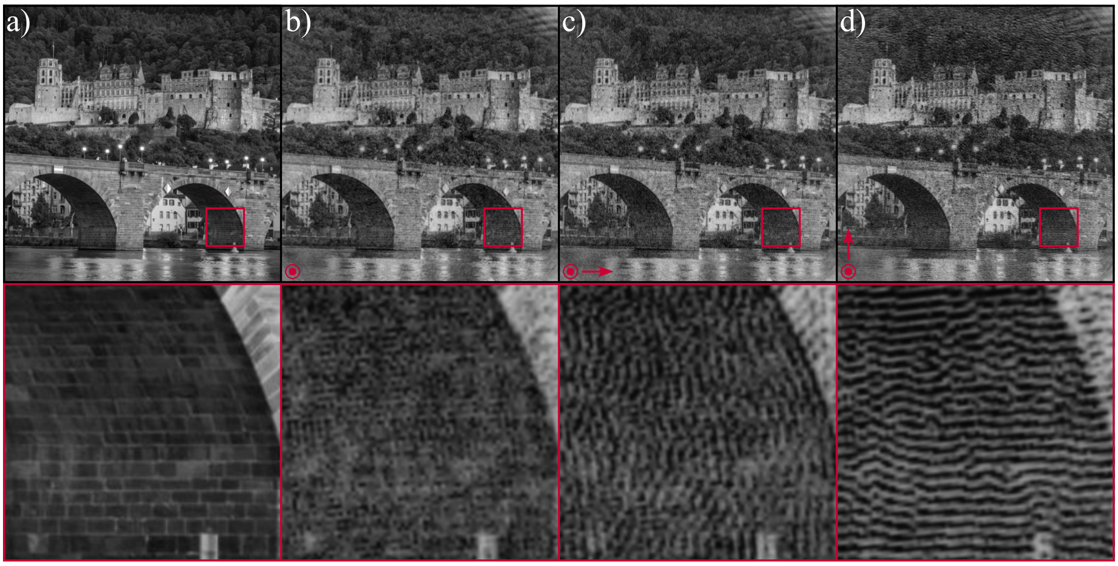

Figure 4.9: (a) An 8-bit reference image of the Heidelberg Castle and (b) the corresponding camera image after 30 iterations. An artificial, translational shift of 3.5 pixels in (c) x-direction, as well as (d) y-direction, was introduced prior to the 30 iterations of the optimization algorithm. Due to the translational shift in (c,d), "dunes" can be observed throughout the image. The "dunes" appear as vertical ripples in (c), while they are horizontally orientated in (d). Below an enlarged visualization of the section outlined by the red square is shown.

4.1.4 Methods

The light-based feedback algorithm is written in *Python*. Before starting the algorithm, the specifications of the used devices, as well as some other parameters have to be set. Additionally, a working directory has to be selected, where the camera images, debugging plots, and optimized DMD patterns are saved.

To communicate with the DMD, the *ALP4lib* module[4] that is based on the *ViALUX* API is used. This module is better maintained for *Python* compared to its *MATLAB* counterpart. In the test setup, a *DLP9000X* chip with a *V4390* controller board was used. According to tab. 3.1, the maximum size of a DMD pattern amounts to 2560 px × 1600 px. Often, the DMD patterns are rotationally symmetric, and therefore, a size of 1600 px × 1600 px is sufficient.

The images were taken by a *Mako G-223 NIR* camera that can be also controlled via a *Python* API[5]. It has a resolution of 2048 px × 1088 px. However, all cameras that use the Vimba module are directly compatible and every other camera can be easily implemented by replacing the function *"CAM_image"* in *"take_image.py"*.

---

[4] github.com/wavefrontshaping/ALP4lib

[5] github.com/alliedvision/VimbaPython

The camera is initialized by loading all settings from a configuration file. Here, the most critical parameters are the exposure time and gain.

As briefly mentioned in the discussion of the image normalization process, a midway equalization algorithm[6] was tested but removed in the final version of the optimization algorithm. It equalizes the grayscale histograms of images while attempting to preserve their previous dynamics. More information about the midway image equalization can be found in [29]. However, the algorithm tended to darken the camera image until no details were left. Furthermore, it generated artifacts on the homogeneous background of the reference image. Probably, the equalization of a noisy camera image histogram and an optimal reference histogram with sharp grayscale features is difficult.

4.2 Density-Based Feedback Algorithm

As presented in the previous section, the light-based feedback algorithm can optimize arbitrary light potentials in a reasonably short time. The average of the error map can be reduced by a factor of 5 and its standard deviation by a factor of 3. In the BECK experiment, the light potential on the atom plane is mainly affected by interference effects stemming from reflections on the uncoated science chamber. However, the light-based feedback algorithm would correct the projected beam shape either before entering or after exiting the science chamber, but never at the position of the atoms. Moreover, the figure of merit in the experiment is still the imaged atomic density distribution. Therefore, the previously presented algorithm was adapted to work with the experimental control setup to directly optimize the atomic density distribution. Details of the experiment and the current single-DMD setup that will be used in the following, are discussed in sec. 2.4. Similar to the previous section, the realization of each step in fig. 4.1 is discussed for this particular case. Again, the initialization of the algorithm is described, followed by the optimization process. Then, the results and some observations are discussed and finally, the methods are described.

4.2.1 Initialization

Similar to the previous section, the latest calibration parameters are either loaded from a file or have to be determined in a calibration routine.

---

[6] github.com/alinasode/general-midway-equalization

Calibration According to eq. 4.1, a translation, a rotation, and a scaling factor have to be found. Since the FFT-based image registration algorithm did not work reliably, another transformation scheme was used. Again, three points that form a scalene triangle in a prescribed trapping potential are used as a calibration pattern. In fig. 4.10a, this calibration pattern in a circular, linearly slanted wall potential is depicted. Again, these are the minimal number of points needed for a unique transformation and any other number of points on a convex hull with no rotational symmetry will work. The trapping sequence and the calibration pattern are loaded onto the DMD and a BEC experiment is conducted. Based on the mean camera image of several realizations, the atomic density distribution is calculated. A more detailed description of the experimental block can be found in the next section. The light, reflected by the three points in the calibration image, called hole punchers, pierces the condensate, as shown in fig. 4.10b. The calibration starts by roughly centering and scaling the atomic density images to increase the size of the atomic cloud without clipping. Therefore, the center of mass (CoM) of the condensate is calculated and shifted to the center of the image to prevent the atom cloud from clipping in the following scaling procedure. Here, the camera image is scaled according to eq. 4.2 by a factor of 5.2 as a first initial guess. The result is displayed in fig. 4.10c with the old and new position of the CoM marked by a star. On the rescaled atomic density image, the holes are first identified with a peak find algorithm[7] and then fitted with a 2D-Gaussian, from which the peak positions are extracted. Figure 4.10d shows the peak positions of the peak finder algorithm, as well as the Gauss-fitted positions. The peak positions, as well as the hole puncher positions on the DMD pattern, form the same geometric shape depicted in fig. 4.10e and can be transformed into each other by affine transformations. The scaling parameter s is determined by comparing the perimeters of the objects. Then, the CoM of both objects is calculated and compared to obtain the translation vector (t_x, t_y). To extract the rotation angle, the extracted hole center positions have to be paired with the prescribed point positions by comparing the total edge length to their neighbors. The two points with the longest total edge length and their respective CoM are then used to define two vectors, where the dot product is used to obtain the angle of rotation θ. The parameters are then combined with the parameters of the rough prealignment and are saved in a file. These values can be used until the position of the condensate is changed. Now, the camera image can be mapped onto the DMD images, as displayed in fig. 4.10f. Without

---

[7] mathworks.com/matlabcentral/fileexchange/113225-peaks2-find-peaks-in-2d-data-without-additional-toolbox

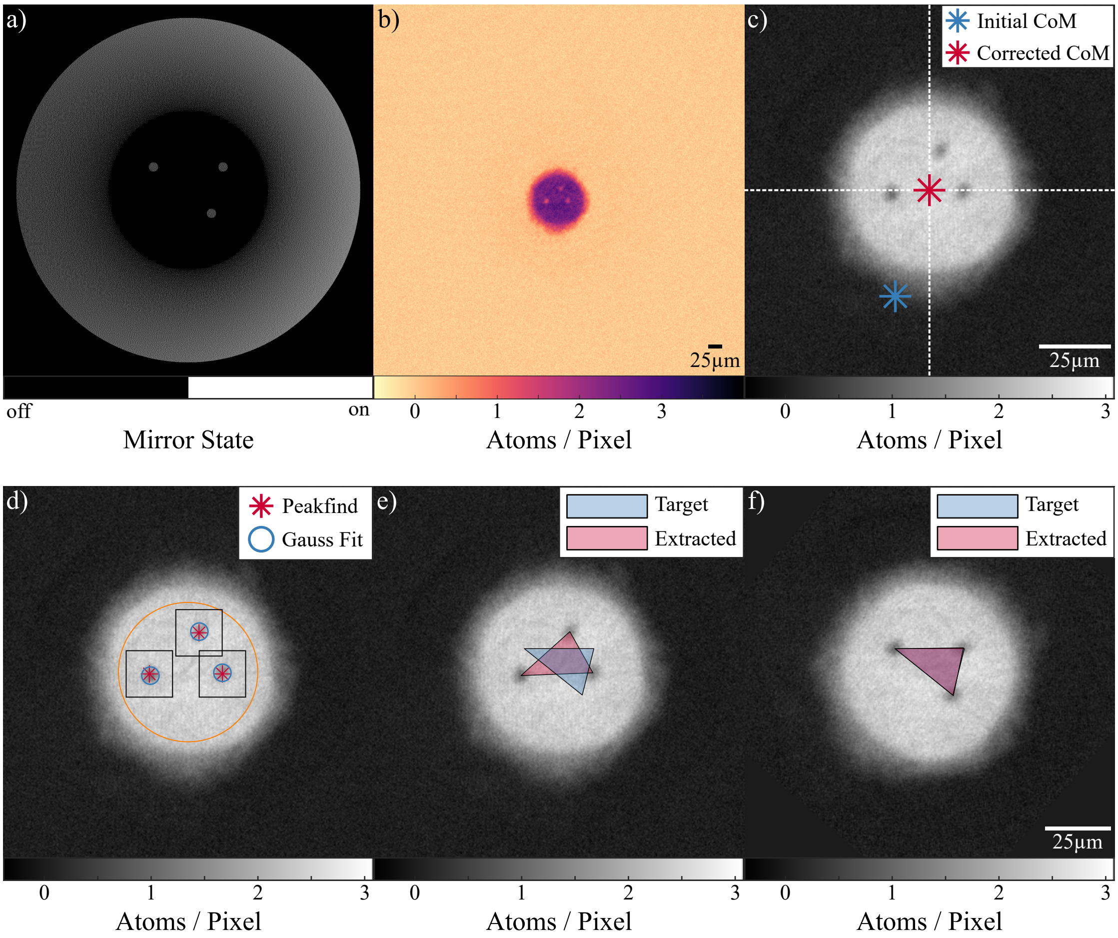

Figure 4.10: (a) Calibration pattern loaded onto the DMD. It consists of a slanted wall trapping potential with three hole punchers. (b) The corresponding camera image is an average of five realizations. (c) This image is then translated and scaled based on the CoM and optical properties of the DMD setup. (d) In the enlarged condensate image, the holes are first roughly identified by using a peakfind algorithm inside the orange circle with a size of $\frac{2}{3}$ of the condensate diameter. Based on these peak positions, 2D Gaussians are fitted to the holes in the black boxes. (e) The peak positions of the Gaussian fits are then compared to the reference hole puncher positions. (e) The triangle based on the extracted hole positions is mapped onto the reference triangle, which provides the necessary transformation parameters for the camera image. Note that (a) and (e) have a size of 1600 px × 1600 px, while the size of (b) - (e) amounts to 1024 px × 1024 px. For better visibility, (c) - (f) use a gray colormap but show the same atomic cloud as (b).

the experimental block, the new calibration scheme takes approx. 6 s. This is a factor of three faster compared to the image registration algorithm used in the light-based algorithm. However, in the experimental block, a BEC experiment has to be conducted several times, which itself takes significantly longer than the total calibration process in the light-based case.

Next, the reference image has to be selected. The imaging routine provides an atomic density distribution, while the DMD pattern represents the light potential.

Hence, either a reference distribution or a reference potential can be selected. Since the atom number fluctuates in the experiment, the reference has to be scaled accordingly. For the reference potential, the corresponding density distribution has to be calculated according to eq. 2.13, where the chemical potential μ depends on the atom number. This is an essential step since not only the density but also the size of the condensate depends on it. On the other hand, the reference distribution is scaled with a global factor β to match the atom number. Note that the size of the given reference density distribution should not depend on the atom number as it remains constant under the scaling. Only the atomic density is affected by β. Optionally, a mask can be selected to exclude areas from the optimization process. The mask works exactly as described in the previous section. Exemplary masks can be seen in fig. 4.11c and f.

To evaluate the algorithm, an example for each reference type was chosen and optimized. As reference potential, a harmonic potential as described in eq. 2.10 with an angular frequency of $\omega = 10\,\mathrm{Hz}$ was selected and is depicted in fig. 4.11a. The atomic cloud in this trap has to follow the Thomas-Fermi profile described in eq. 2.14, such that the shape of the condensate depends on the atom number and scattering length. While the dependency on the atomic number is important to test the normalization process of the algorithm, the scattering length dependency can be used to evaluate the quality of the optimized potential.

For the reference density distribution, the Friedmann-Lemaître-Robertson-Walker (FLRW) metric with spherical curvature was chosen, which was already realized in [54]. Here, the density profile has to follow

$$n_{2D}(r) = n_0\,(1 + \frac{r^2}{R^2})^2, \tag{4.8}$$

where n_0 is the density at the center of the trap, and R describes the size of the condensate. While the size of the condensate is fixed by R, fluctuations in atom number can be compensated by adjusting n_0 with the global factor β. At the same time, the required density ratio of 1:4 between the center and edge of condensate is maintained. The density profile is shown in fig. 4.11d. To maintain the condensate's radius R, a circular hardwall potential with a depth of approx. 2μ is used for the confinement, depicted in fig. 4.11e. Besides the evaluation of the shape, the propagation of a phonon wave packet will allow us to assess the optimized atomic distribution.

Now, the initial DMD sequence has to be prepared. It consists of a trapping

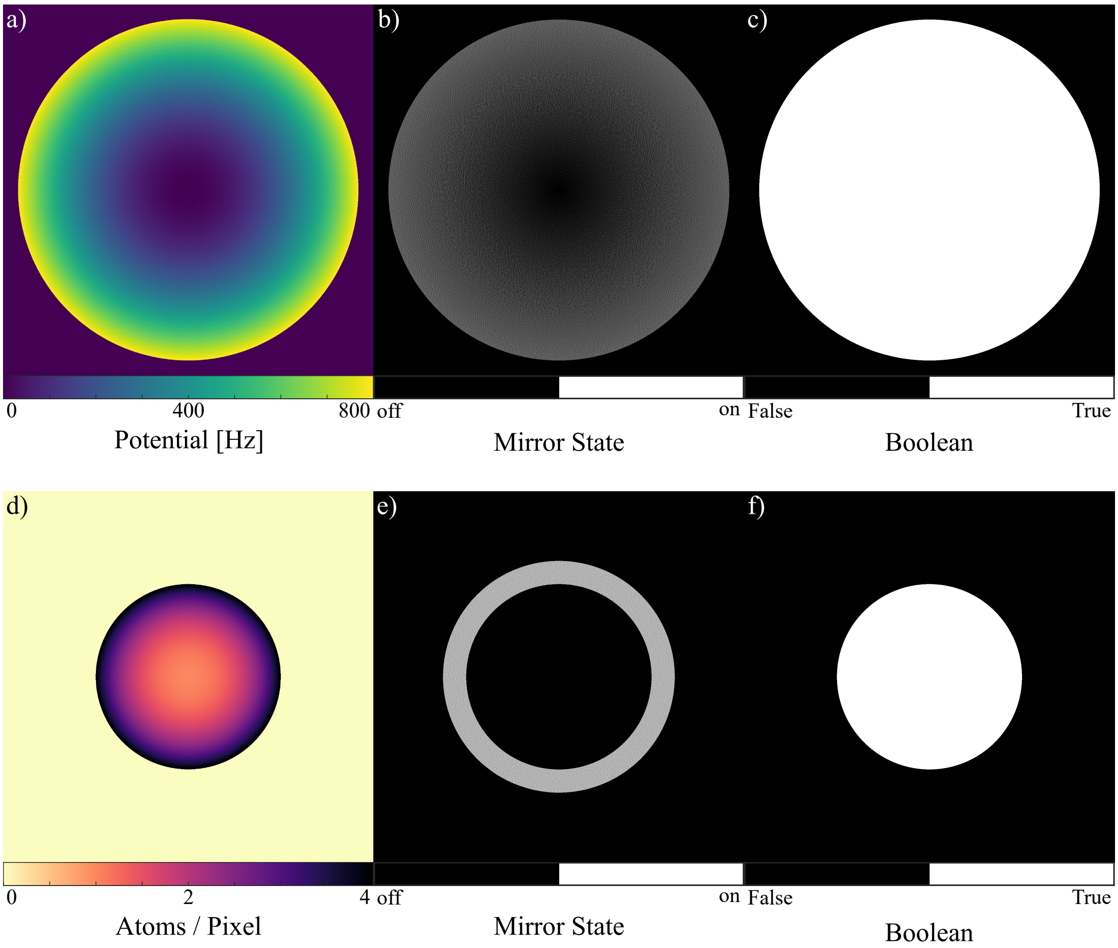

Figure 4.11: (a) A harmonic reference potential according to eq. 2.10 with $\omega = 10\,\mathrm{Hz}$ and $m = 39\,\mathrm{u}$. (b) The potential is used to calculate the initial DMD pattern. (c) An optional mask with a similar size. The reference atomic image (not shown) is recalculated after each iteration based on the atomic number in the experimental realization. (d) Below a reference density distribution following eq. 4.8 with $n_0 = 1\,\mathrm{atom/px}$ and $R = 35\,\mathrm{\mu m}$. (e) The initial DMD image consists of a hard wall potential with radius R. (f) Optional mask with the same radius. After each iteration, the density distribution is scaled with a global factor β based on the atom number in the experimental realization. This figure is a vector graphic that resolves every pixel of the 1-bit DMD patterns.

sequence, followed by a ramp-up of the desired light potential. More technical details can be found in the next section. For the reference atomic distribution, the initial DMD pattern consists of a hard wall potential with a prescribed radius R. This is displayed in fig. 4.11e. The resulting, homogeneous atom distribution is a sufficient initial guess, from where the algorithm can quickly converge. On the other hand, the reference potential has to be transformed into an initial DMD pattern to start with a relatable trap geometry. Therefore, the fraction of turned-on micromirrors, which is needed to achieve the prescribed light potential, has to be calibrated.

Initial DMD pattern According to [30], the reference potential $V_L(x, y)$ is connected to the micromirror fraction by

$$V_L(x, y) = c_L \cdot P_{DMD} \cdot I_{rel}(x, y). \tag{4.9}$$

Here, P_{DMD} is the DMD illumination power, and the reflected intensity fraction $I_{rel}(x, y)$ is the square root of the fraction of turned-on mirrors in a small, unresolvable area around (x,y). The calibration constant c_L is dependent on the experimental configuration and has to be determined once. For this, the condensate is loaded into a circular trapping potential $V_L(x, y)$ with linearly slanted walls, where the slope and the laser power P_{DMD} are known. The DMD pattern used for this measurement is shown in fig. 4.12a. Then, the slope of the light potential in fig. 4.12b is compared to that of the condensate edge in fig. 4.12c. Transposing eq. 4.9 and using the Thomas-Fermi approximation to express the potential in terms of an atomic density (Eq. 2.13), the calibration constant is given by

$$\frac{c_L}{h} = \frac{[n(r) - n(r')] \cdot g_{2D}}{[I_{rel}(r) - I_{rel}(r')] \cdot P_{DMD} \cdot h} \tag{4.10}$$

Since the radial average is used to determine the slope, the Cartesian coordinates (x, y) can be replaced by the radial coordinate r. For the realization in fig. 4.12c, a DMD power of $P_{DMD} = 0.1\,\mathrm{W}$ and a scattering length of $a_s = 100\,a_0$ was set[8], yielding $g_{2D} = 1.1 \times 10^{-44}\,\mathrm{J\,m^2}$. Since the slope of the potential and condensate edge are approximately linear, the positions of the corresponding readout points do not have to coincide. Nonetheless, the different distances $|r - r'|$ between the readout points have to be considered in the calculation resulting in

$$n(r) - n(r') = \frac{(2.53 - 0.53)\ \mathrm{px}^{-1}}{(400 - 320)\ \mathrm{px} \cdot A_{px}} = 1.2 \times 10^{11}\,\mathrm{m}^{-2}\,\mathrm{px}^{-1} \tag{4.11}$$

$$I_{rel}(r) - I_{rel}(r') = \frac{0.16 - 0}{(650 - 250)\ \mathrm{px}} = 4 \times 10^{-4}\,\mathrm{px}^{-1}. \tag{4.12}$$

To match the unit of the atom density distribution n with the interaction parameter g_{2D}, the pixel area of n has to be given in square meters amounting to

$$A_{px} = \left(\frac{P_{cam}}{M_{cam}}\right)^2 = 2.07 \times 10^{-13}\,\mathrm{m}^2\,\mathrm{px}^{-1}. \tag{4.13}$$

---

[8] Given that 1 V in the experimental control corresponds to 0.1 W laser power

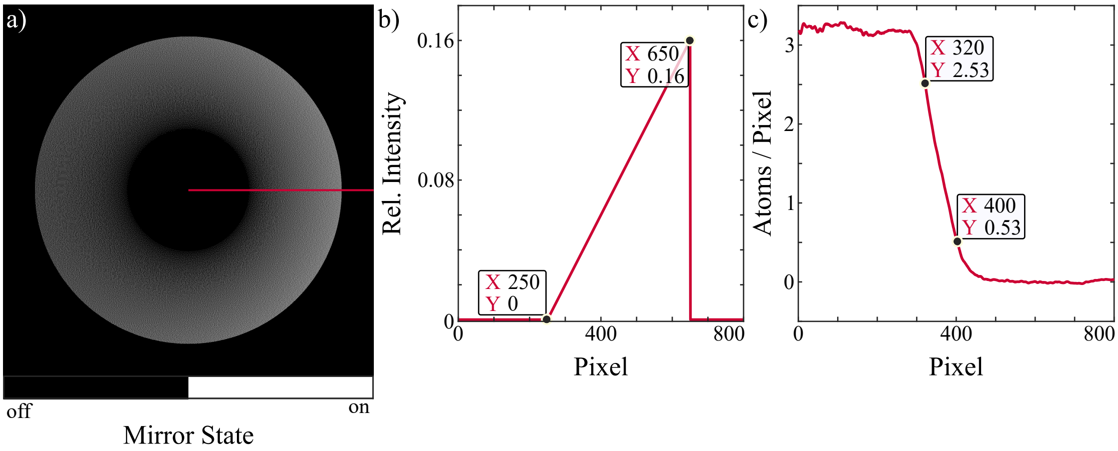

Figure 4.12: (a) The DMD calibration pattern consists of a slated wall potential with a linear slope. The red line indicates a single pixel cut through the rotational symmetric DMD pattern, which is sketched in (b). Note that the relative intensity $I_{rel}(r)$ is the square root of the fraction of turned-on mirrors shown in (a). (c) With the radial average of an experimental realization, the slope of the condensate edge is determined. (b) and (c) are both in units of DMD pixels.

Now, inserting all values in eq. 4.10 yields a calibration factor of

$$c_L = 50\,\mathrm{kHz\,W^{-1}}. \tag{4.14}$$

Due to the Gaussian shape of the illumination beam, the light intensity decreases radially. Hence, the calculated calibration constant is only a lower bound and should have a radial dependency. However, the constant is only used to calculate an initial DMD pattern that will then be optimized. As demonstrated in the previous section, the algorithm compensates the Gaussian intensity distribution and therefore, it is sufficient to use a global calibration constant. To crosscheck the calibration constant with theory, the required laser power for a dipole potential of $V_{dip} = 50\,\mathrm{kHz}$ is calculated similar to sec. 3.1. For $\lambda = 532\,\mathrm{nm}$, $\omega_0 = 768.5\,\mathrm{nm}$ and $\Gamma = 2\pi\cdot\, 6\,\mathrm{MHz}$, eq. 2.50 yields an intensity of $I(r) = 0.033\,\mathrm{mW\,\mu m^{-2}}$. Using the same $\frac{1}{e^2}$ beam radius of $70\,\mathrm{\mu m}$ and typical condensate radius of $35\,\mathrm{\mu m}$, a power of $1\,\mathrm{W}$ is required, which approves the experimentally determined calibration constant for the already implemented DMD. Now that an initial DMD pattern can be calculated from any reference potential, the optimization process can start.

4.2.2 Iteration

As described in the last section, an iteration of the optimization routine consists of three parts. These steps are illustrated in fig. 4.1 and are discussed in the following.

Experimental Block The experiment starts by loading the latest trapping sequence onto the DMD. The sequence consists of two parts: Confining the atoms and preparing them in an initially prescribed trapping geometry. Then, the initial trap is ramped to the desired DMD pattern that will be optimized by determining the different mirror flip states and randomly correcting these states in a preset number of steps. Now that the DMD is prepared, a BEC experiment is conducted as described in sec. 2.4. An experimental realization takes approx. 25 s in the BECK experiment. For the optimization, an average of five runs is used to reduce the effect of experimental noise, for example, atomic shot noise, which is much larger than the noise in the light-based optimization. The camera automatically takes an absorption, a reference, and a background image. With those three pictures, the atomic density distribution is calculated according to [44]. To eliminate imaging errors, the atom numbers of each run are compared and images, where the atom number does not lie within two sigma, are neglected. Then, the mean image is created that is used for the optimization process. Loading the imaging data and calculating the density distribution takes approx. 12 s. However, the duration strongly depends on the connection to and current load of the file server. In total, the experimental block takes 140 s to create a mean image of five runs.

Mapping and image normalization The camera image can be mapped directly onto the DMD image by applying the transformation parameters. If a reference potential is provided, the potential is filled according to eq. 2.13 based on the atom number of the camera image. Hence, a minimization algorithm searches the corresponding chemical potential μ of the condensate. This step is not needed if a reference density distribution is provided instead. In both cases, the 95th percentile of the reference and camera atomic density are compared and the fraction of those values β is calculated. β is then multiplied with the reference distribution to normalize the range of both images. If the reference distribution was calculated from a potential, this operation slightly deforms the shape of the reference condensate. However, the range of the calculated density distribution usually agrees well with the camera image and normally, $\beta \geq 0.95$. For the provided reference density distribution, the global factor β is needed to match the atom number of the camera image as previously discussed. Here, β does not change the functional form of the density profile and therefore, does not deform the reference. The transformed camera image can now be optimized based on the normalized reference image. The mapping and normalization process takes approx. 1.5 s.

Optimization By subtracting the reference image $\hat{p}_R(x,y)$ from the transformed camera image $p_{cam}(x,y)$ and dividing by the range of $\hat{p}_R(x,y)$, the local error is calculated according to

$$\epsilon(x,y) = \frac{p_{cam}(x,y) - \hat{p}_R(x,y)}{max[\hat{p}_R(x,y)] - min[\hat{p}_R(x,y)]}. \tag{4.15}$$

The interpretation of the error map and the mirror flip probability $\alpha|\epsilon(x,y)|$, as well as the optimization routine were already described in the previous section. Due to the higher experimental noise, two Gauss filters are applied, representing fundamental length scales. Based on the estimated chemical potential μ, the healing length ξ described in eq. 2.9 is determined to filter all frequencies higher than $\frac{1}{\xi}$. Additionally, a Gauss filter with a σ of the number of unresolved DMD pixels is used. Moreover, an additional flip condition was implemented that restricts the optimization routine to areas where the reference potential is larger than zero. Furthermore, the alpha value has to be tuned depending on the illumination laser power P_{DMD} and the calibration constant c_L. In the current experiment with c_L $= 50\,\mathrm{kHz\,W^{-1}}$ and $P_{DMD} = 0.1\,\mathrm{W}^8$, an $\alpha = 0.3$ grants fast convergence, while preventing an overcompensation of the error. The optimization process takes approx. 8.3 s.

The optimized pattern is then saved and loaded into the DMD pattern folder to prepare the next iteration. To conclude, the calibration and each optimization iteration take approx. 150 s, where the main contribution stems from the BEC experiment.

4.2.3 Results and Observations

The previously described density-based feedback algorithm has been used to optimize two common problems: The harmonic oscillator and the positively curved FLRW metric. These examples cover the two reference types and are used to evaluate the optimized pattern. Additionally, another frequently used light potential, the grid potential, will be presented and the performed optimization will be assessed. Finally, the relevance of the "Dune" phenomenon in the main experiment is discussed.

Harmonic Oscillator Similar to the light-based algorithm, the number of flipped mirrors, as well as the average error and standard deviation of the error map are logged in each iteration. Figure 4.13 displays these values for the harmonic potential (Fig. 4.11a) over seven iterations. Here, a scattering length of $a_s = 200\,a_0$ and

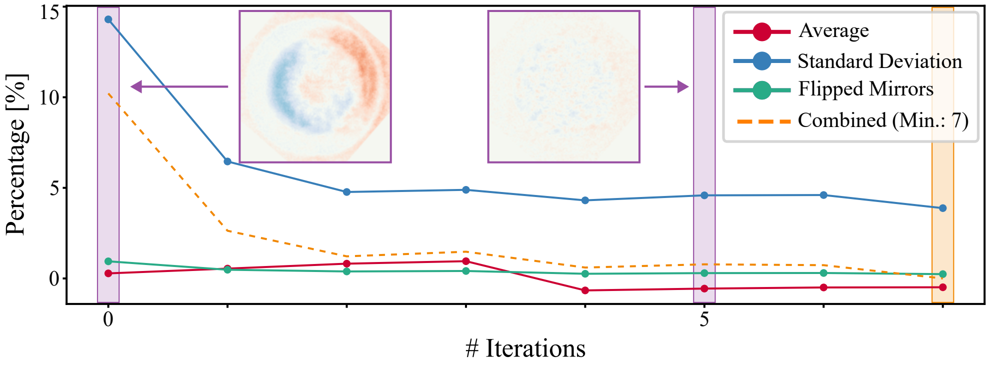

Figure 4.13: Average error and standard deviation of the error map, as well as the fraction of flipped mirrors for the harmonic potential (Fig. 4.11a) over 7 iterations. The sum of the average and standard deviation subtracted by their means provides the combined graph. The iteration with the lowest combined value is marked in orange. The insets (violet) display the error map of the marked iteration.

$\alpha = 0.3$ were used. The algorithm converges after four iterations and reaches an average of -0.006 with a standard deviation of 0.043, while the number of flipped mirrors stays at 7000. The global minimum is reached at the last measurement point, however, the improvement seems to be marginal compared to the first four iterations. On average, the atom distribution deviates by 0.6 % from the reference with a one sigma deviation of 4.3 %. Since each iteration of the density-based algorithm takes significantly longer compared to the light-based optimization routine, the long-term convergence behavior of the algorithm was not studied.

In fig. 4.14, the initial state and fourth iteration are presented in more detail. The error map of the initial state has an average of 0.003 with a standard deviation of 0.14. In the first iteration, approx. 24 000 mirrors were flipped. The values of the fourth iteration were already presented in the previous paragraph. While the average value stays at approx. zero, the standard deviation could be reduced by a factor of 3. The error map of the optimized DMD pattern in fig. 4.14g does not show any pattern, however, the density fluctuations form larger clusters in the areas of lower overall densities. In each iteration, the target density distribution is calculated based on the atom number of the camera image. The radial average of the targeted density distribution is compared to the imaged distribution in fig. 4.14d and h. Not only the shape of the profile but also the standard deviation of the optimized atom cloud have been improved compared to the initial guess.

The capability of the density-based algorithm to optimize a condensate of constant size has been demonstrated. However, it remains to be tested if the optimized DMD pattern can be also used for different cloud sizes or rather scattering

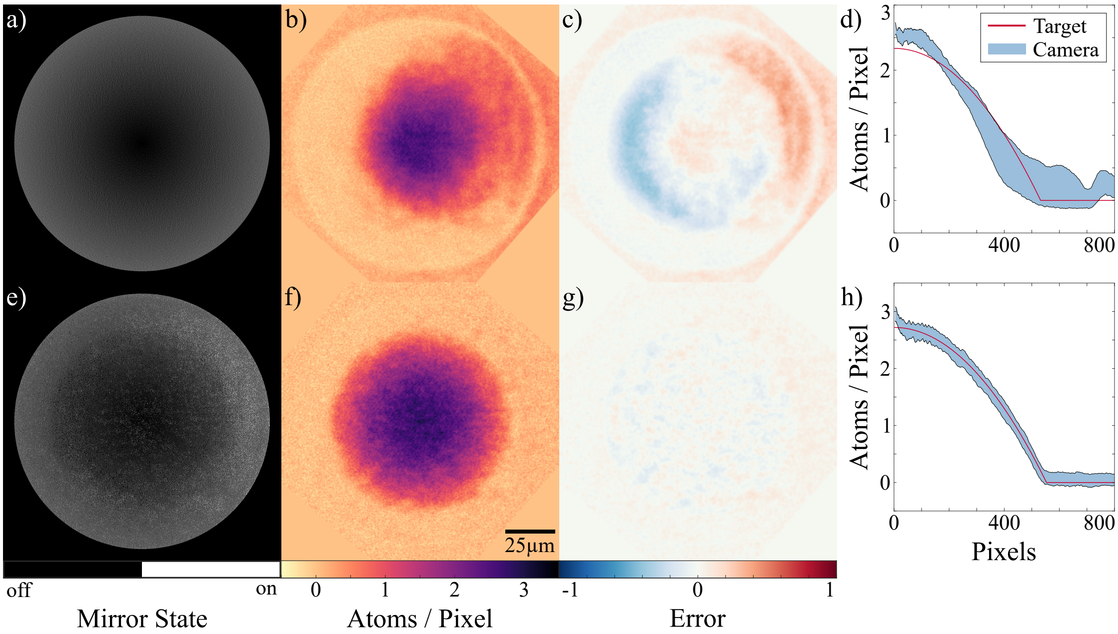

Figure 4.14: Comparison of the (a) initial DMD and (b) camera image of a harmonic trap (Fig. 4.11a) with an (e) optimized DMD and (f) camera image after four iterations. The corresponding error maps of the initial and optimized camera image are shown in (c) and (g), respectively. The radial averages of each camera image are displayed in (d,h) and are compared to the targeted condensate shape. The blue area represents the one-sigma range.

lengths. In a harmonic potential, the condensate should follow the Thomas-Fermi (TF) profile described in eq. 2.14. Consequently, the radius of the atomic cloud should show a square root dependency on the scattering length. This was tested by changing the scattering length of the condensate in the optimized DMD pattern via Feshbach resonances. The resulting atomic density distributions and the fitted TF profiles to the radial average are presented in fig. 4.15a-e. The chemical potential μ extracted from the camera images agrees with the fitted value but was in general overestimated. The fitted radii show the theoretically expected square root dependency, when plotted against the scattering length depicted in fig. 4.15f. The potential was optimized for a scattering length of $a_s = 200\,a_0$ but all experimental realizations follow the Thomas-Fermi profile and have a round shape. The realization with $a_s = 50\,a_0$ deviates the most from the targeted shape. Probably, the optimization algorithm was focused on the edge of the potential and not on its center, as these are the most critical areas for a larger condensate. However, the condensate with $a_s = 50\,a_0$ is situated in the center of the trap.

While the expected Thomas-Fermi profile is maintained, when scaling the cloud size, the behavior of dynamical processes, like the breathing modes of the condensate, remains to be tested. To induce a breathing of the condensate, the scattering

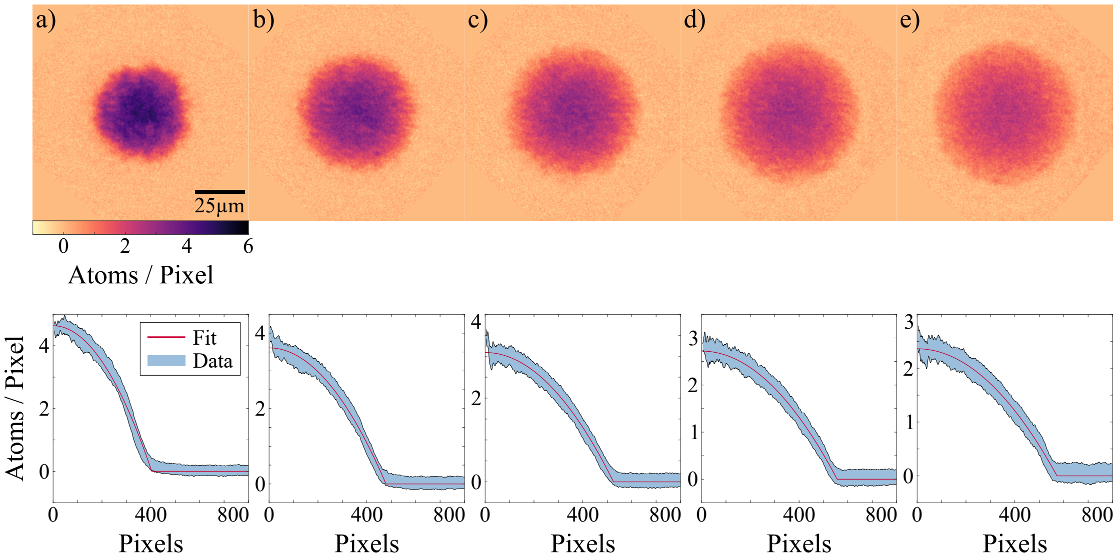

Fit:

$$\psi_0\left(r\right) = \sqrt{\frac{\mu}{g}\left(1 - \frac{r^2}{R_{TF}^2}\right)}\,\theta\left(R_{TF} - r\right)$$

Coefficients	a)	b)	c)
μ	185.2(6) Hz	288.4(8) Hz	370.2(10) Hz
R_{TF}	403.8(10) px	478.4(11) px	525.5(11) px

	d)	e)
μ	434.7(10) Hz	471.7(12) Hz
R_{TF}	556.6(11) px	573.0(12) px

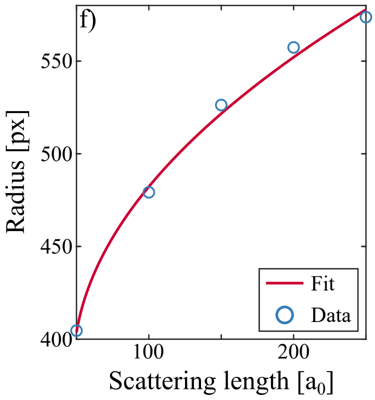

Figure 4.15: Condensate in the optimized harmonic trap (Fig. 4.14e) with different scattering lengths a_s. The scattering length starts at (a) $50\,a_0$ and increases to (e) $250\,a_0$ in steps of $50\,a_0$. Below, the Thomas-Fermi profile was fitted to the corresponding radial average of the camera images. The interaction strength parameter g_{2D} was calculated according to eq. 2.20 such that only μ and R_{TF} were left as fit parameters. The blue area represents the one-sigma range. The fit function and resulting coefficients with one sigma error are listed in the box below. (f) The resulting Thomas-Fermi radius R_{TF} is plotted against the scattering length a_s and a square root function $r(a_s) = A \cdot \sqrt{a_s - B} + C$ was fitted to the data.

length was ramped down after loading the atoms into the optimized harmonic trap. Then, the radii after different evolution times are determined and were compared to the theoretical oscillation frequency of 2ω. Ideally, the radius of the condensate should follow a damped sinusoid given by

$$r(t) = R \cdot \exp(-\lambda t) \cdot \cos(\omega_{osc} t - \varphi) + c. \tag{4.16}$$

Here, R is the radius of the condensate at $t = 0$, λ is the decay rate, ω_{osc} describes the angular frequency, φ is the phase angle at $t = 0$ and c is a global offset. In

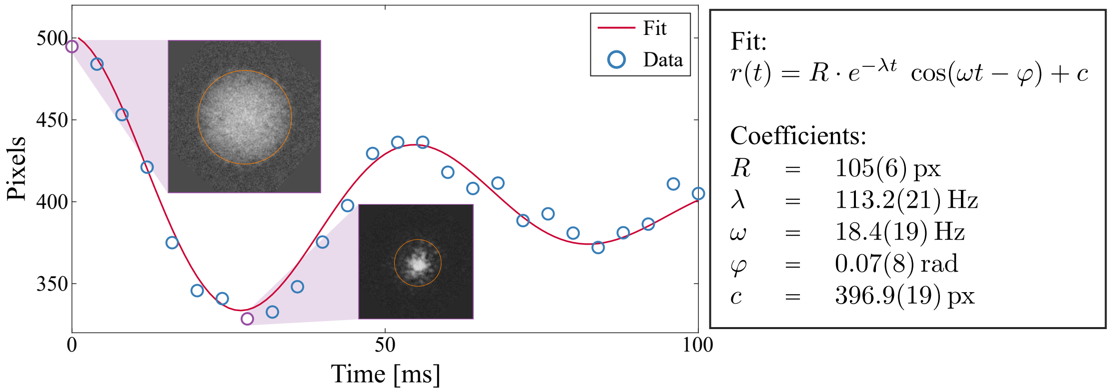

Fit:
$r(t) = R \cdot e^{-\lambda t}\ \cos(\omega t - \varphi) + c$

Coefficients:

R	=	105(6) px
λ	=	113.2(21) Hz
ω	=	18.4(19) Hz
φ	=	0.07(8) rad
c	=	396.9(19) px

Figure 4.16: Breathing mode of the condensate in the optimized harmonic trap (Fig. 4.14e). To induce the mode, the scattering length was ramped down from $200\,a_0$ to $5\,a_0$ after loading the trap. The fit function and resulting coefficients with one sigma error are presented in the box on the right. The insets (violet) display the condensate after different hold times. The circle (orange) indicates the estimated diameter of the atom cloud.

fig. 4.16, eq. 4.16 is fitted to the experimental data to extract the frequency. The fit yields a frequency of $\omega_{osc} = 18.4(19)$ Hz, which translates to a harmonic trap frequency of $\omega = 9.2(10)$ Hz. This agrees in the one sigma range with the prescribed trap frequency. In conclusion, the optimized harmonic potential behaves as expected and can also be used for different condensate sizes.

For similar α, other DMD patterns follow the convergence behavior depicted in fig. 4.13. Seven iterations seem to be sufficient to obtain a good result. The whole process to optimize a DMD pattern will then take 20 min. Note that 19 min are needed to conduct the BEC experiment, while the optimization algorithm itself takes 1 min.

Spherical metric To further validate the optimization algorithm, the reference density distribution (Fig. 4.11d) following eq. 4.8 was optimized. In this case, five iterations were needed to converge, which is within the expected seven iterations. Here, an extra iteration is needed to compensate for the bad initial guess of a flat condensate with radius R. Accordingly, the optimized DMD pattern is not compared to the initial guess but instead, it is compared to a reference potential. The reference potential has to be tweaked manually according to the atom number to reach the density ratio of 1:4. Figure 4.17 illustrates both cases in the already used manner. The error map of the guessed, initial potential has an average of -0.03 with a standard deviation of 0.17 and 8500 mirrors have to be flipped. In comparison, the error map of the optimized pattern has an average of 0.01 with a standard deviation of 0.16, while 8000 mirrors need to be flipped. Although, these

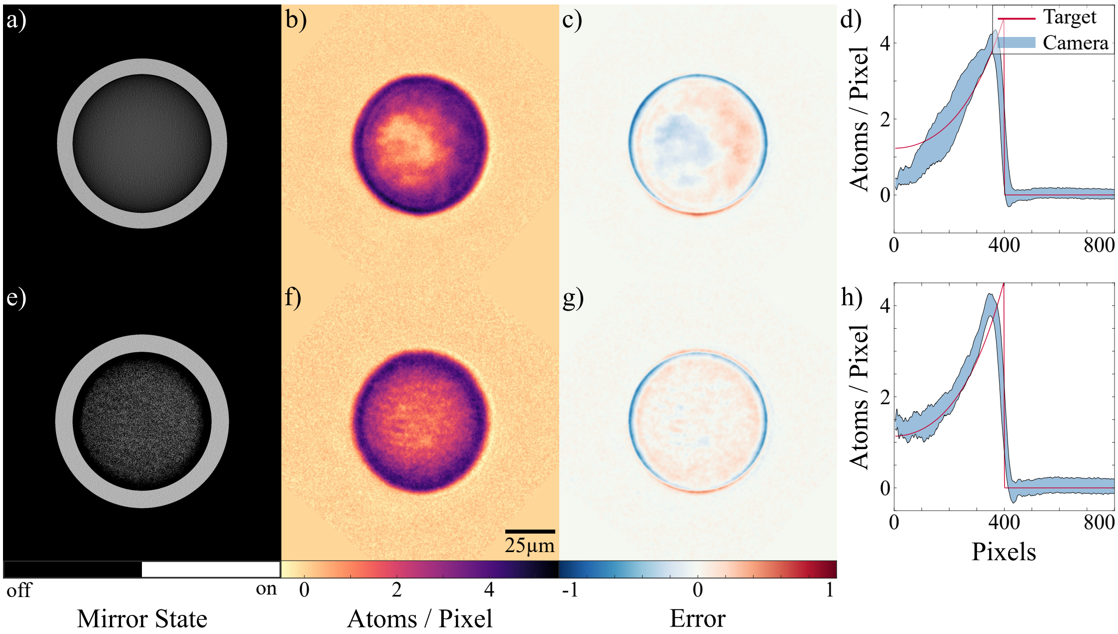

Figure 4.17: Comparison of the (a) initial DMD and (b) camera image implementing an spherically curved FLRW metric (Fig. 4.11d) based on a tuned reference potential with an (e) optimized DMD and (f) camera image based on a reference density distribution after five iterations. Note that the initial DMD image of the reference density distribution only consists of a hard wall potential, and therefore, a manually tweaked initial guess was used for the comparison. The initial guess was tweaked according to the atom number to reach the density ratio of 1:4. The corresponding error maps of the initial and optimized camera images are shown in (c) and (g), respectively. The radial averages of each camera image are displayed in (d,h) and are compared to the targeted condensate shape. The blue area represents the one-sigma range.

values do not indicate any improvement, the radial averages of the two condensates show a clear improvement in the case of the optimized DMD pattern. Since the shape of the optimized condensate is closer to the target, the required density ratio of 1:4 has been achieved, which is not the case for the guessed, initial potential. In both cases, the sharp edge of the condensate contributes most to the overall error. The sharpness of this feature is limited by the resolution of the objective, as well as the healing length of the condensate. Here, the resolution and healing length have a similar length scale of 10 px on the DMD chip. By evaluating the error map without the edges, the standard deviation of the initial guess reduces to 0.04, while the optimized condensate reaches a value of 0.016. Now, the error map shows an improvement of factor three similar to the harmonic potential. On the other hand, the averages do not change by a lot. This case demonstrates that although the error map is a useful indicator for the quality of the optimization, it has to be used carefully. In some cases, the region of interest has to be adapted manually. However, a combination of condensate image, error map, and radial

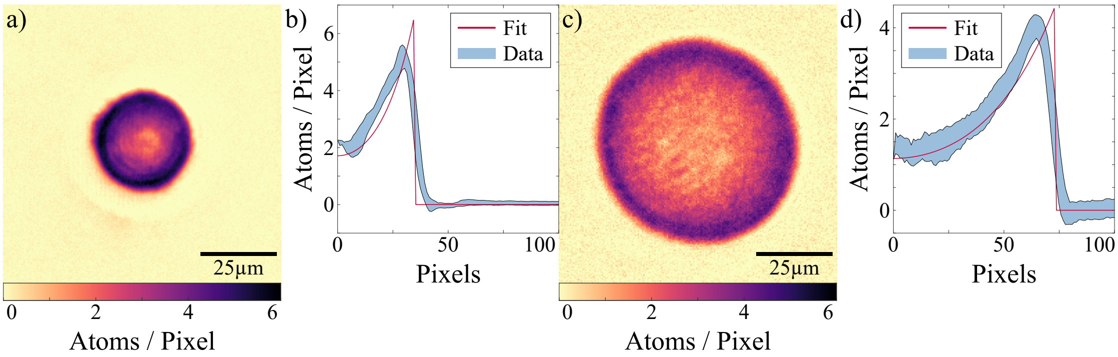

Figure 4.18: (a,b) Comparison of the condensate used in [54] with (c,d) the optimized density distribution shown in fig. 4.17e-h. (a) and (c) show the centered atom density distribution cropped to 200 px × 200 px with no pixel binning. (a) is averaged over 100 realizations, while (c) uses 15 realizations. In (b) and (d), eq. 4.8 was fitted to the radial average of the corresponding condensate image. (b) has a center density of $n_0 = 1.72(5)$ atoms/px and a radius of $R = 35$ px, while (d) yields $n_0 = 1.14(3)$ atoms/px and $R = 74$ px.

average should suffice to evaluate the results.

The optimized spherical metric is now compared to the previous realization in [54]. Since the atom number increased from 18 000 to 45 000, a larger trap with twice the radius was used in the current experiment. Figure 4.18 shows both condensates and their corresponding radial averages. Besides better following the shape of the targeted density distribution, the optimized spherical metric reaches a ratio of 1:3.6 compared to the ratio of 1:2.6 in [54].

To test the dynamical behavior of the optimized pattern, the expansion of a phononic wave packet was observed. For this, a hole puncher was placed at the edge of the condensate and the wavefront of the resulting under-density was observed. The spatial expansion after different evolution times is depicted in fig. 4.19. In fig. 4.19a, data from [54] is presented and compared to the optimized realization in fig. 4.19b. Due to the difference in the central density n_0 by a factor of two, the speed of sound is slower in fig. 4.19b. Nonetheless, the expansion of the phononic wave packet in both cases agrees with the expected dynamics. The data from [54] shows the evolution up to the straightening of the wave packet, while the current realization allows us to follow the dynamics till the refocusing. In fig. 4.19b, the reflection of the spherical wavefront follows the original wave packet. In contrast, they are overlapped in fig. 4.19a. The improvements in the current realization might mainly result from the higher atom number. However, the optimization algorithm ensures that the ratio of 1:4 is reached.

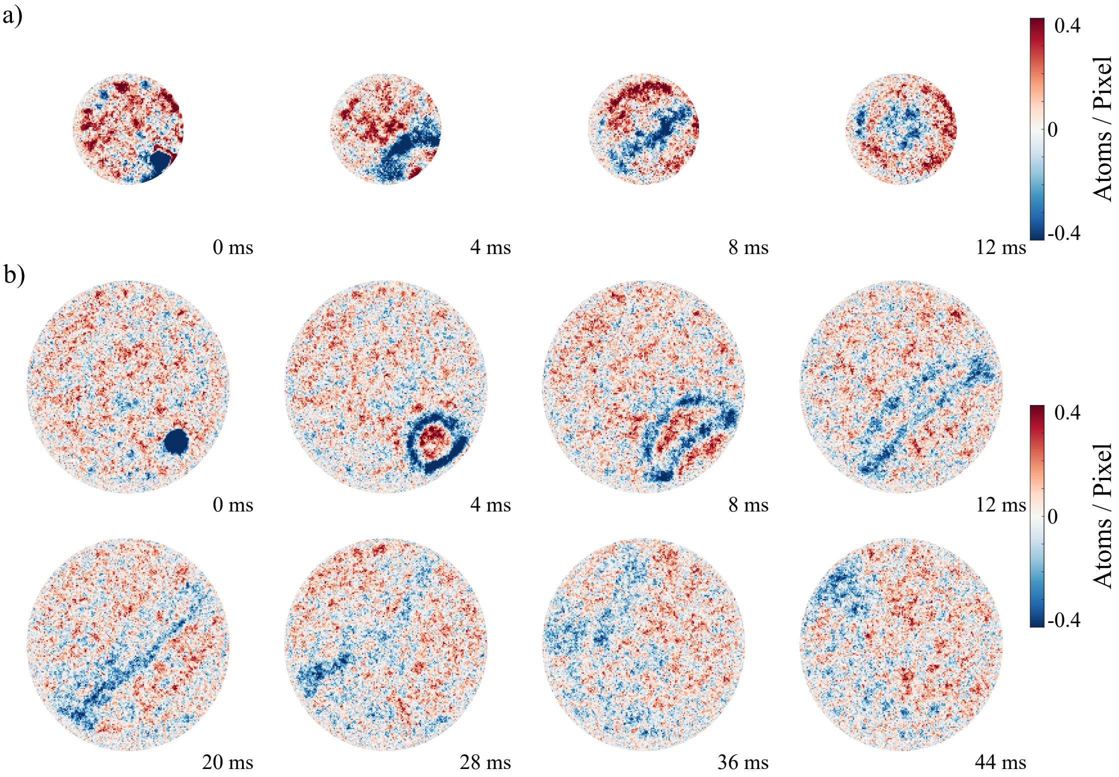

Figure 4.19: Propagation of a phononic wave packet after different hold times on the spherical background densities depicted in fig. 4.18c. Here, the differences to the unperturbed condensate are shown, where blue represents under- and red over-densities. (a) The experimental results from [54] are compared to (b) the current capabilities of the setup. While (a) has a condensate radius of $R = 35\,\mathrm{px}$, (b) has a radius of $R = 74\,\mathrm{px}$.

Grids Recent results in the experiment describe the emergence of square lattice patterns due to the periodic driving of the interaction. To investigate this phenomenon in detail, we attempted to produce finely structured square lattice density distributions to instigate dynamics in the condensate explicitly. The grid pattern is defined by

$$V_{dip}(x, y) = \frac{A}{2} \cdot \left[1 + \sin\left(\frac{2\pi x}{\lambda}\right)\right] + \frac{A}{2} \cdot \left[1 + \sin\left(\frac{2\pi y}{\lambda}\right)\right] \tag{4.17}$$

with amplitude A and period length λ. Here, an amplitude of $A = 60\,\mathrm{Hz}$ and a period length of $\lambda = 10\,\mu\mathrm{m}$ on the atomic plane were chosen. The condensate was trapped in a slanted wall potential that was already discussed in fig. 4.12a and b and was superimposed with the grid potential, as illustrated in fig. 4.20a. For this potential, four iterations are needed to converge and the results are depicted in fig. 4.20. The error map of the initial potential has an average of -0.005 and a standard deviation of 0.036, while 16 000 mirrors have to be flipped. After four iterations, the average amounts to -0.0006, and the standard deviation is decreased

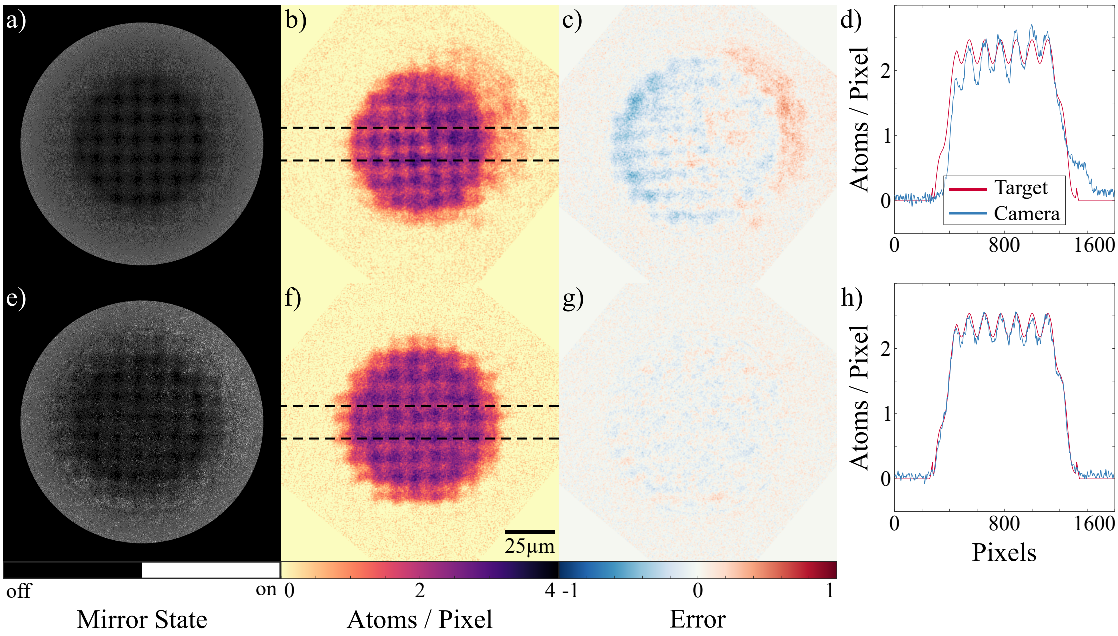

Figure 4.20: Comparison of the (a) initial DMD and (b) camera image of a grid potential (Eq. 4.17) with an (e) optimized DMD and (f) camera image after four iterations. The corresponding error maps of the initial and optimized camera image are shown in (c) and (g), respectively. The average over 200 px (dotted black lines) of each camera image are displayed in (d,h) and are compared to the average of the targeted condensate shape.

to 0.015, while 8000 mirrors need to be flipped. In comparison, the average of the error map improved by a factor of eight and the standard deviation by a factor of two. A closer look at the atomic distributions in fig. 4.20b shows that the rotational transformation was not precisely calibrated as the grid is not parallel to the dotted black lines. However, the algorithm managed to correct the rotational orientation of the grid as displayed in fig. 4.20f. The optimized error map in fig. 4.20g does not show any patterns but larger clusters of density fluctuations are observed. The average over the rows within the two black dotted lines are depicted in fig. 4.20d, h and compared to the reference. The initial pattern shows a density gradient along the x-axis and the amplitude of the grid modulation does not have the right contrast. On the other hand, the optimized pattern does not have a gradient, and the amplitude of the grid sites has the correct height. This demonstrates that the algorithm is also capable of optimizing small-scale features in the density distribution.

"Dunes" As discussed in sec. 4.1, "Dunes" arise due to a translational misalignment. Following eq. 4.7 and inserting $P_{cam} = 13\,\mu\text{m}$, $d_{DMD} = 10$, $s = 5.3$, and $P_{DMD} = 7.6\,\mu\text{m}$, a maximum shift of $\Delta = 90\,\text{px}$ is allowed. Consequently, "Dunes" should not be a relevant phenomenon for the density-based feedback algorithm. In fig. 4.17f, slight horizontal stripes can be seen on the condensate. The high light intensity required to produce the hard wall potential might favor the emergence of dunes. However, similar stripes can also be seen on atomic densities that did not use an optimized DMD pattern. Probably, these stripes could stem from a camera error. Due to temporal constraints, the "dune" phenomenon has not been studied in detail on atomic clouds.

4.2.4 Methods

The density-based feedback algorithm is written in *MATLAB* to better integrate into the existing experimental control. First, the specification of the used devices and experimental configuration parameters have to be set. This includes the selection of the reference type, as well as the initial trapping potential. The hard wall and slanted wall trapping sequence are directly implemented but any custom trapping sequence can be used. It is recommended to use an initial trap geometry that is close to the desired potential. Furthermore, several directories have to be set: First, a working directory, similar to the previous section, has to be chosen, where the camera images, debugging plots, and optimized DMD patterns are stored. Secondly, a DMD pattern folder is required. This folder contains the latest DMD sequence, which is then loaded to the DMD. Finally, the current scan folder has to be selected, from where the camera data can be loaded.

Similar to the test setup, a *DLP9000X* chip with *V4390* controller board is already implemented in the BEC experiment. Accordingly, the device specifications are similar and can be found in tab. 3.1. The images are taken by a *ProEM HS:1024BX3* camera that was characterized in [32]. It has a resolution of 1024 px × 1024 px and is controlled by the experimental control software. In contrast to the test setup, the atomic cloud formed by the projected DMD beam cannot be directly imaged but instead has to be magnified by a factor of 28.6.

5 On-demand, Deterministic Vortex Creation

With the enhanced control of the atomic cloud in sight, a new toolbox, namely on-demand, deterministic vortex creation is explored. To study vortices and obtain meaningful statistics, they have to be created in a controlled and reproducible manner. The phase imprint and chopstick method that were introduced in sec. 2.3, are now tested with the current single-DMD setup described in sec. 2.4. In the following, the choice of variables for our specific experimental setup, first results, and current limitations are presented.

5.1 Phase Imprinting

The method described in sec. 2.3.2 modifies the phase distribution of the condensate according to an external potential $V_{dip}(x,y)$. If the potential $V_{dip}(x,y)$ is an angular intensity gradient as illustrated in fig. 2.6, a total angular momentum S can be created in the condensate depending on the induced phase shift $2\pi S$. In the BECK experiment, the potential $V_{dip}(x,y)$ is applied by the DMD. Due to the refresh rate of the mirrors, the pulse length t_L cannot be smaller than $90\,\mu\mathrm{s}$ (Tab. 3.1). According to eq. 2.53, a potential difference of $\Delta V_{dip} = 10\,\mathrm{kHz}$ at the discontinuity is needed for a phase shift of 2π given a pulse-length of $t_L = 100\,\mu\mathrm{s}$. For a calibration constant of $c_L = 50\,\mathrm{kHz\,W^{-1}}$ and an intensity fraction difference of $\Delta I_{rel} = 1$ at the discontinuity, a laser power difference of $\Delta P_{DMD} = 0.2\,\mathrm{W}$ is needed, following eq. 4.9. In the current setup, a maximum DMD power of $P_{DMD} = 1\,\mathrm{W}$ is achievable.[8]

At the discontinuity, the intensity has to change abruptly to ensure a continuous angular phase gradient throughout the condensate. In contrast, a gradual intensity change will cause a strong phase gradient at the discontinuity and thus, distort the system. In the experiment, the contrast at the discontinuity is limited by the resolution of the optical setup. To not be affected by an imperfect intensity jump, the density at the discontinuity is depleted by illuminating the area before the phase imprint. A DMD power of $P_{DMD} = 0.4\,\mathrm{W}$ is used[8] such that a maximum mirror fraction of $25\,\%$ has to be turned on. This can reduce interference effects stemming from diffraction orders of neighboring mirrors being aligned. The condensate has a scattering length of $a_s = 75\,a_0$ and is confined by a circular hardwall potential with radius $r = 40\,\mu\mathrm{m}$. Here, a smaller scattering length corresponds to a larger healing length and consequently to a larger vortex core size, which simplifies detection.

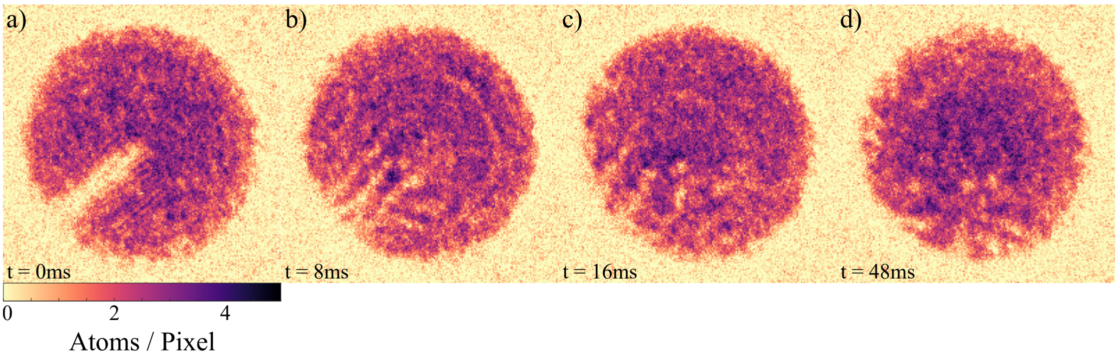

Figure 5.1: Time evolution of an atomic density distribution with $a_s = 75\,a_0$ in a hard-wall potential of radius $r = 40\,\mu\text{m}$ directly after a gradient phase imprint. The images are single realizations.

The dynamics in the condensate after the phase imprint are shown in fig. 5.1. Right after the phase imprint, the experimentally created density depletion at the discontinuity is still visible. After 8 ms, the density dip has decayed into sound waves that travel away from the depleted area. A hold time of 16 ms (Fig. 5.1c) shows vortices in the previously depleted area that might be caused by the rough surface of the confining potential creating turbulences. These vortices remain in the area for long times as can be observed in fig. 5.1d. However, even with some tuning, it was not possible to deterministically create one singular vortex in the middle of the condensate. Instead, vortices are created next to the imprinted phase jump. Additionally, a ring-shaped under-density is visible in fig. 2.6b and c that moves inwards. The interference might be caused by the light from the trapping potential and the phase imprint pattern.

With a second DMD, one device could project the trapping sequence, while the other displays the imprint pattern. This allows us to reduce the imprinting time to several microseconds, which better meets the approximation made in sec. 2.3.2. As discussed in sec. 3.1, a potential difference of $\Delta V = 100\,\text{kHz}$ is required for a pulse duration of $t_L = 1\,\mu\text{s}$. The needed laser power of $P_{DMD} = 50\,\text{mW}$ at a wavelength of $\lambda = 760\,\text{nm}$ can be achieved with the planned setup. Additionally, the interference effect will be no longer relevant as the light sources of the potential and the imprint pattern are not coherent anymore. Moreover, the Gaussian shape of the illumination beam was not considered when creating the phase imprint pattern. Accordingly, the center of the condensate has collected more phase than the outer part. By using one of the optimization algorithms, the overall shape of the projected gradient can be improved.

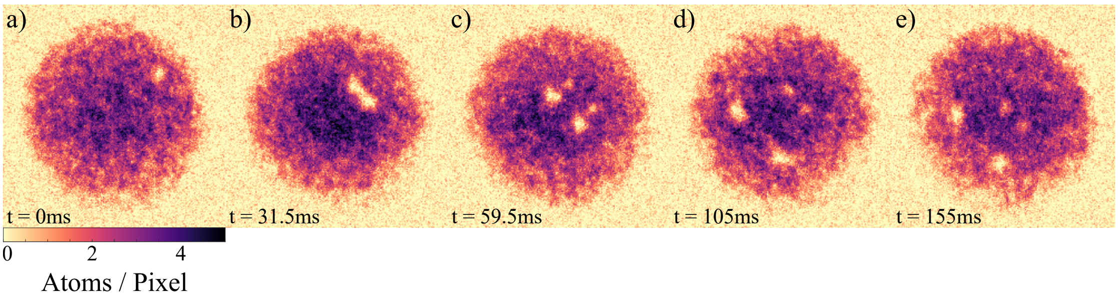

Figure 5.2: (a-d) Chopsticks sequence in a condensate with $a_s = 75\,a_0$ confined by a hardwall potential of radius $r = 40\,\mu\text{m}$. To perform the whole sequence, 105 ms are needed. The vortices are immediately lost from the beams due to a beam size smaller than 3.4 µm [24]. (e) An additional hold time of 50 ms shows the dynamic of the created vortex pair. The images correspond to single realizations.

5.2 Chopsticks Method

With the chopsticks method described in sec. 2.3.3, a neutral vortex configuration can be generated. In the BECK experiment, a DMD projects the chopsticks onto the atomic plane, which allows to easily modify all relevant parameters. As a first initial guess, a beam radius of $\sigma_c = 5\,\mu\text{m}$ is chosen. Experimental observations show that the beam radius on the DMD chip corresponds to the full width at half maximum (FWHM) of the projected beam, which is related to σ_c by

$$\text{FWHM} = \frac{\sqrt{\ln 2}}{\sqrt{2}} \cdot 2\sigma_c \tag{5.1}$$

Accordingly, a chopstick radius of 35 px on the DMD chip was set to achieve the targeted σ_c on the atomic plane. In each DMD image, the chopsticks move by 0.28 µm on the atomic plane, and the total travel distance amounts to 42 µm, but is not critical. The angle between the chopsticks is also not critical but experimental observations suggest that the two chopstick beams should overlap for a sufficiently long time. Given the beam size, an angle of $\theta = 37°$ guarantees an overlap for the first third of the sequence. After the chopstick sequence, the hold time determines how long the final chopstick position is held constant, before linearly decreasing the optical power in a prescribed fade-out time. These parameters have to be determined experimentally [45]. As an initial guess, the hold time is set to zero and the chopsticks fade out in 30 DMD images.

For the experiment realization, a condensate with a scattering length of $a_s = 75\,a_0$ in a circular hardwall potential with radius $r = 40\,\mu\text{m}$ was chosen. Following fig. 1 in [24], the ratio of sweep velocity $|\vec{v}_s|$ and speed of sound c_0 should lie within 0.11

and 0.21. For the resulting density distribution, the theoretically calculated speed of sound yields $c_0 = 1.8\,\mu\mathrm{m}\,\mu\mathrm{s}^{-1}$ (Eq. 2.29). Thus, the sweep velocity has to be between $|\vec{v}_s| = 0.2\,\mu\mathrm{m}\,\mathrm{ms}^{-1}$ and $0.4\,\mu\mathrm{m}\,\mathrm{ms}^{-1}$, corresponding to a trigger spacing between 0.7 ms and 1.4 ms. With all parameters set according to the initial guess, no vortices have been observed as the optimal hold and fade-out times have not been found yet.

However, by reducing the chopstick size to a radius of $r = 20\,\mathrm{px}$ equal to $\sigma_c = 3\,\mu\mathrm{m}$, it is expected that the vortex pair is lost from the chopsticks [24]. In this setting, the hold and fade-out times are not critical and thus, fewer parameters have to be tuned. This has been observed and is depicted in fig. 5.2. Here, decreasing the trigger spacing to 0.7 ms ($|\vec{v}_s| = 0.4\,\mu\mathrm{m}\,\mathrm{ms}^{-1}$) yields the best results. For lower sweep velocities, the vortex production is not observed in all experimental realizations. For higher velocities, the flow around the chopsticks is more turbulent creating several pairs of vortices in a less controlled manner. The vortices appear shortly after the splitting of the chopsticks and have a vortex core radius of approx. $0.75\,\mu\mathrm{m}$ ($\frac{1}{e^2}$ width) and thus, are slightly larger than the theoretically calculated healing length of $\xi = 0.6\,\mu\mathrm{m}$ (Eq. 2.9). After the vortices have been lost from the chopsticks in fig. 5.2c, they are separated by $13.9\,\mu\mathrm{m}$ and have a velocity of $0.07\,\mu\mathrm{m}\,\mathrm{ms}^{-1}$ (measured between fig. 5.2c and d). In fig. 5.2d, the distance between the vortices reduces to $10.6\,\mu\mathrm{m}$, while the velocity increases to $0.14\,\mu\mathrm{m}\,\mathrm{ms}^{-1}$ (measured between fig. 5.2d and e). After the hold time of 50 ms, the distance of the vortices remains at around $10.8\,\mu\mathrm{m}$.

The on-demand, deterministic creation of vortices using the chopsticks method seems already feasible with a single DMD. The first experimental results demonstrate that vortices can be detected by the imaging system for low-enough scattering length a_s. To make the method deterministic, the pinning of the vortex pair with the chopsticks has to be achieved by tuning the size of the chopsticks, as well as the hold and fade-out time. However, the workflow with a single DMD is tedious as a new DMD pattern sequence has to be created each time a parameter has to be changed. The second DMD could be used to only project the chopsticks sequence, which would allow to change the trigger spacings and laser power without affecting the trapping sequence. In this way, the hold and fade-out time, as well as the optical power of the chopsticks can be tuned much easier.

6 Conclusion and Outlook

In this thesis, the implementation of a second DMD setup in the experiment is planned and a test setup was built and characterized. In this process, the mounting hardware for the DMD was improved upon the version currently used in the experiment and now supports passive cooling of the controller board. The new setup will enable the projection of near-resonant, blue-, as well as red-detuned potentials onto the atomic cloud providing enhanced control necessary for future projects. This setup is ready to be implemented in the main experiment including the corresponding near-resonant laser.

A light-based feedback algorithm was designed that optimizes arbitrary DMD patterns based on a camera signal, which is compared to a target image. It compensates for the Gaussian shape of the illumination beam, dust particles on the optics, and other imperfections, like interference fringes. For the tested patterns, the average of the optimized error map improved by a factor of five and its standard deviation by a factor of three compared to the initial guess. With a resolution comparable to the experimental setup, a flat-top potential with an NRMSE of 1.8 % has been achieved over the entire beam diameter of 1 mm. The algorithm is ready to use and needs around ten iterations corresponding to 120 s to converge. The main contributor to the time is the module that maps the camera image onto the DMD image. In the future, this module could be replaced to speed up the code. Furthermore, the algorithm does not have a termination condition. Depending on α, it converges after approx. six iterations and then starts to oscillate around the optimal solution. To mitigate the oscillation and maybe reduce the residual error, α can be decreased dynamically. Additionally, a lower limit for α could be used to implement a termination condition.

A density-based version of this algorithm was implemented into the main experiment and showed significant improvements in various density distributions. These include a harmonic potential and a spherical metric. For the first example, a target trapping potential was set as a reference, while for the second a target density distribution was used. Both target options are included in the algorithm. The radial averages show significant improvements over the initial guesses. In the optimized harmonic trap, the atomic cloud nicely follows the expected Thomas-Fermi profile, while the optimized spherical metric achieves the important density ratio of 1:4 between the center and edge of the condensate. In both cases, the dynamics in the optimized traps were evaluated and the expected behavior was observed demonstrating that they are not affected by the optimization routine. Furthermore, the algorithm was applied to another current project, where it was used to optimize small-scale structures: To create a supersolid in the condensate, a fine grid pattern has to be imprinted onto the atomic cloud. The results show a similar improvement compared to the large-scale potentials, so the algorithm is also capable of optimizing small-scale features. In the future, the hyperbolic metric [54] could also be optimized. In this case, the edges of the condensate are of particular interest, where the low densities involved are highly sensitive to imperfections. Projects like these will strongly benefit from the implementation of the second DMD by using it to correct the projected potential of the first device.

With the upcoming, enhanced control of the atomic cloud in sight, a new toolbox, namely on-demand, deterministic vortex production was already explored by using the current single-DMD setup. First, the phase imprinting method was tested but did not work. This method will benefit from a second DMD that enables shorter imprint duration, as well as an optimized potential to more precisely imprint an integer phase winding over the full radial extent of the condensate. In contrast, the chopstick method seems viable with one DMD, where on-demand vortex production has been achieved. However, the pinning has not been demonstrated yet, which requires a better tuning of the chopstick size, hold, and fade-out time. With a second DMD, the static trapping potential and the dynamic sequence can be separated, which would provide more degrees of freedom. With full control over vortex production, the dynamics of this topological excitation could be observed for different metrics analog to the already studied phononic excitations. Moreover, a total net angular momentum can be induced, which allows to study the behavior of supersolids in a rotating superfluid.

By using the tune-out wavelength for potassium of $\lambda_{zero} = 768.9701(4)\,\mathrm{nm}$ [50], a fictitious magnetic field induced by the vector-Stark shift can be applied to locally induce spin rotations, which can generate excitations, topological defects [34], or even two-component dynamics. Alternatively, a two-photon Raman transition can be achieved with further modifications to the laser setup, which corresponds to a spin flip in this experimental context. The Raman transfer can be used to e.g. induce local losses, or prepare Townes solitons [2].

A Optical Components

Thorlabs

Illumination Optics

- **Cage System**
  ER4-P4
  RA90TR/M (4x)
  TR150/M-JP (2x)

- **Fiber Outcoupler**
  CP32/M (2x)
  AC127-019-B-ML
  SM05FCA2

- **Power Control**
  CRM1T/M
  WPH05M-780
  CP1M09/M (Modified)
  PBS102

- **Power Stabilization**
  CP1M09/M (Modified)
  BS071

- **Galilean Telescope (M=4)**
  ACN127-050-B
  AC254-200-B
  SM05L05
  SM1A6
  SM1M35
  SM1L15
  SM1V15
  SM1RC/M (2x)
  TR75/M-P5

Output Optics

- **Cage System**
  ER24 (4x)
  RA90TR/M (4x)
  TR150/M-JP

- **4f-Setup**
  LCP34T/M
  ACT508-400-B
  LCP34/M
  SM2D25
  For M=4:
  LCP34T/M
  ACT508-100-B
  For M=8:
  LCP33/M
  AC254-050-B-ML

- **4f-Setup (M=20)**
  TR50/M-P5
  LMR2/M
  ACT508-750-B

Imaging Optics

- **Mounting**
  TR30/M-P5
  PH40/M-P5

- **Galilean Telescope (M=10)**
  ACN127-020-B
  AC254-200-B
  SM05L05

SM1A6
SM1M35
SM1L25
SM1V15
SM1RC/M

- **4f-Setup (M=8.7)**
  AC254-300-B
  LMR1/M

MOT Optics

- **Mounting**
  TR75/M-P5
  PH75/M-P5

- **Telescope (M=1)**
  AC508-075-B
  LMR2S/M
  SM2L10
  FMP2/M

Misc

P3-630PM-FC-10
BB2-E03
BA1S/M-P5 (4x)
PH50/M-P5 (2x)
TR75/M-P5
PF85B (2x)
BS032

Others

- **Liop-Tec**
  SR100L-200-2-OR (6x)

- **Newport**
  9081-M

- **Festo**
  DGST-8-80-Y12A
  VUVG-L10-M52-MT-M5-1R8L
  GRLA-M5-QS-6-D (2x)
  QSM-M5-6-I (10x)
  PUN-6X1-SW (50 m)

B Technical Drawings

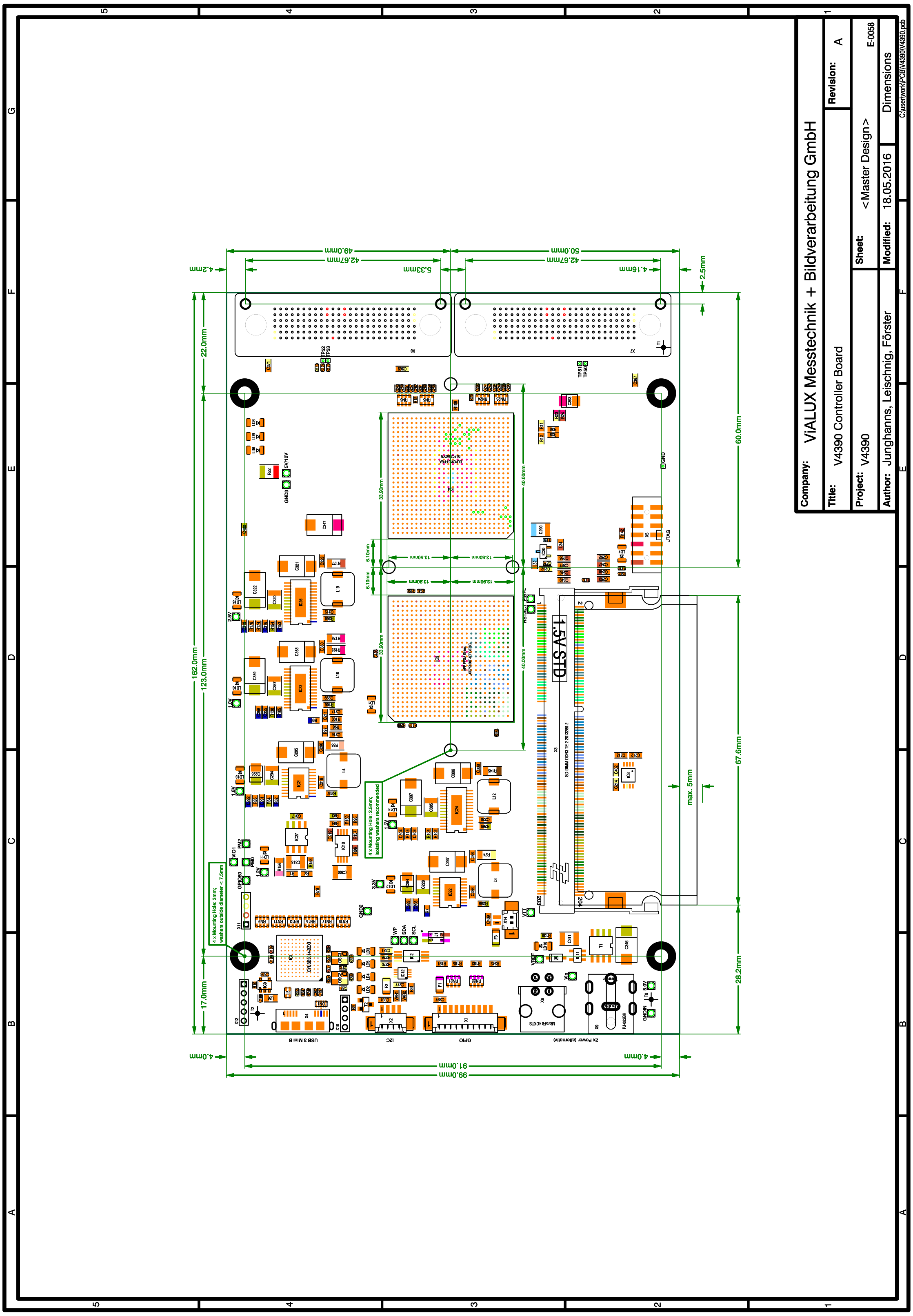

Figure B.1: *V4390* controller board dimensions provided by *ViALUX*.

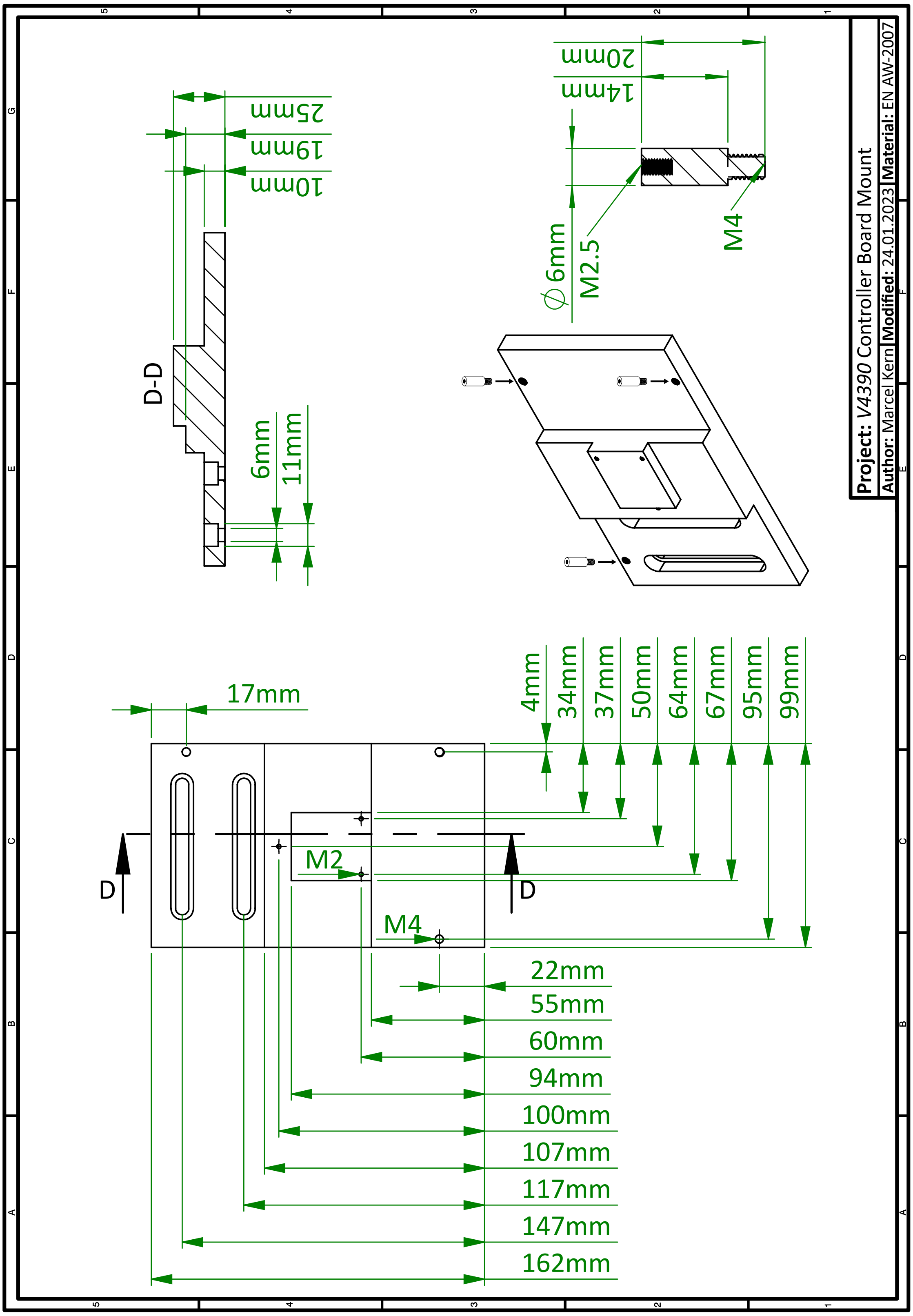

Figure B.2: *V4390* controller board mount. This mount acts as a passive heat sink for the APPS-FPGA.

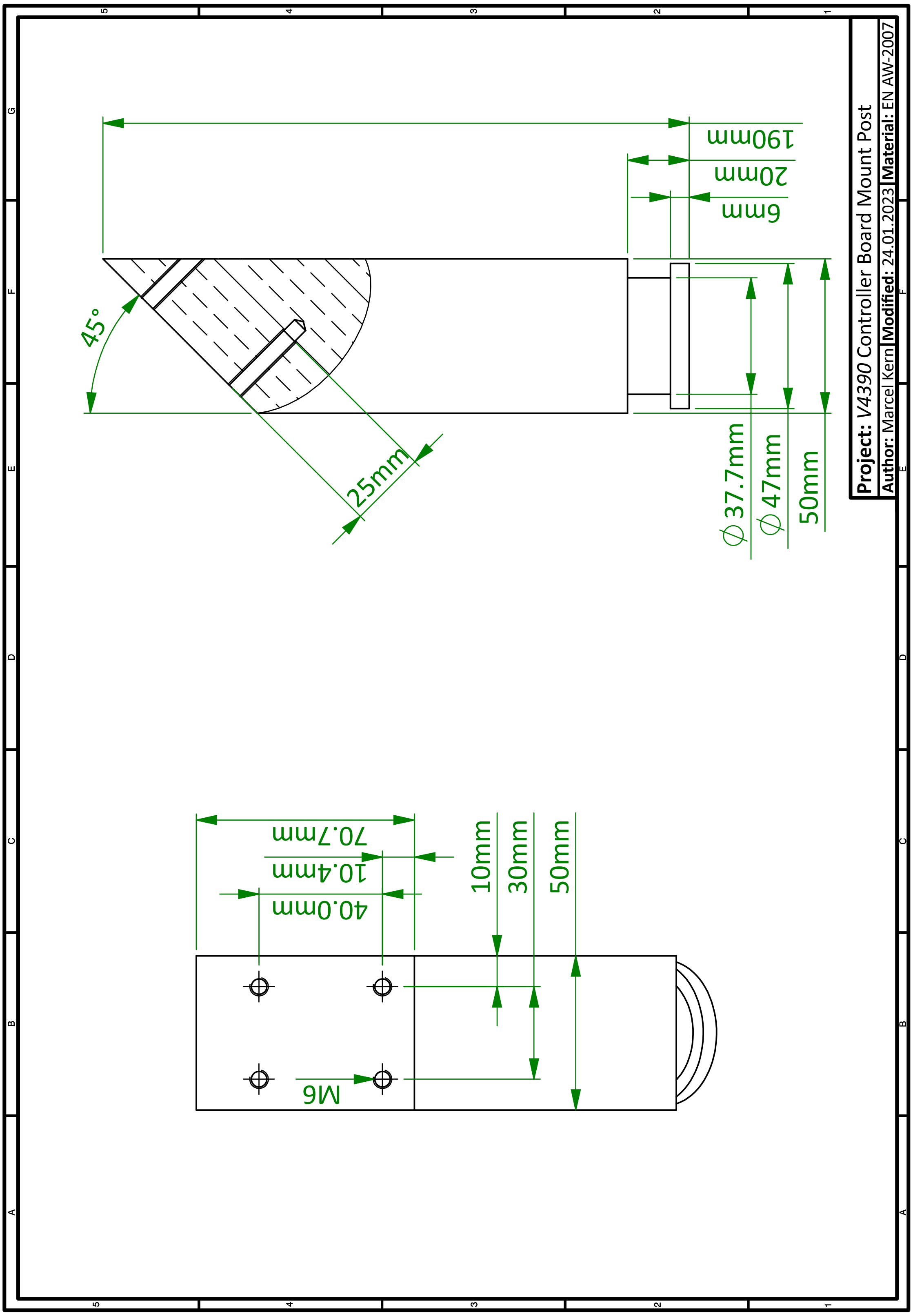

Figure B.3: Controller board mount post. The controller board mount is attached to the post by four M6 screws. The pedestal-style base of the mount is compatible with a *Thorlabs PF85B* clamping fork.

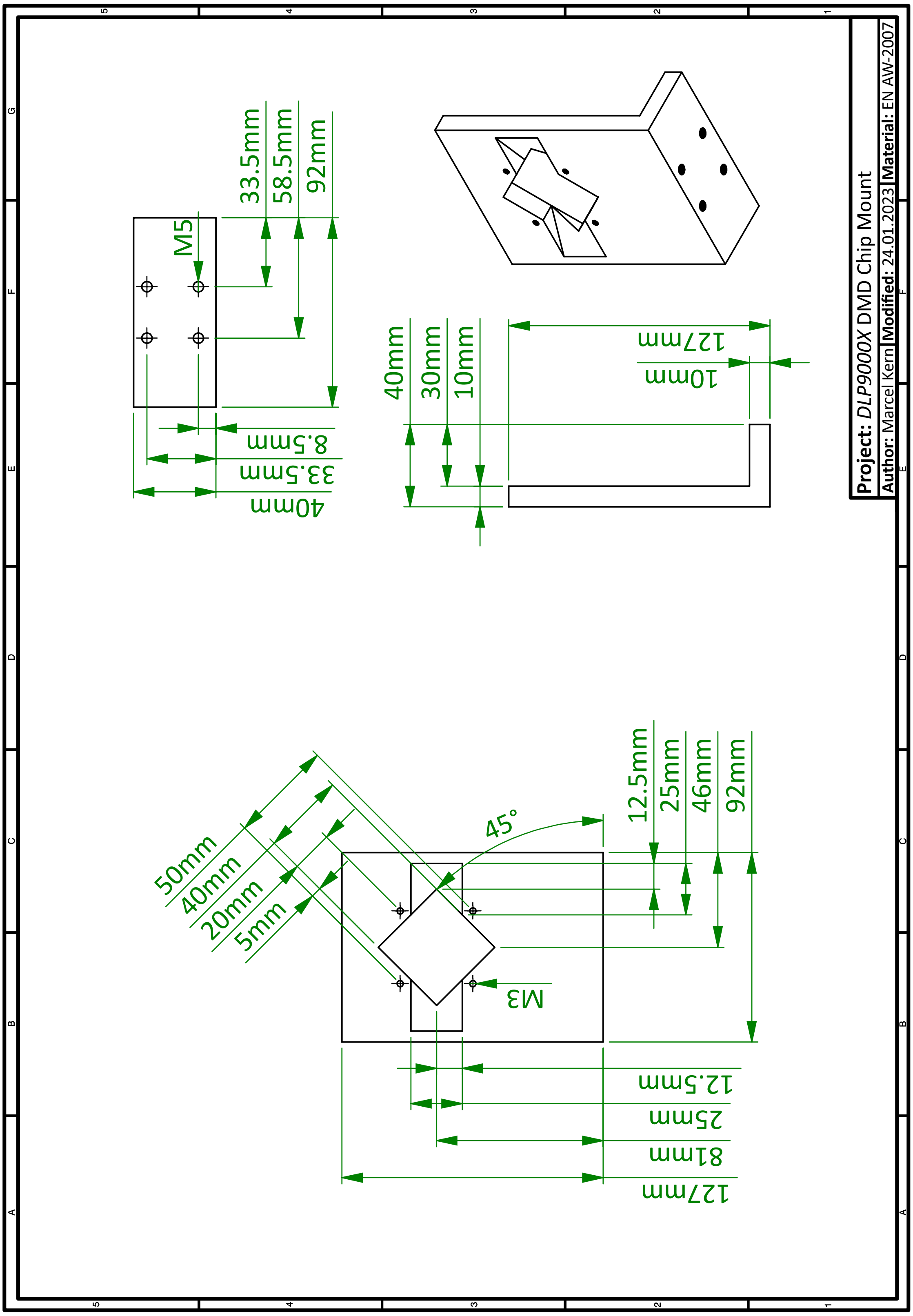

Figure B.4: *DLP9000X* DMD chip mount. The screw threads at the bottom are compatible with the *Newport 9081-M* 5-axis translation stage. The mount is designed for a beam height of 12.5 mm.

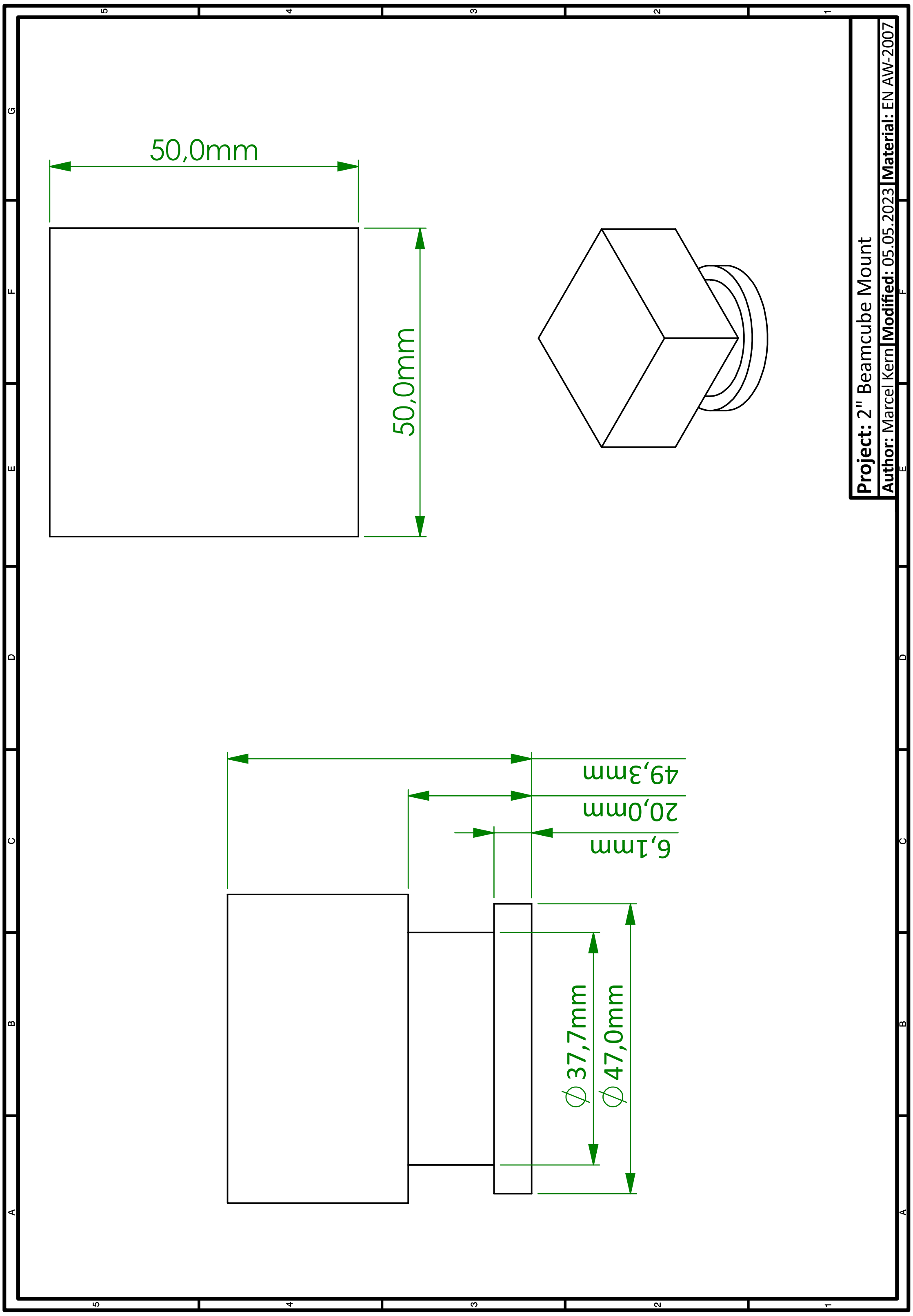

Figure B.5: Mount for a 2 inch beamcube. Designed for the vertical breadboard above the science chamber. The pedestal-style base of the mount is compatible with a *Thorlabs PF85B* clamping fork. The beamcube has to be glued onto the mount.

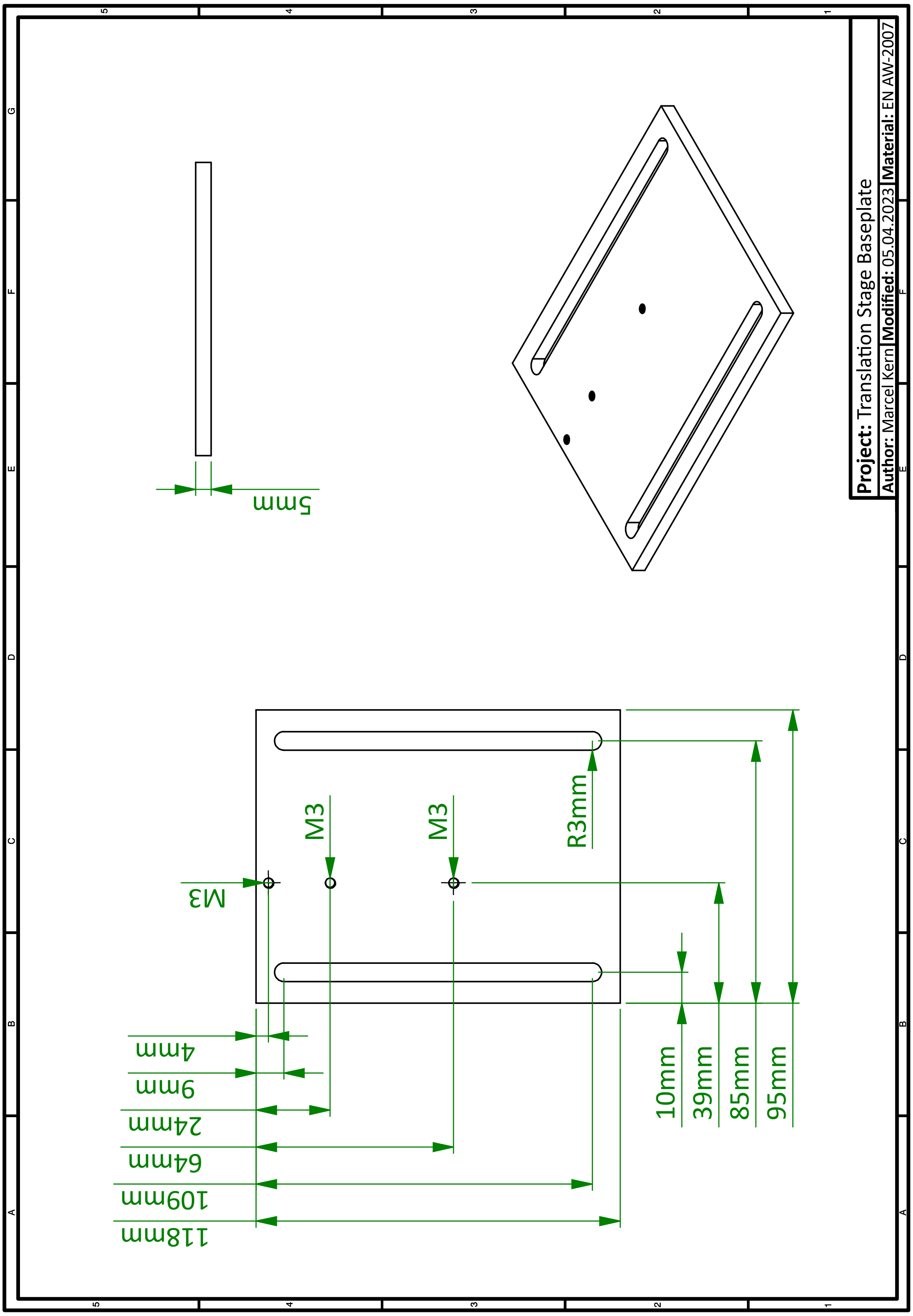

Figure B.6: Baseplate for the *Festo DGST-8-80-Y12A* mini slide, compatible to metric breadboards with 25 mm hole patterns and M6 threads.

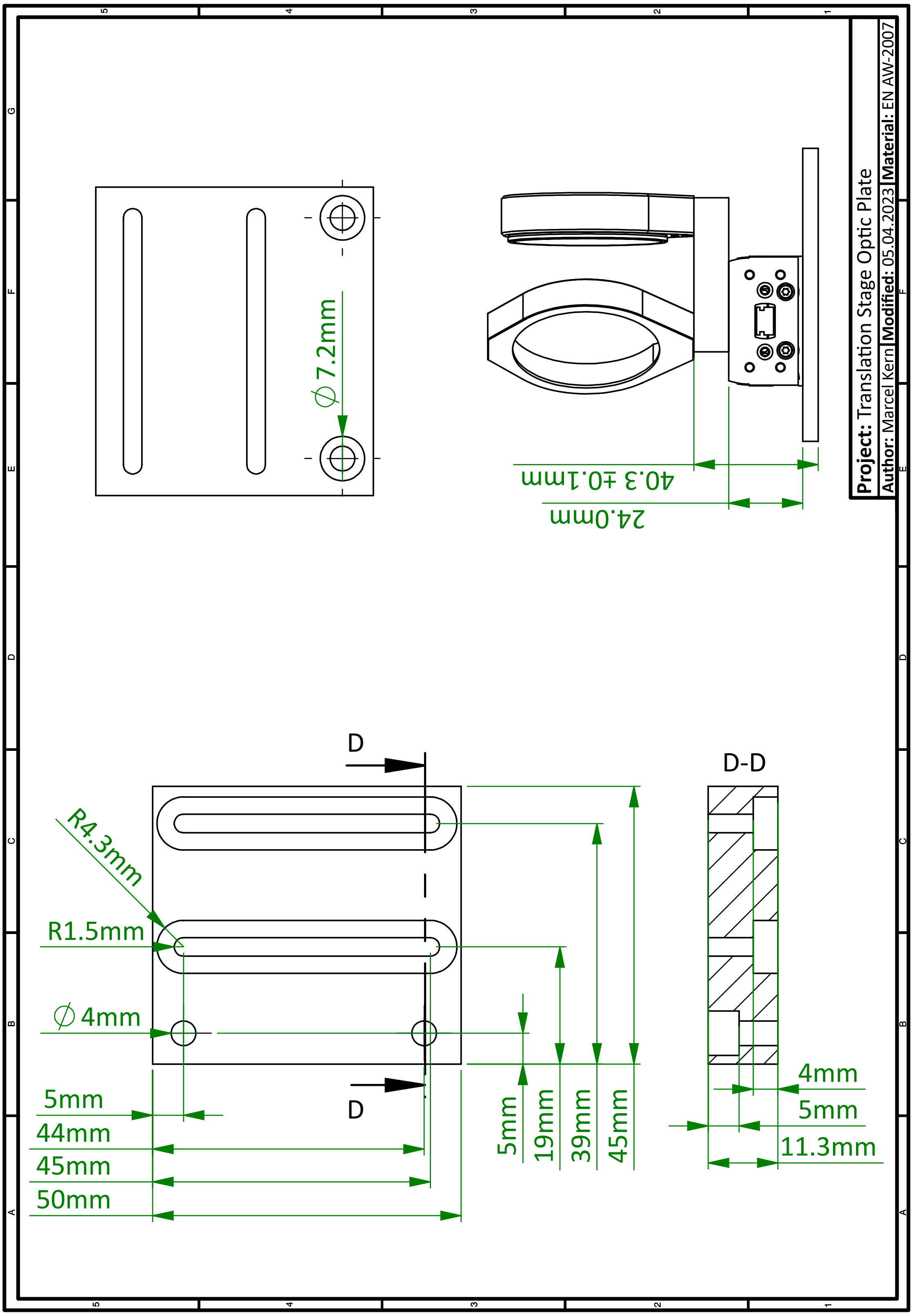

Figure B.7: Adapter plate to mount the MOT lens and a mirror onto the *Festo DGST-8-80-Y12A* mini slide. For a centered position of the MOT beam on the lens, the mini slide with base and adapter plate needs a height of exactly 40.3 mm.

C Electronical Drawings

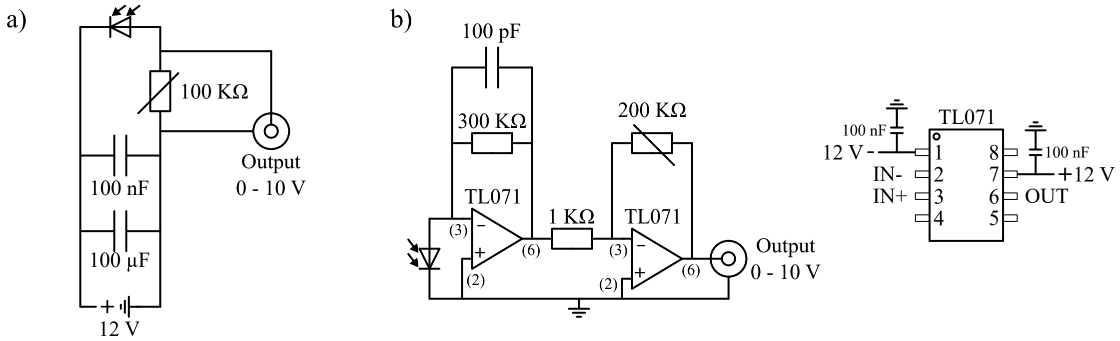

Figure C.1: (a) Fast photodiode circuit for the integration in the main experiment and (b) transimpedance amplifier for the test setup. With the potentiometers, the sensitivity of the photodiode can be adapted to the used laser power.

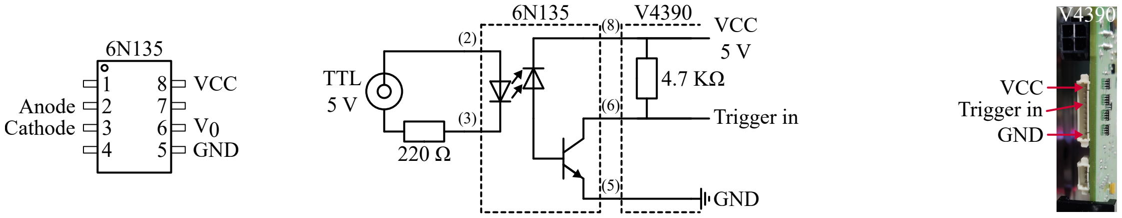

Figure C.2: Optocoupler circuit to trigger the DMD via an external TTL signal. A *Molex PicoBlade*^{TM} header is used to connect the optocoupler with the *V4390* controller board. Note that this connector is not hot-plug capable. More details can be found in [51]. Designed by Marius Sparn.

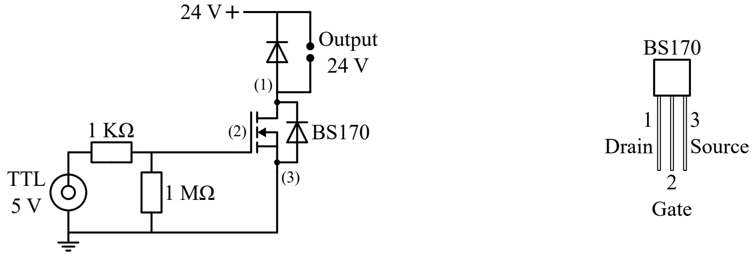

Figure C.3: Circuit to control the *Festo* solenoid valve (*VUVG-L10-M52-MT-M5-1R8L*) via an external TTL signal. The valve either extends or retract the *Festo* mini slide (*DGST-8-80-Y12A*). Adapted from Maurus Hans and designed by Joris Hoffmann.

Bibliography

[1] M. H. Anderson et al. “Observation of Bose-Einstein Condensation in a Dilute Atomic Vapor”. In: *Science* 269.5221 (1995), pp. 198–201. DOI: 10.1126/science.269.5221.198 (cit. on p. 5).

[2] B. Bakkali-Hassani et al. “Realization of a Townes Soliton in a Two-Component Planar Bose Gas”. In: *Phys. Rev. Lett.* 127 (2 July 2021), p. 023603. DOI: 10.1103/PhysRevLett.127.023603 (cit. on p. 73).

[3] I. Bloch, J. Dalibard, and S. Nascimbène. “Quantum simulations with ultracold quantum gases”. In: *Nature Physics* 8 (4 Apr. 2012), pp. 267–276. DOI: 10.1038/nphys2259 (cit. on p. 1).

[4] I. Bloch and C. Gross. “Quantum simulations with ultracold atoms in optical lattices”. In: *Science* 357 (6355 Apr. 2017), pp. 995–1001. DOI: 10.1126/science.aal3837 (cit. on p. 1).

[5] M. Bôcher. “Introduction to the Theory of Fourier’s Series”. In: *Annals of Mathematics* 7.3 (1906), pp. 81–152. DOI: 10.2307/1967238 (cit. on p. 46).

[6] N. N. Bogoljubov. “On a new method in the theory of superconductivity”. In: *Il Nuovo Cimento* 7 (6 1958), pp. 794–85. DOI: 10.1007/BF02745585 (cit. on p. 9).

[7] N. Bose. “Plancks Gesetz und Lichtquantenhypothese”. In: *Zeitschrift für Physik* 26 (1924), pp. 178–181. DOI: 10.1007/BF01327326 (cit. on p. 5).

[8] T. Bourgeois. “Tailorable optical trap with Digital Micromirror Device for Dysprosium experiment”. Masterarbeit. Universität Heidelberg, 2023 (cit. on pp. 46, 47).

[9] C. Chin et al. “Feshbach resonances in ultracold gases”. In: *Rev. Mod. Phys.* 82 (2 Apr. 2010), pp. 1225–1286. DOI: 10.1103/RevModPhys.82.1225 (cit. on p. 3).

[10] Coherent. *MBR-110*. 2013. URL: https://www.symphotony.com/wp-content/uploads/MBR110_DS_0913revB_1.pdf (visited on 02/28/2024) (cit. on p. 21).

[11] R. J. Cook and A. F. Bernhardt. “Deflection of atoms by a resonant standing electromagnetic wave”. In: *Phys. Rev. A* 18 (6 Dec. 1978), pp. 2533–2537. DOI: 10.1103/PhysRevA.18.2533 (cit. on p. 16).

[12] K. B. Davis et al. “Bose-Einstein Condensation in a Gas of Sodium Atoms”. In: *Phys. Rev. Lett.* 75 (22 Nov. 1995), pp. 3969–3973. DOI: `10.1103/PhysRevLett.75.3969` (cit. on p. 5).

[13] M. C. Davis et al. “Manipulation of vortices by localized impurities in Bose-Einstein condensates”. In: *Phys. Rev. A* 80 (2 Aug. 2009), p. 023604. DOI: `10.1103/PhysRevA.80.023604` (cit. on p. 18).

[14] J. Denschlag et al. “Generating Solitons by Phase Engineering of a Bose-Einstein Condensate”. In: *Science* 287.5450 (2000), pp. 97–101. DOI: `10.1126/science.287.5450.97` (cit. on p. 16).

[15] Ł. Dobrek et al. “Optical generation of vortices in trapped Bose-Einstein condensates”. In: *Phys. Rev. A* 60 (5 Nov. 1999), R3381–R3384. DOI: `10.1103/PhysRevA.60.R3381` (cit. on p. 16).

[16] C. Eckart. “The Application of Group theory to the Quantum Dynamics of Monatomic Systems”. In: *Rev. Mod. Phys.* 2 (3 July 1930), pp. 305–380. DOI: `10.1103/RevModPhys.2.305` (cit. on p. 15).

[17] A. Einstein. “Quantentheorie des einatomigen idealen Gases”. In: *Albert Einstein: Akademie-Vorträge.* John Wiley & Sons, Ltd, 2005, pp. 237–257. DOI: `10.1002/3527608958.ch27` (cit. on p. 5).

[18] uwe electronic. *UEKK – CHBF3127271802 - 00.* URL: `https://www.uweelectronic.de/images/datenblaetter_malico/bga_kuehler_luefter/chbf3127271802_00.pdf` (visited on 02/28/2024) (cit. on p. 25).

[19] J. Etrych et al. “Pinpointing Feshbach resonances and testing Efimov universalities in ^{39}K”. In: *Phys. Rev. Res.* 5 (1 Mar. 2023), p. 013174. DOI: `10.1103/PhysRevResearch.5.013174` (cit. on pp. 4, 19, 20).

[20] H. Feshbach. “Unified theory of nuclear reactions”. In: *Annals of Physics* 5.4 (1958), pp. 357–390. DOI: `10.1016/0003-4916(58)90007-1` (cit. on p. 3).

[21] R. P. Feynman. “Simulating physics with computers”. In: *International Journal of Theoretical Physics* 21 (6 June 1982), pp. 467–488. DOI: `10.1007/BF02650179` (cit. on p. 1).

[22] R. W. Floyd and L. Steinberg. “An Adaptive Algorithm for Spatial Greyscale”. In: *Proceedings of the Society for Information Display* 17 (1976), pp. 75–77 (cit. on p. 39).

[23] A. L. Gaunt et al. “Bose-Einstein Condensation of Atoms in a Uniform Potential”. In: *Phys. Rev. Lett.* 110 (20 May 2013), p. 200406. DOI: `10.1103/PhysRevLett.110.200406` (cit. on p. 1).

[24] B. Gertjerenken et al. "Generating and manipulating quantized vortices on-demand in a Bose-Einstein condensate: A numerical study". In: *Phys. Rev. A* 93 (2 Feb. 2016), p. 023604. DOI: `10.1103/PhysRevA.93.023604` (cit. on pp. 17, 18, 70, 71).

[25] R. Grimm, M. Weidemüller, and Y. B. Ovchinnikov. "Optical Dipole Traps for Neutral Atoms". In: vol. 42. Advances In Atomic, Molecular, and Optical Physics. Academic Press, 2000, pp. 95–170. DOI: `10.1016/S1049-250X(08)60186-X` (cit. on pp. 4, 13).

[26] E. P. Gross. "Structure of a quantized vortex in boson systems". In: *Il Nuovo Cimento* 20 (3 1961), pp. 454–477. DOI: `10.1007/BF02731494` (cit. on p. 6).

[27] G. Guillaume. *Transport and Turbulence in Quasi-Uniform and Versatile Bose-Einstein Condensates*. Springer International Publishing, 2020. DOI: `10.1007/978-3-030-54967-1_4` (cit. on pp. 8, 11, 31, 36, 41, 42).

[28] G. Guillaume et al. "Direct imaging of a digital-micromirror device for configurable microscopic optical potentials". In: *Optica* 3.10 (Oct. 2016), pp. 1136–1143. DOI: `10.1364/OPTICA.3.001136` (cit. on p. 1).

[29] T. Guillemot and J. Delon. "Implementation of the Midway Image Equalization". In: *Image Processing On Line* 6 (2016), pp. 114–129. DOI: `10.5201/ipol.2016.140` (cit. on p. 50).

[30] M. Hans. "Physical Computing on a Versatile Setup for Ultra-cold Potassium". PhD thesis. Universität Heidelberg, 2022 (cit. on pp. 18, 19, 55).

[31] Texas Instruments. *DLP9000 Family of 0.9 WQXGA Type A DMDs*. 2016. URL: `https://www.ti.com/lit/ds/symlink/dlp9000.pdf` (visited on 02/28/2024) (cit. on pp. 24, 28).

[32] E. Kath. "Feasability of Single-Atom-Resolved Fluorescence Imaging of Freely Propagating K39 Atoms". Masterarbeit. Universität Heidelberg, 2022 (cit. on p. 67).

[33] W. J. Kwon et al. "Sound emission and annihilations in a programmable quantum vortex collider". In: *Nature* 600 (7887 Dec. 2021), pp. 64–69. DOI: `10.1038/s41586-021-04047-4` (cit. on p. 1).

[34] S. Lannig. "Vector Solitons and Different Scenarios of Universal Dynamics in a Spin-1 Bose-Einstein Condensate". PhD thesis. Universität Heidelberg, 2022 (cit. on p. 73).

[35] J. Liang et al. “1.5% root-mean-square flat-intensity laser beam formed using a binary-amplitude spatial light modulator”. In: *Appl. Opt.* 48.10 (Apr. 2009), pp. 1955–1962. DOI: `10.1364/AO.48.001955` (cit. on p. 46).

[36] N. Liebster et al. *Emergence of crystalline steady state in a driven superfluid.* 2023. DOI: `10.48550/arXiv.2309.03792` (cit. on p. 1).

[37] K. W. Madison et al. “Vortex Formation in a Stirred Bose-Einstein Condensate”. In: *Phys. Rev. Lett.* 84 (5 Jan. 2000), pp. 806–809. DOI: `10.1103/PhysRevLett.84.806` (cit. on p. 11).

[38] E. Mandelung. “Quantentheorie in hydrodynamischer Form”. In: *Zeitschrift für Physik* 40 (3 Mar. 1927), pp. 322–326. DOI: `10.1007/BF01400372` (cit. on p. 11).

[39] M. R. Matthews et al. “Vortices in a Bose-Einstein Condensate”. In: *Phys. Rev. Lett.* 83 (13 Sept. 1999), pp. 2498–2501. DOI: `10.1103/PhysRevLett.83.2498` (cit. on p. 11).

[40] A. J. Moerdijk, B. J. Verhaar, and A. Axelsson. “Resonances in ultracold collisions of ^{6}Li, ^{7}Li, and ^{23}Na”. In: *Phys. Rev. A* 51 (6 June 1995), pp. 4852–4861. DOI: `10.1103/PhysRevA.51.4852` (cit. on p. 3).

[41] R. Onofrio et al. “Observation of Superfluid Flow in a Bose-Einstein Condensed Gas”. In: *Phys. Rev. Lett.* 85 (11 Sept. 2000), pp. 2228–2231. DOI: `10.1103/PhysRevLett.85.2228` (cit. on p. 11).

[42] L. P. Pitaevskii. “Vortex Lines in an Imperfect Bose Gas”. In: *Sov. Phys. JETP.* 13 (2 1961), pp. 451–454 (cit. on pp. 6, 12).

[43] R. W. Powell, C. Y. Ho, and P. E. Liley. *Thermal conductivity of selected materials.* Vol. 8. US Department of Commerce, National Bureau of Standards Washington, DC, 1966 (cit. on p. 26).

[44] G. Reinaudi et al. “Strong saturation absorption imaging of dense clouds of ultracold atoms”. In: *Opt. Lett.* 32.21 (Nov. 2007), pp. 3143–3145. DOI: `10.1364/OL.32.003143` (cit. on p. 57).

[45] E. C. Samson et al. “Deterministic creation, pinning, and manipulation of quantized vortices in a Bose-Einstein condensate”. In: *Phys. Rev. A* 93 (2 Feb. 2016), p. 023603. DOI: `10.1103/PhysRevA.93.023603` (cit. on pp. 17, 70).

[46] N. Seshasayee. *Understanding Thermal Dissipation and Design of a Heatsink.* Application Report. Texas Instruments, 2011. URL: `https://www.ti.com/lit/an/slva462/slva462.pdf` (visited on 02/28/2024) (cit. on p. 26).

[47] M. Sparn. “A Setup for Creating Arbitrary Potentials in a Two-dimensional 39K BEC with a Digital Micromirror Device”. Masterarbeit. Universität Heidelberg, 2020 (cit. on pp. 21, 22, 24, 25, 29–31).

[48] Thorlabs. *Does NA provide a good estimate of beam divergence from a single mode fiber?* 2020. URL: https://www.thorlabs.com/newgrouppage9.cfm?objectgroup_id=14204 (visited on 02/28/2024) (cit. on p. 23).

[49] T. G. Tieck. “Feshbach Resonances in Ultracold Mixtures of the Fermionic Quantum Gases ^{6}Li and ^{40}K”. PhD thesis. University of Amsterdam, 2009 (cit. on p. 3).

[50] R. Trubko et al. “Potassium tune-out-wavelength measurement using atom interferometry and a multipass optical cavity”. In: *Phys. Rev. A* 95 (5 May 2017), p. 052507. DOI: 10.1103/PhysRevA.95.052507 (cit. on p. 73).

[51] ViALUX. *V4390 Controller Board. Technical Reference.* 2017 (cit. on p. 83).

[52] ViALUX. *SuperSpeed V-Modules.* 2023. URL: https://www.vialux.de/Website/PDF/ALP/E_SuperSpeed%20V-Modules.pdf (visited on 02/28/2024) (cit. on p. 24).

[53] C. Viermann. “Cosmological particle production and curced spaces in an ultracold quantum gas”. PhD thesis. Universität Heidelberg, 2022 (cit. on pp. 4, 5, 18).

[54] C. Viermann et al. “Quantum field simulator for dynamics in curved spacetime”. In: *Nature* 611 (Aug. 2022), pp. 260–264. DOI: 10.1038/s41586-022-05313-9 (cit. on pp. 1, 53, 64, 65, 73).

[55] E. Wigner. “Einige Folgerungen aus der Schrödingerschen Theorie für die Termstrukturen”. In: *Zeitschrift für Physik* 43 (9 Sept. 1927), pp. 624–652. DOI: 10.1007/BF01397327 (cit. on p. 15).

Erklärung

Ich versichere, dass ich diese Arbeit selbstständig verfasst und keine anderen als die angegebenen Quellen und Hilfsmittel benutzt habe.

Heidelberg, den 01.04.2024,

Acknowledgements

At the end of this thesis, I would like to thank the people who made this work possible:

First, I would like to thank Prof. Markus Oberthaler for the opportunity to do my Master's project in his group and to present the results at two conferences. Your optimism and passion for physics always encouraged and motivated me during this journey.

Also I want to thank Prof. Lauriane Chomaz for being the second referee and for her interest in my work.

A huge thank you to the whole Matterwave group, who warmly welcomed me. I enjoyed the numerous discussions - not only about physics - and I will miss especially the Friday breakfasts. It was a very nice experience to be part of this group. In particular, I want to thank Helmut Strobel for the advice and help in every situation. I have learned a lot from you.

And of course, I have to thank the BECK team that has provided the right environment and supported me in every way possible. Especially, Marius Sparn for his expertise during the planning and building of the DMD setup, Nikolas Liebster for his patience, while testing and debugging the density-based algorithm, and Elinor Kath for her enthusiasm on the hunt for vortices. All of them also invested a lot of time in proofreading this thesis. I really enjoyed the time with you all.

Thanks to the Quantum Fluid group, particularly Karthik Chandrashekara and Christian Gölzhäuser, for the good collaboration and discussions on the different aspects of operating a DMD.

All the custom solutions for this setup were realized by KIP's mechanic workshop, primarily by Julia Bing and David Jansen. Thank you for the quick and easy communication, as well as the ideas you added to my drafts.

Finally, I would like to thank my friends, family, and girlfriend, Sarah, who have supported me all the years. Without you all, I would not have come that far.